

AD-754 939

OPTICS RESEARCH, 1972:1

Robert H. Rediker

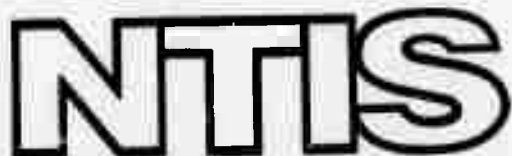
Massachusetts Institute of Technology

Prepared for:

Electronic Systems Division  
Advanced Research Projects Agency

19 December 1972

DISTRIBUTED BY:



National Technical Information Service  
U. S. DEPARTMENT OF COMMERCE  
5285 Port Royal Road, Springfield Va. 22151

# **DISCLAIMER NOTICE**

**THIS DOCUMENT IS THE BEST  
QUALITY AVAILABLE.**

**COPY FURNISHED CONTAINED  
A SIGNIFICANT NUMBER OF  
PAGES WHICH DO NOT  
REPRODUCE LEGIBLY.**

AD 754939

# Optics Research

1

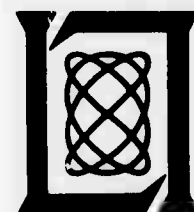
1972

Prepared for the Advanced Research Projects Agency  
and the Department of the Air Force  
under Electronic Systems Division Contract F19628-70-C-0230 by

# Lincoln Laboratory

MASSACHUSETTS INSTITUTE OF TECHNOLOGY

LEXINGTON, MASSACHUSETTS



Reproduced by  
**NATIONAL TECHNICAL  
INFORMATION SERVICE**  
U.S. Department of Commerce  
Springfield, VA 22151

165  
P

**DOCUMENT CONTROL DATA - R&D**

(Security classification of title, body of abstract and indexing annotation must be entered when the overall report is classified)

1

1972

## Optics Research

Issued 19 December 1972

Prepared for the Advanced Research Projects Agency  
and the Department of the Air Force  
under Electronic Systems Division Contract F19628-70-C-0230 by

# Lincoln Laboratory

MASSACHUSETTS INSTITUTE OF TECHNOLOGY

LEXINGTON, MASSACHUSETTS



Approved for public release; distribution unlimited.

Preceding page blank

The work reported in this document was performed at Lincoln Laboratory, a center for research operated by Massachusetts Institute of Technology. This work was sponsored by the Advanced Research Projects Agency of the Department of Defense under Air Force Contract F19628-70-C-0230 (ARPA Order 600). Where noted, research sponsored by the Environmental Protection Agency is included.

This report may be reproduced to satisfy needs of U.S. Government agencies.

Non-Lincoln Recipients

**PLEASE DO NOT RETURN**

Permission is given to destroy this document  
when it is no longer needed.

# CONTENTS

Abstract	iii
Introduction	vii
Reports on Optics Research	x1
Organization	xv
I. LASER TECHNOLOGY AND PROPAGATION	1
A. CW Theory	1
1. Laser Propagation Through a Turbulent Medium	1
2. Interaction of Heating and Turbulence in Thermal Blooming	10
3. Calculations of Phase Correction for a Laboratory Thermal Blooming Experiment	13
B. Effects	15
1. Laser-Induced Air Breakdown	15
2. Surface Interactions	19
3. Explosive Vaporization of Fog Droplets by a $10.6\text{-}\mu\text{m}$ Laser Pulse	31
C. Devices	37
1. Electron Beam (e-Beam)	37
2. The Possibility of Generating Laser Plasmas by Photoionization	51
3. Other Device Work	54
II. OPTICAL MEASUREMENTS AND INSTRUMENTATION	59
A. ZnS Up-Conversion	59
B. IR Camera (4 inch)	59
C. Interferometric Imaging Techniques	62
1. Introduction	62
2. Experimental Program	63
3. Results	65
4. Conclusions	67
D. Airborne Image Studies	68
1. Measurements of the Tropopause Effect	68
2. Boundary Layer	71
E. Tunable Infrared Laser Spectroscopy of Sulfur Dioxide	72
1. Introduction	72
2. Diode Laser Fabrication and Experimental Procedure	73
3. Theory	73
4. Results	74
5. Application of Theoretical Spectra to Pollutant Gas Monitoring	77
6. Acknowledgments	78
F. Extension of Tunable Laser Techniques to Air Pollution Detection	78
1. Spectrophone Investigation	79
2. <u>In-Situ</u> Auto Exhaust Measurements	79
3. Long-Path Laser Transmission Studies	83

**Contents**

III. LASER RADAR AND TRACKING	85
A. Instrument for Atmospheric Modulation Transfer Function Measurements	85
1. Introduction	85
2. MTF Electronics	86
B. Automatic Range Tracker	87
C. Atmospheric Optical Coherence Measurements at 10.6 and 0.63 $\mu$ m	88
D. InSb Isolator	89

# INTRODUCTION

## I. LASER TECHNOLOGY AND PROPAGATION

The computer code for calculating thermal blooming described previously has been extended to include the effects of turbulence in the atmosphere.

A theoretical study has been made of two mechanisms which have been suggested as important in thermal blooming calculations: the dependence of  $\alpha$  upon localized temperature in a thermally turbulent medium, and the effect of velocity turbulence which would tend to cool off the heated air. The study shows that for power levels presently contemplated, both these effects are negligible.

A series of propagation calculations have been performed which show that CW thermal blooming can be considerably reduced by an initial phase correction of the laser beam.

Several experiments were performed to investigate the effects of atmospheric dust on the breakdown threshold of 10.6- $\mu\text{m}$  laser beams with large focal spots. The lasers used in these experiments were a 1-kJ pulsed e-beam at Aveo Everett Research Laboratories (AERL), and a 3-J pulsed TEA laser at Lincoln Laboratory. The main conclusions from these experiments are: the breakdown threshold of clean air is close to that predicted by microwave breakdown theory; dust particles can lower the threshold below this value roughly in proportion to their size; and the presence of atmospheric dust can explain the "spot size effect" reported recently by D. C. Smith.

Impulse data obtained with the AERL 1-kJ pulsed CO<sub>2</sub> laser have been roughly correlated with a simple cylindrical blast wave model. The apparent saturation of impulse with increasing laser energy was observed in the presence of multiple aerosol-induced breakdowns in the laser beam.

Observations of plasmas produced by irradiation of surfaces with the AERL pulsed CO<sub>2</sub> laser were carried out. The plasma and associated shock-wave expansions were observed with a framing camera ( $2 \times 10^6$  frames/sec). The plasma absorption at wavelengths 4881 Å and 10.6  $\mu\text{m}$  was measured and used to infer electron density histories.

The explosive vaporization of individual water droplets (5- to 25- $\mu\text{m}$  radius) by a 10.6- $\mu\text{m}$  laser pulse has been observed with a high-speed schlieren photography system. The hot vapor sphere and the shock wave produced by the explosion can be clearly distinguished in the schlieren photographs.

The Lincoln 500-J CO<sub>2</sub> e-beam excited laser is in the final stages of construction. Laser operations should commence in August 1972, and full device operation is expected during October.

The rate equations and temperature balance equation have been solved to predict small signal gain, pulse energy, and pulse length for an e-beam excited CO<sub>2</sub> laser. The initial spike, as

## Introduction

observed experimentally for the laser pulse from the Avco e-beam device, has been predicted but the computed temporal width is narrower than that observed.

A 2.5-m unstable confocal positive branch resonator has been designed for the pulsed 500-J CO<sub>2</sub> laser so that effective use can be made of the large-volume short-length (1 m) gain medium. Although several different outcouplings and geometries will be tried, it is expected that the optimum mode quality outcoupling 85 percent will produce 45 percent of the net energy within the first Airy dark ring.

The Fredholm integral equation is used to determine the asymmetric unstable resonator cavity mode field distribution without a gain medium. Conversion is made by function expansion to the eigenvalue solution of an infinite matrix. A finite matrix solution approximation is then used for computer calculation.

A 3-nsec 600-keV e-beam source has been used to initiate a CO<sub>2</sub> laser beam. Output optical pulses up to 120μsec and 22.4J have been observed from an active volume of about 1 liter.

A pulsed CO<sub>2</sub> laser beam has been shaped in time by passing the beam through an absorption cell that is external to the laser and filled with SF<sub>6</sub> or Freon-12. The initial spike on the laser pulse has been successfully attenuated when passed through the absorption cell.

A theoretical investigation has been carried out to determine the difficulties of amplifying very short (~1 nsec) pulses or frequency-chirped pulses at 10-μm optical wavelength to high energies (~200 J/sequence). The conclusions indicated that only the volume preionized devices are reasonable in the last stages of amplification. Considerations are made of the saturation and pulse sharpening limitations on such devices. Frequency distortion and index changes are not seen to be a serious problem. The most severe difficulties are found to be in bulk medium heating and cathode shock-wave distortion as limiting the coherence time of the pulses.

It should be possible to produce electron densities on the order of 10<sup>12</sup>/cm<sup>3</sup> at atmospheric pressure by photoionization in a laser gas such as CO<sub>2</sub> or CO. The ionization produced will be uniform throughout large laser medium volumes if the photon absorption length is large, and this can be accomplished by seeding the laser gas with a low partial pressure of gas that has a low ionization potential. This will then allow deep photon penetration and low-energy UV photons to be utilized for ionization.

A small ionization cell containing a Xe flash lamp with suprasil window and two flat parallel electrodes is used to study volume photoelectron ionization. When 0.2 torr of tripropylamine is added to 500-torr N<sub>2</sub>, an electron density  $n_e = 10^{10}/\text{cm}^3$  is measured upon flash-lamp ignition. The current is found to vary linearly with applied electrode voltage, which implies an  $n_e$  production only by photoionization.

The small signal gain and laser level pumping rates for a CO<sub>2</sub> laser have been scaled with pressure to 10 atm. Using longitudinal excitation by a 10<sup>4</sup>-A, 3-nsec e-beam source (Febatron 706), the peak gain for the P<sub>20</sub> line has been calculated to be 2.2 percent/cm.

A 20-cm<sup>3</sup> CO<sub>2</sub> laser device has been constructed to operate at 10 atm, and experiments with this laser will commence when the Febatron 706 is available as a longitudinal e-beam source.

Measurements and evaluation of data have been completed on the Lamb dip for 16 different rotational-vibrational transitions in sealed-off CO lasers operating at a total pressure of 1.5 torr.

## II. OPTICAL MEASUREMENTS AND INSTRUMENTATION

In the ZnS upconversion process, AC effects have been measured using chopped IR radiation as a source and constant UV illumination for excitation. The AC SNR is 1 to 2 orders of magnitude worse than the SNR obtained in previous measurements where the phosphor is exposed to DC IR radiation after (not during) UV excitation. Apparatus to determine the S/N characteristics of the phosphor screen resolution elements is being constructed.

Measurements have been made relevant to the imaging quality of a cooled 4-inch-diameter, 3-element refractor camera. Tests have demonstrated the mechanical integrity of the design and its diffraction-limited performance in the wavelength range of 7.5 to 12 $\mu$ m. Extraneous radiation at angles about 18° off the optical axis has been observed, and some effort has been made to determine the cause of these peaks.

The shearing interferometer was employed on board the NKC-135 aircraft with auxiliary optics suspended from a window-mounted air-foil plate to measure the modulation transfer function of the local boundary layer within 25 cm of the aircraft skin. The existence of image degradation due to a boundary layer was established.

Stellar images recorded in high-altitude flight with a diffraction-limited, long-focal-length telescope have been analyzed to determine the possible effects of the tropopause in image degradation. The results suggest that the difference between the stratosphere and troposphere is not measurable in the presence of boundary-layer turbulence, and a determination of turbulence effects agrees quite well with interferometer results measured separately.

Detailed tunable diode laser studies have been made of the  $v_1$  band of SO<sub>2</sub> centered around 8.7 $\mu$ m. Comparison between the experimental results and theoretical predictions based on microwave data has resulted in the establishment of a more accurate value for the band center frequency. Characteristics of the absorption spectra under varying conditions of temperature and pressure are used to determine optimum wavelengths for monitoring applications.

Several extensions of tunable diode laser techniques to air-pollution monitoring are described. The sensitivity of acousto-optic absorption cells and direct transmission measurements for air-pollution monitoring have been compared; real-time, quantitative, in-situ measurements of auto exhaust have been made and are reported; and long path laser transmission studies of ambient air pollution are described.

## III. LASER IMAGING RADAR

The 10.6- $\mu$ m imaging radar has been used to measure cross-section characteristics of two satellite models and a Terrier radome.

## Introduction

A simple, portable modulation-transfer-function (MTF) instrument based on a Sielman's star reticle has been built and tested. Under laboratory conditions, the instrument has demonstrated diffraction-limited performance. In the field, the atmospheric MTF has been measured under a wide variety of conditions in support of atmospheric spatial coherence measurements which were being made with a 48-inch telescope at  $10.6\mu\text{m}$ .

Electronics have been constructed both for control of the MTF instrument and for processing of the output signal. The MTF processor provides a calibrated output voltage proportional to the percentage modulation. Various control circuits for the Firepond laser radar have also been designed and implemented.

Spatial coherence measurements have been made at  $10.6$  and  $0.63\mu\text{m}$ . The data at  $10.6\mu\text{m}$  are currently being reduced, but qualitatively agree with the results obtained at  $0.63\mu\text{m}$ . These latter data, taken over a 5.4-km horizontal path at an average 68 m above the ground, indicate that the coherence diameter  $r_0$  ( $0.63\mu\text{m}$ ) for a wide variety of atmospheric conditions varies from  $1\text{ cm} < r_0$  ( $0.63\mu\text{m}$ )  $< 20\text{ cm}$ . From this, we predict that the  $10.6\mu\text{m}$  data will reveal  $30\text{ cm} < r_0$  ( $10.6\mu\text{m}$ )  $< 6\text{ m}$  for this path.

A  $10.6\mu\text{-m}$  isolator has been fabricated using Faraday free-carrier rotation. The isolator has a forward insertion loss of  $2\text{ dB}$ , a total reverse loss of  $22\text{ dB}$ , and a maximum throughput power of  $30\text{ W CW}$ .

# REPORTS ON OPTICS RESEARCH

1 January through 30 June 1972

## PUBLISHED REPORTS

### Final Technical Report

Development and Application  
of Tunable Diode Lasers to the  
Detection and Quantitative  
Evaluation of Pollutant Gases      E. D. Hinkley      30 September 1971

### Journal Articles\*

#### JA No.

3797	Conductivity Studies in Europium Oxide	M. R. Oliver J. O. Dimmock A. L. McWhorter T. B. Reed	Phys. Rev. B <u>5</u> , 1078 (1972), DDC AD-737932
3834	Detection of Air Pollutants with Tunable Diode Lasers	E. D. Hinkley P. L. Kelley	In <u>Clearing the Air: The Impact of the Clean Air Act on Technology</u> , J. C. Redmond, J. C. Cook and A. A. J. Hoffman, Eds. (IEEE Press, New York, 1971), pp. 76-80
3958	Pulsed Laser Sensitometer	R. W. O'Neil H. Kleiman P. F. Kellen†	Appl. Opt. <u>11</u> , 692 (1972), DDC AD-742622
3962	Experiment on Cross Relaxation in CO <sub>2</sub>	H. Granek C. Freed H. A. Haus†	IEEE J. Quantum Electron. <u>QE-8</u> , 404 (1972), DDC AD-743824
3976	TEA Laser Medium Diagnostics	R. W. O'Neil R. J. Carbone H. Granek H. Kleiman	Appl. Phys. Letters <u>20</u> , 461 (1972)
4006	Tunable-Laser Spectroscopy of the ν <sub>1</sub> Band of SO <sub>2</sub>	E. D. Hinkley A. R. Calawa P. L. Kelley S. A. Clough†	J. Appl. Phys. <u>43</u> , 3222 (1972)
4017	A Look at Photon Detectors	R. J. Keyes R. H. Kingston	Phys. Today <u>25</u> , 48 (1972), DDC AD-744912
4022	Excitation of a Long-Pulse CO <sub>2</sub> Laser with a Short-Pulse Longitudinal Electron Beam	S. Marcus	Appl. Phys. Letters <u>21</u> , 18 (1972)

\* Reprints available.

† Author not at Lincoln Laboratory.

Reports

JA No.

MS-3146	Infrared Detectors and Applications	J.O. Dimmock	J. Electronic Materials <u>1</u> , 255 (1972)
MS-3188	Designs and Experiments Relating to Stable Gas Lasers	C. Freed	Proceedings of Seminar on Frequency Standards and Metrology, University of Laval, Quebec, Canada, 30 August - 1 September 1971

\* \* \* \*

UNPUBLISHED REPORTS

Journal Articles

JA No.

4040	Tunable Infrared Lasers and Their Applications to Air Pollution Measurements	E.D. Hinkley	Accepted by Opto-Electronics
4041	The Feasibility of Producing Laser Plasmas via Photoionization	A. Javan* J.S. Levine	Accepted by IEEE J. Quantum Electron.

Meeting Speeches<sup>†</sup>

MS No.

3278	Numerical Computation of Pulse Propagation	L.C. Bradley J. Herrmann	VII International Quantum Electronics Conference, Montreal, 8-11 May 1972
3280	Studies of Breakdown in Air Induced by a Pulsed CO <sub>2</sub> Laser	L.C. Marquet R.J. Hull D.E. Lencioni	
3281	Lamb Dip in Sealed-Off CO Lasers	C. Freed* H.A. Haus*	
3297	Gain and Relaxation Studies in Transversely Excited HF Lasers	S. Marcus R.J. Carbone	3rd Conference on Chemical and Molecular Lasers, St. Louis, Missouri, 1-3 May 1972

\* Author not at Lincoln Laboratory.

† Titles of Meeting Speeches are listed for information only. No copies are available for distribution.

MS No.

3349	Tunable Infrared Laser Techniques for Air Pollution Detection	E. D. Hinkley	Optical Society of America, New York, 13 April 1972; Seminar, Naval Research Laboratories, Washington, D. C., 26 May 1972; Seminar, NOAA National Environmental Satellite Service, Suitland, Maryland, 26 May 1972; Symposium on Molecular Structure and Spectroscopy, Ohio State University, 12 June 1972
3352	Numerical Calculation of Turbulent Propagation	L. C. Bradley J. Herrmann	Optical Society of America, New York, 11-13 April 1972
3390	The Feasibility of Producing Laser Plasmas via Photoionization	J. S. Levine A. Javan*	Device Research Conference, Edmonton, Alberta, Canada, 21-23 June 1972

---

\* Author not at Lincoln Laboratory.

# ORGANIZATION

## OPTICS DIVISION

R. H. Rediker, *Head*  
R. S. Cooper, *Assistant Head*  
M. J. Hudson, *Assistant*

## LASER TECHNOLOGY

S. Edelberg, *Leader*  
L. C. Marquet, *Associate Leader*

Bradley, L. C.	Kafulas, P.	Morency, A. J.
Brennan, M. J.	Kilcline, C. W.	O'Neil, R. W.
Bushee, J. F., Jr.	Kleiman, H.	Pirroni, J. S.
Carbone, R. J.	Kromer, R.	Pitts, R. F.
Ferdinand, A. P., Jr.	Lencioni, D. E.	Ross, A. H. M.
Granek, H.	Levine, J. S.	Shey, S. Y.
Herrmann, J.	Lowder, J. E.	Theriault, J. R.
Johnson, J. Q.	Marcus, S.	

## ADVANCED SENSORS

J. O. Dimmock, *Leader*  
E. S. Cotton, *Associate Leader*  
T. M. Quist, *Assistant Leader*

Ariel, E. D.	Hinkley, E. D.	Scouler, W. J.
Bielinski, J. W.	Kelsall, D.	Stack, T. E.
Dickey, D. H.	Merrill, E. R.	Sullivan, F. M.
DiMarzio, E. W.	Nork, L. P.	Thomas, M. A.
Edwards, D. M.	Perry, F. H.	Wainwright, E. S.
Ellis, R. H.	Pike, H. A.	Ziegler, H. L.
Fulton, M.	Sunple, J. O.	Zwicker, H. R.

## OPTO-RADAR SYSTEMS

A. B. Gschwendtner, *Leader*

Bauer, J. H.	Coles, R. M.	Longaker, P. R.
Billups, R. R.	Dyjak, C. P.	McPhie, J. M.
Brownson, J. S.	Garavano, L. A.	Stevens, R. R.
Bryant, B. W.	Hull, R. J.	Zieman, H. E.
Cluy, W. G.		

## LASER SYSTEMS

R. H. Kingston, *Leader*  
L. J. Sullivan, *Associate Leader*

Bates, D. H.	Gilmartin, T. J.	O'Donnell, R. G.
Bicknell, W. E.	Holtz, J. Z.	Purker, A. C.
Capes, R. N., Jr.	Mulling, L. R.	Swezey, L. W.
Chanik, L. W.	Marapoti, J. V.	Teoste, R.
Daley, J. A., Jr.	Mehlhorn, H. A.	Zimmerman, M. D.
Freed, C.	Munoz-Flores, J.	

## I. LASER TECHNOLOGY AND PROPAGATION

### A. CW THEORY

#### 1. Laser Propagation Through a Turbulent Medium

In previous reports, we discussed the propagation of a high-power laser beam through a nonturbulent atmosphere. In the past six months, we have extended our capabilities to include propagation through a turbulent atmosphere.

The standard approach to the calculation of propagation of a low-power beam through a turbulent medium is by analytic computation of ensemble average values of various quantities. (A good review of this field is found in Ref. 1.) However, since analytic methods had not been successful in the high-power, nonturbulent case, another approach was needed. We accomplished this by simulating individual realizations of the atmosphere, with the constraint that the ensemble of these realizations should have the statistical properties of an accepted (or at least, widely used) model of the turbulent atmosphere. In the following section, we argue that the velocity turbulence of the atmosphere is of little importance except in the case of an extremely high-power beam, and that for the majority of cases it is an adequate approximation simply to add the naturally occurring temperature (or index) fluctuations to the temperature (or index) change induced by the beam itself. Since our numerical method is capable of computing the propagation through an arbitrary atmosphere (so long as the index gradients are not excessive), the only remaining problem is the generation of suitable realizations of the temperature fluctuations.

For our purposes, sufficient information about the statistical properties of the index of refraction is contained in the autocorrelation function  $\langle n(\vec{r}) n(\vec{r} + \vec{p}) \rangle$ . If the atmosphere is considered to be statistically homogeneous, this function is independent of  $\vec{r}$ , and can be described equally well by the (three-dimensional) spectrum

$$\Phi_3(\vec{k}) = \frac{1}{(2\pi)^3} \int d^3 p e^{i\vec{k} \cdot \vec{p}} \langle n(\vec{r}) n(\vec{r} + \vec{p}) \rangle .$$

This spectrum is generally used for the statistical description of the atmosphere. But in our propagation calculations, the quantity  $n$  does not enter directly, but only as an integral,  $\int n dz$ . To this integral corresponds a two-dimensional spectrum:

$$\Phi_2(k_x, k_y) = \frac{1}{(2\pi)^2} \iint_{-\infty}^{\infty} dx dy \exp[i(k_x x + k_y y)] \left\langle \int_{z_1}^{z_1 + \Delta z} n(\vec{r}) dz \int_{z_1}^{z_1 + \Delta z} n(\vec{r} + \vec{p}) dz \right\rangle .$$

It is easy to show that  $\Phi_2$  is related to  $\Phi_3$  by the equation

$$\Phi_2(k_x, k_y) = (\Delta z)^2 \int dk_z \Phi_3(k_x, k_y, k_z) [j_0(k_z \Delta z / 2)]^2$$

where  $j_0(u) \equiv \sin u/u$ .

Section I

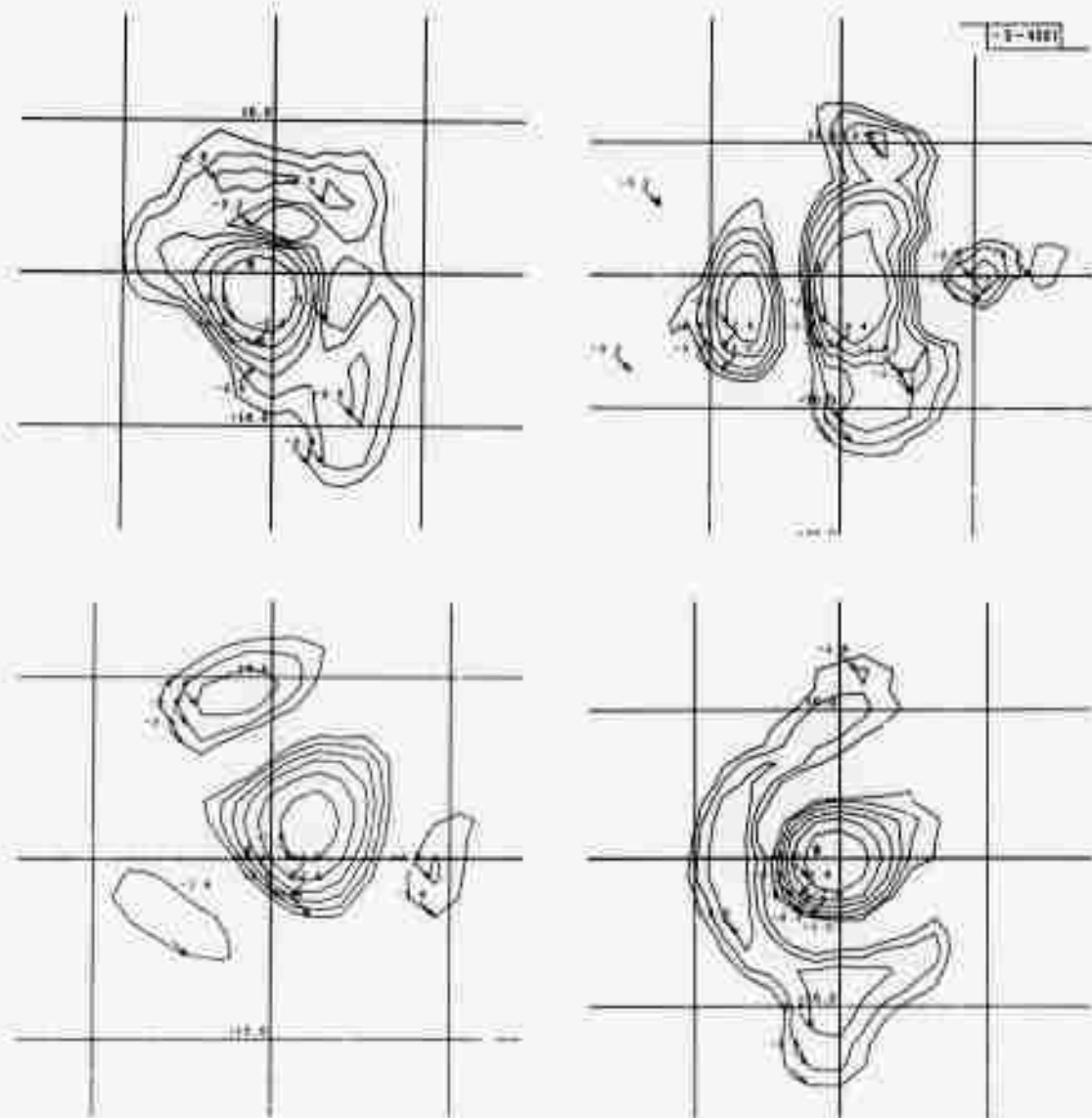


Fig. I-1. Iso-irradiance contour plots for conditions corresponding to Firepond facility: 122-cm Cassegrainian (0.33 obscuration ratio) focused at 5.4 km,  $\lambda = 10.6 \mu\text{m}$ . Turbulence is assumed to be homogeneous and isotropic, with  $C_n^2 = 2 \times 10^{-14} \text{ m}^{-2/3}$ . Four different realizations. Grid spacings are 10 cm.

We now wish to generate values of  $\int n dz$  on a finite two-dimensional grid. We do this by generating an array of random complex numbers  $q_{m,n}$  with zero mean and Gaussian distribution in the space  $k_x, k_y$ , multiplying by the required function of  $k_x, k_y$ , and taking a Fourier transform:

$$\int n dx = \frac{(2\pi)^2}{L_x L_y} \sum_{m,n} \exp\left[2\pi i \left(\frac{mx}{L_x} + \frac{ny}{L_y}\right)\right] q_{mn} \sqrt{S_2\left(\frac{2\pi m}{L_x}, \frac{2\pi n}{L_y}\right)}$$

where  $L_x$  and  $L_y$  are the total widths of the grid in the  $x$ - and  $y$ -directions, respectively.

Requiring a least-mean-square fit of  $\int n dz$  based on a finite grid to the continuum expression, one can show that a convolution is necessary in order to take proper account of frequencies present in the continuous spectrum  $\Phi_2$ , but not present in the spectrum  $S_2$  for the discrete wave-numbers  $k_x = 2\pi m/L_x$  and  $k_y = 2\pi n/L_y$ .  $S_2$  is then related to  $\Phi_2$  by

$$S_2(k_x, k_y) = \frac{L_x^2 L_y^2}{(2\pi)^4} \iint_{-\infty}^{\infty} dk'_x dk'_y \Phi_2(k'_x, k'_y) \left\{ j_0\left[\frac{(k_x - k'_x)L_x}{2}\right] j_0\left[\frac{(k_y - k'_y)L_y}{2}\right]\right\}^2 .$$

We use the scheme described above to generate an array of phase changes (proportional to  $\int n dz$ ) twice for every step in  $z$ , in accordance with our method of calculation.<sup>2</sup> The arrays are taken to be statistically independent of one another, since the  $z$ -steps actually used are considerably larger than the outer scale of turbulence, except in the immediate vicinity of a focus where the small optical lever arm makes phase changes of little importance. For the same reason, we believe that the assumption of a Gaussian distribution for the phase changes is justified. For the spectrum  $\Phi_3$ , we have used the modified von Kármán spectrum in the form

$$\Phi_3(k) = 0.033 C_n^2 \left[k^2 + \left(\frac{2\pi}{L_o}\right)^2\right]^{-11/6} \exp[-(kL_o/2\pi)^2]$$

where  $L_o$  is the outer scale, and  $L_o$  is the inner scale of turbulence.

Figure I-1 shows some iso-irradiance contour plots that result when we apply our method to a particular experimental situation, without nonlinear effects. Each plot corresponds to an instantaneous picture of the beam, and the variation from one plot to another is due to the statistical fluctuations of the assumed atmosphere.

As overall measures of the effect of turbulence, we have chosen two quantities. One is the equivalent area, defined as

$$A_{eq} \equiv \frac{\left(\int I dx dy\right)^2}{2 \int I^2 dx dy} .$$

For well-behaved intensity patterns, the equivalent area so defined agrees with the area defined by

$$A_{rms} = \pi \int [(x - \bar{x})^2 + (y - \bar{y})^2] I dx dy / \int I dx dy$$

based on the standard deviations. But for the Airy pattern, the rms area diverges whereas the equivalent area gives a reasonable value. In addition, the standard deviations cannot be reliably calculated for noisy experimental data, since the weighting of the intensity with  $r^3$  (as can be seen by putting the integral into cylindrical coordinates) leads easily to numerical difficulties for large  $r$ . We therefore prefer to use the equivalent area. This is usually divided by the

Section I

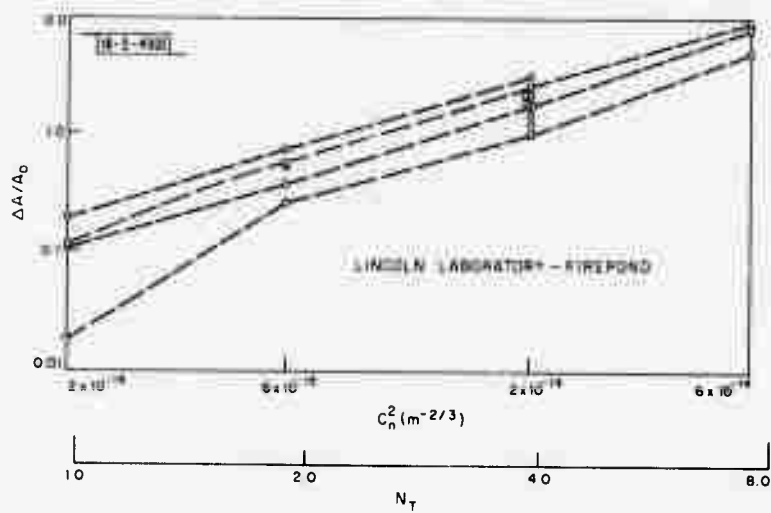


Fig. I-2. Beam spread as a function of  $C_n^2$ , same conditions as in Fig. I-1.

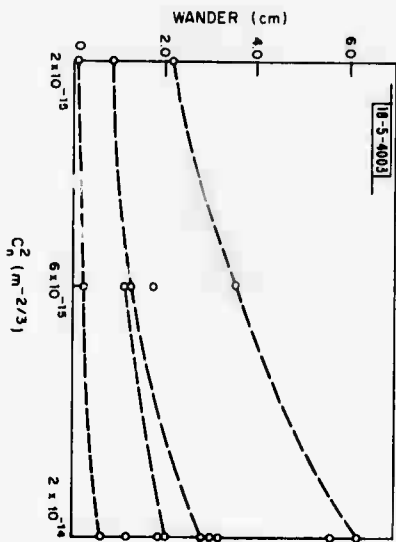


Fig. I-3. Wander as a function of  $C_n^2$ , same conditions as in Fig. I-1.

corresponding quantity in the absence of turbulence  $A_o$ , and a nondimensional "beam spread" is defined:

$$\sigma_A^2 \equiv (A_{eq} - A_o)/A_o$$

The other quantity is the displacement of the center of irradiance of the pattern:

$$w_x \equiv \int x I dx dy / \int I dx dy$$

$$w_y \equiv \int y I dx dy / \int I dx dy$$

and the nondimensional "wander" (squared) is defined as

$$\sigma_w^2 \equiv \pi(w_x^2 + w_y^2)/A_o$$

In Figs. I-2 and I-3, we plot the values of these quantities as a function of  $C_n^2$ , the measure of the strength of turbulence. At a given value of  $C_n^2$ , the different points correspond to different realizations of the atmosphere. Points that are connected by dashed lines correspond to realizations that differ only by the value of  $C_n^2$ ; i.e., the random numbers used to generate the realizations are the same.

The fact that these dashed lines are nearly parallel to one another suggests that it may be possible to study the dependence of turbulent propagation on various parameters by maintaining a single set of random numbers and varying the parameters, without having to accumulate a large number of statistics for each set of parameters. This possibility is made more plausible by an examination of the contour plots of Figs. I-4 and I-5, which result from just such a study, where a set of dimensionless numbers appropriate for this problem have been chosen and varied systematically. The dimensionless numbers are the Fresnel number

$$N_F \equiv k_o a_m^2 / L$$

the f/number

$$f/ \equiv L/2a_m$$

the "turbulent distortion number"

$$N_T \equiv a_m (k_o^2 C_n^2 L)^{3/5}$$

and the ratios  $a_m/L_o$  and  $a_m/l_o$ . Here,  $a_m$  is a characteristic radius in the initial plane,  $k_o$  is the optical wavenumber, and both the initial radius of curvature and the distance to the plane of observation are taken to be 1. For Figs. I-4 and I-5, the parameter  $N_T$  has been kept constant, while the other parameters are varied. From the "family resemblance" of the plots, it seems clear that scaling laws can be deduced in this way and that  $N_T$  is the most important parameter in the range studied. Its effect on the beam spread and wander are already visible in Figs. I-2 and I-3; Figs. I-6 and I-7 show the effects of varying  $N_F$ .

We can now proceed to compute the propagation of a high-power beam through a turbulent atmosphere. In Fig. I-8, we see a comparison of results for a high-power beam propagating

## Section I

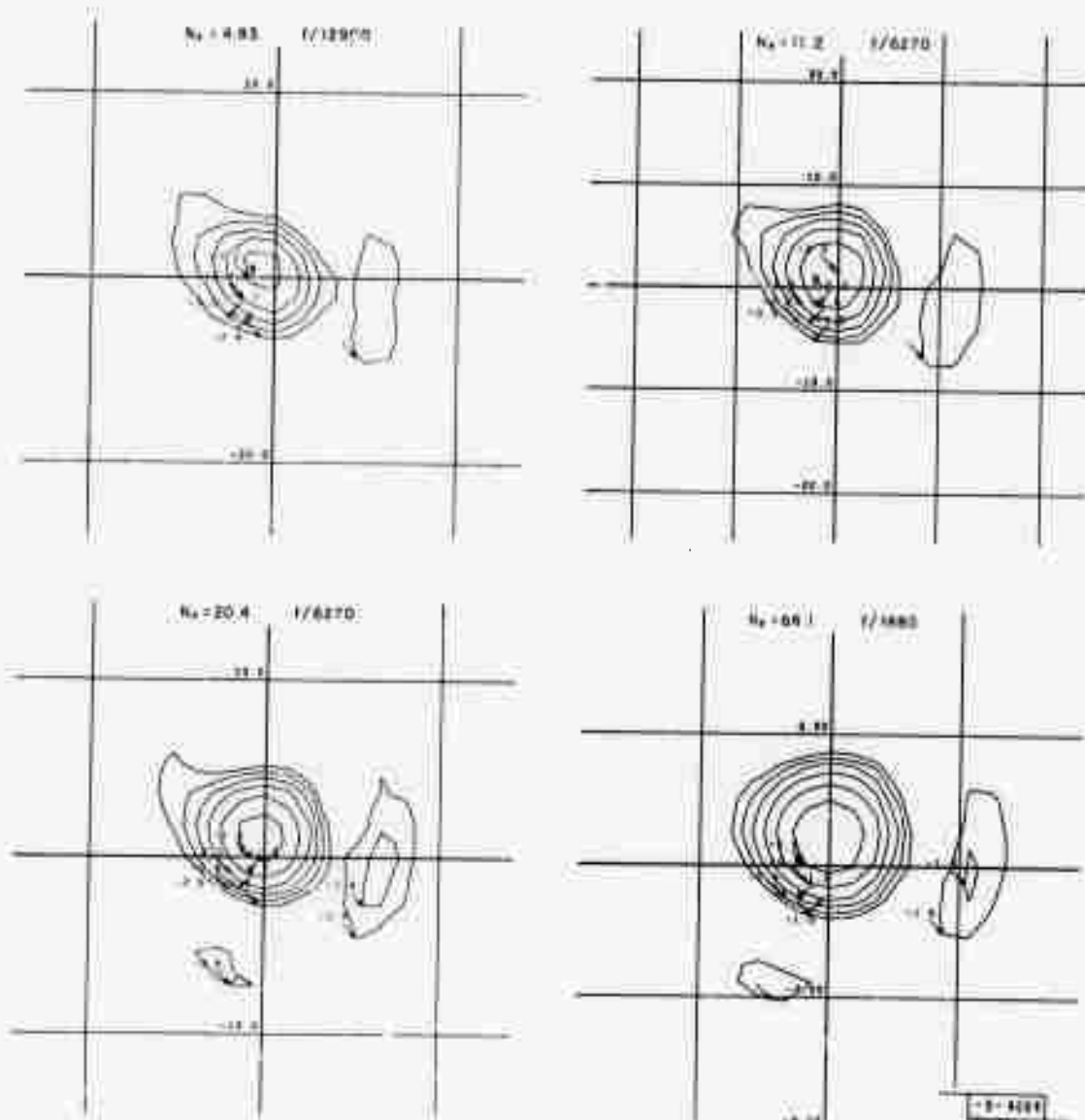


Fig. I-4. Iso-irradiance contours for geometry of Fig. I-1, with  $N_T = 1.86$  and various values of  $N_F$  and  $f/$ .

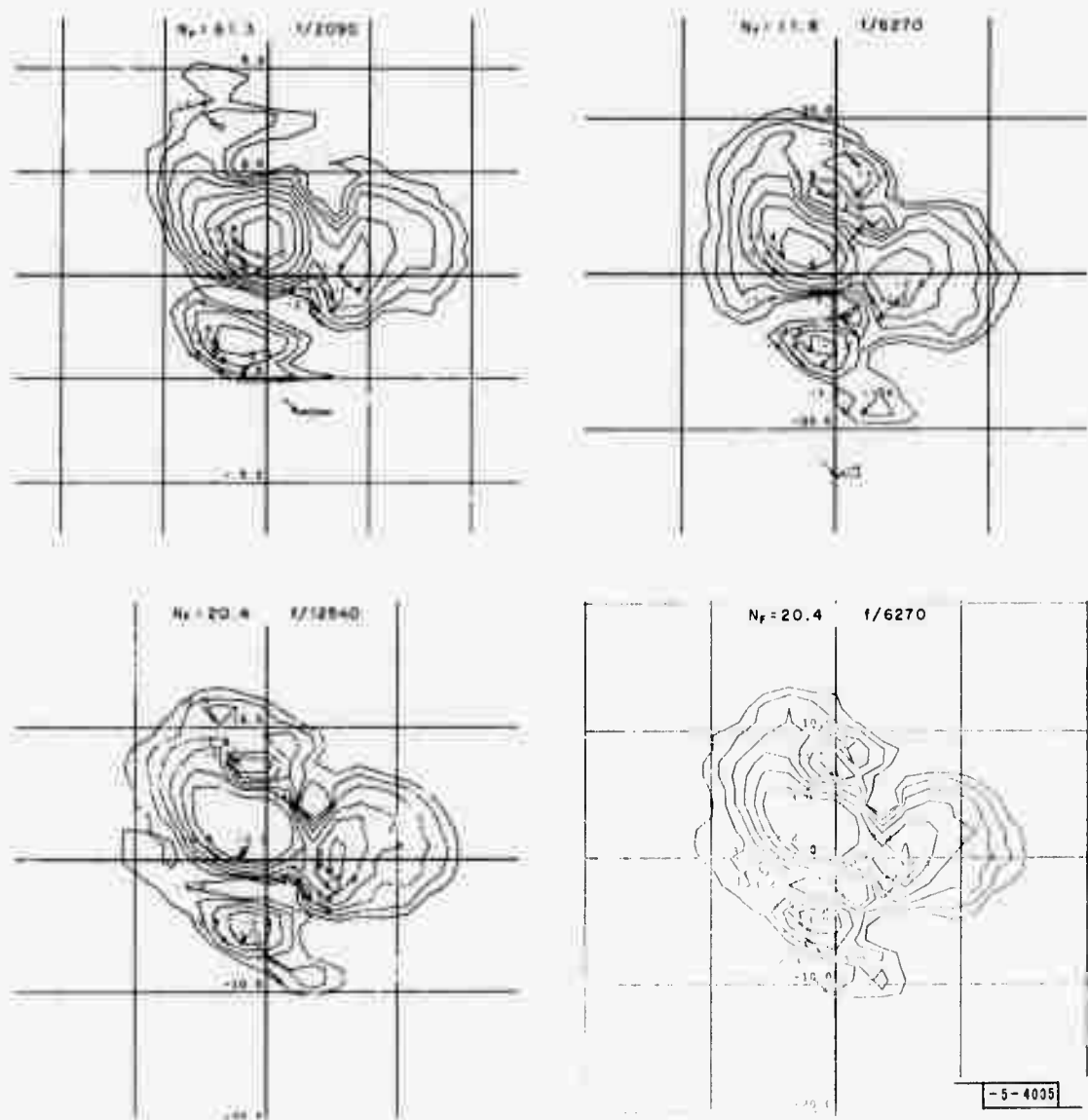


Fig. I-5. Iso-irradiance contours for geometry of Fig. I-1, with  $N_T = 3.83$  and various values of  $N_F$  and  $f/$ .

## Section I

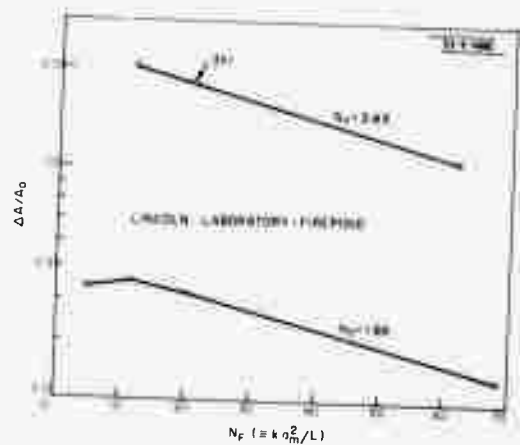


Fig. I-6. Beam spread as a function of  $N_F$ ,  
Firepond geometry.

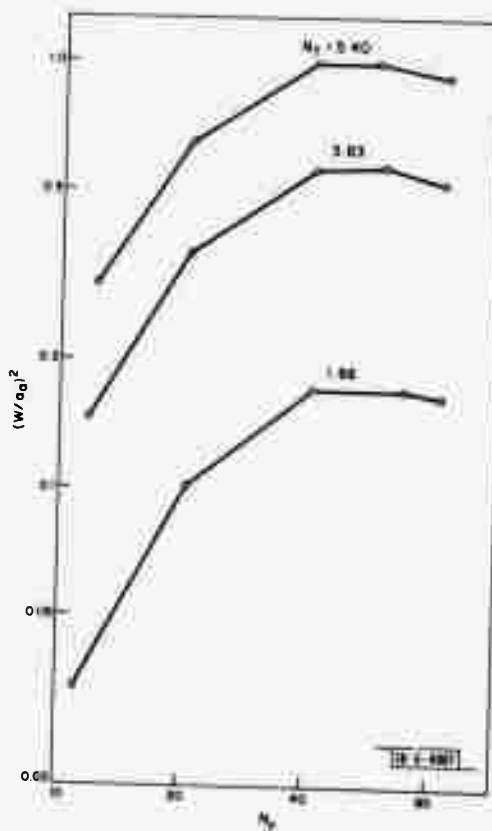


Fig. I-7. Wander as a function of  $N_F$ ,  
Firepond geometry.

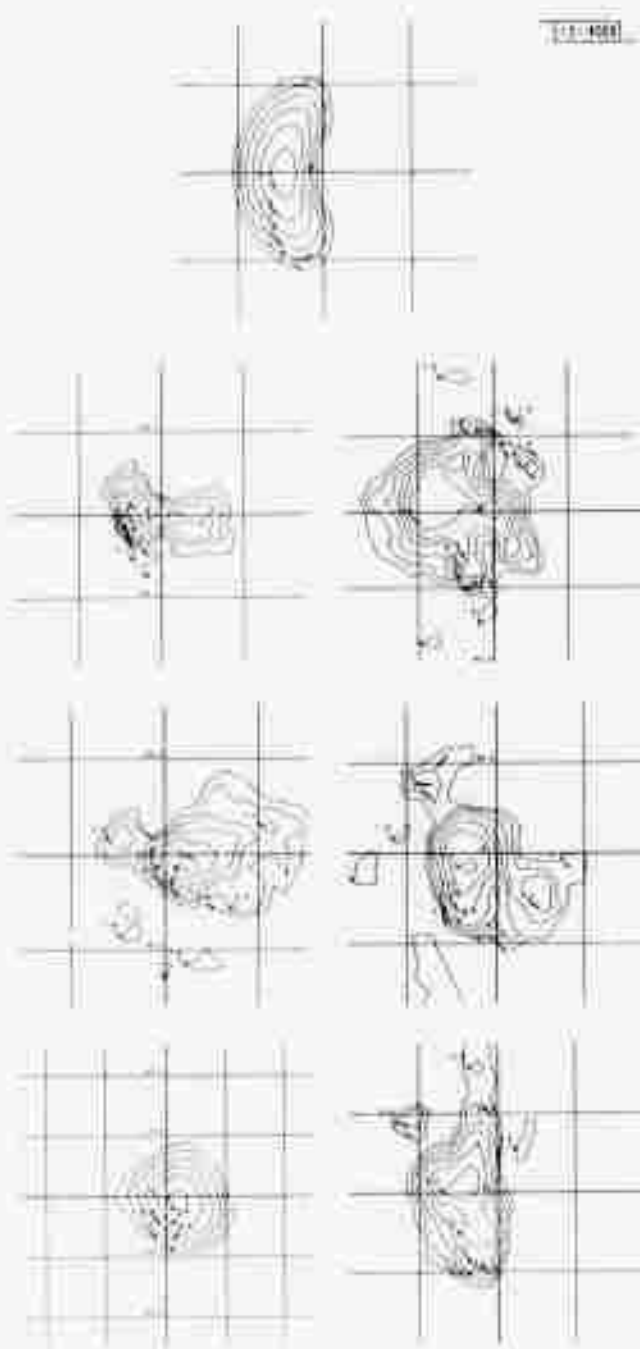


Fig. I-8. Thermal blooming in presence of turbulence. Top contour plot shows beam with turbulence absent and thermal blooming present. Left three contour plots show beam in absence of thermal blooming, after propagation through three realizations of turbulent atmosphere ( $C_n^2 = 10^{-14} \text{ m}^{-2/3}$ ). Right three contour plots show thermally blooming beam after passing through same three realizations of turbulent atmosphere. Initial beam was an infinite Gaussian,  $1/e^2$  power diameter 1 m, focused and observed at range of 10 km,  $\lambda = 10.6 \mu\text{m}$ , and  $\sigma P/v_w = 10^{-4}$ .

## Section I

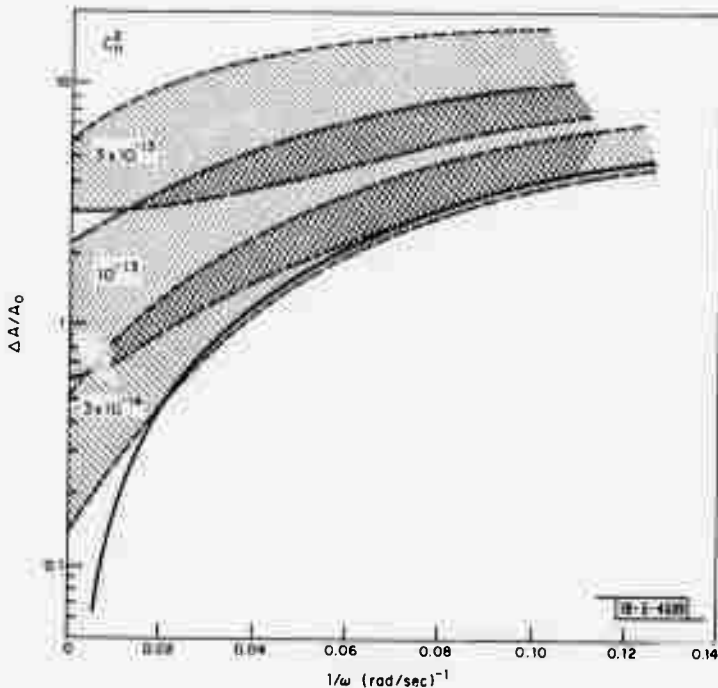


Fig. I-9. Total loss (thermol blooming plus turbulence) as a function of slewing rate. Solid line shows loss in absence of turbulence, while hatched areas show range of loss associated with various values of  $C_n^2$ . Infinite Gaussian,  $1/e^2$  power diameter 1 m, range 3 km,  $\lambda = 20 \mu\text{m}$ ,  $\sigma P/v_w = 10^{-4}$ .

through the same turbulent atmosphere. Figure I-9 shows the intensity loss when turbulence and thermal blooming are combined, for a particular example. More detailed studies are under way.

L. C. Bradley  
J. Herrmann

### 2. Interaction of Heating and Turbulence in Thermal Blooming

In our calculation of the propagation of a high-power beam through a turbulent atmosphere, we assumed that the temperature variations due to heating may be simply added to those already present in the atmosphere. It has been suggested that the interaction between heating and turbulence may give rise to additional temperature variations sufficiently large that the propagation will be significantly affected. Two mechanisms have been proposed:

- Warmer blobs have a larger absorption coefficient than cooler ones, so heating will tend to amplify the variations.
- Velocity fluctuations in the medium will tend to cool off the heated air more effectively, and also will cause further temperature fluctuations.

Our purpose here is to estimate these effects and show that both are negligible, at least at presently contemplated power levels.

We assume that wind velocities are much smaller than the sound velocity, so that the pressure may be considered constant. The temperature is thus considered a passive additive to the turbulent velocity field. If the winds are not so slow, the heating effects will be negligible anyhow. Then, the equation of energy conservation may be written as

## Section I

$$\frac{\partial T}{\partial t} + \vec{v} \cdot \nabla T = \frac{\alpha I}{\rho c_p} . \quad (I-1)$$

We assume the properties of the radiation source to be independent of time (or slowly changing), and divide the properties of the medium into mean and fluctuating parts:

$$T = T_o + T_1 , \quad \vec{v} = \vec{v}_o + \vec{v}_1 , \quad \frac{\alpha}{\rho} = (\frac{\alpha}{\rho})_o + (\frac{\alpha}{\rho})_1 .$$

The mean parts are assumed to satisfy

$$\vec{v}_o \cdot \nabla T_o = (\frac{\alpha}{\rho})_o \frac{I}{c_p} . \quad (I-2)$$

To this might be added a term  $\overline{\vec{v}_1 \cdot \nabla T_1}$ , but we argue below that this term is negligibly small for practical application. Then we have

$$\frac{\partial T_1}{\partial t} + \vec{v}_o \cdot \nabla T_1 + \vec{v}_1 \cdot \nabla T_1 = (\frac{\alpha}{\rho})_1 \frac{I}{c_p} - \vec{v}_1 \cdot \nabla T_o - \frac{\partial T_o}{\partial t} . \quad (I-3)$$

We now separate that part of the random temperature field which can be considered as the frozen turbulence  $T_f$ , satisfying the Taylor hypothesis

$$\frac{\partial T_f}{\partial t} = -\vec{v}_o \cdot \nabla T_f .$$

Then, with  $T_1 = T_f + T_2$  we get

$$\frac{\partial T_2}{\partial t} + (\vec{v}_o + \vec{v}_1) \cdot \nabla T_2 = (\frac{\alpha}{\rho})_1 \frac{I}{c_p} - \vec{v}_1 \cdot \nabla T_o - \vec{v}_1 \cdot \nabla T_f - \frac{\partial T_o}{\partial t} . \quad (I-4)$$

In our propagation code (see Sec. A-1) in a turbulent atmosphere the contributions of  $T_o$  and  $T_f$  have been included. We must now estimate the contributions on the right-hand side of Eq. (I-4) to show that  $T_2$  is negligible.

The time for a fluid particle to cross the beam is  $\sim a/v_o$ , where  $a$  is the beam radius, so the increment in  $T_2$  is

$$\Delta T_2 \sim \frac{a}{v_o} \left[ (\frac{\alpha}{\rho})_1 \frac{I}{c_p} - \vec{v}_1 \cdot \nabla T_o - \vec{v}_1 \cdot \nabla T_f - \frac{\partial T_o}{\partial t} \right] .$$

We may compare the increment from the first term ( $\Delta_1 T_2$ ) to the rms value of  $T_f$  in the unperturbed fluid, which we call  $T_r$ :

$$\frac{\Delta_1 T_2}{T_r} \sim \frac{1}{T_r} \frac{a}{v_o} (\frac{\alpha}{\rho})_1 \frac{I}{c_p}$$

Now,

$$\frac{(\frac{\alpha}{\rho})_1}{(\frac{\alpha}{\rho})_o} \sim \frac{E}{kT} \frac{T_r}{T_o} \sim 6.5 \frac{T_r}{T_o}$$

## Section I

where  $E$  is the lower level of the laser transition, and  $I \sim P/\pi a^2$ , so we find

$$\frac{\Delta_1 T_2}{T_r} \sim \frac{6.5 \alpha_o P}{\pi p_o c_p T_o v_o a} .$$

For fairly extreme cases, this may amount to  $\sim 1$  percent, which we consider to be negligible.

It is not appropriate to compare the increment from the second term ( $\Delta_2 T_2$ ) with  $T_r$ , since under conditions of low lapse rate (at dawn or dusk) it is possible to have large velocity fluctuations and small temperature fluctuations. Instead, we compare it with  $\Delta T_o$ , the change in  $T_o$  in traversing the beam. It is easily seen that  $(\Delta_2 T_2 / \Delta T_o) \sim (v_r / v_o)$ , where  $v_r$  is the rms value of  $v_1$ . This is an overestimate of the effect, however, for the important quantity for propagation is not the change in temperature itself, but its integral over the length of the beam, which is proportional to the phase change. Since  $v_1$  is uncorrelated over paths greater than some outer scale  $L_o$ , while  $T_o$  adds coherently over the whole path, which we assume is much larger than  $L_o$ , we have

$$\int \Delta T_o dz \propto (\Delta T_o) (\Delta z)$$

$$\int \Delta_2 T_2 dz \propto (\Delta_2 T_2) (L_o \Delta z)^{1/2}$$

and the ratio of the corresponding phase changes is

$$\frac{\Delta_2 \varphi}{\Delta \varphi_o} \sim \frac{v_r}{v_o} \left[ \frac{L_o}{\Delta z} \right]^{1/2} .$$

At most,  $(v_r / v_o) \sim 0.1$ , while  $(L_o / \Delta z) \sim 0.01$  for the cases in which we are interested. Thus, we consider that this term too can be neglected.

The third term ( $\Delta_3 T_2$ ) describes the breakup of frozen turbulence. Since  $\nabla T_f \sim (T_r / L_o)$ , we find

$$\frac{\Delta_3 T_2}{T_r} \sim \frac{v_r}{v_o} \frac{a}{L_o}$$

which is negligibly small.

The fourth term ( $\Delta_4 T_2$ ) is the most difficult with which to deal. The time variation of  $T_o$  is due to the fact that turbulence in the initial parts of the beam leads to scintillations (time changes in  $I$ ) at later points in the beam. In general, the rapidly varying part of  $I$  has high spatial frequencies and therefore tends to integrate out in the equation for  $T_2$ , whereas the low spatial frequencies, which are the most important in contributing to  $T_2$ , are slowly varying. Furthermore, in a focused beam, the relevant time-scale  $a/v_o$  becomes smaller as the beam travels farther and as the scintillations thus become larger. Therefore,  $\Delta_4 T_2$  may not be as important as it appears at first glance. In an attempt to make these statements more quantitative, we are now carrying out "computer experiments" on low-power beams.

The above considerations apply to a beam of moderate dimensions ( $\gtrsim 1$  m) propagating through the atmosphere. Recently, Gebhardt, et al.<sup>3</sup> have studied thermal blooming in a turbulent medium in the laboratory. They have attempted to make  $v_o$  and  $T_f$  as small as possible, and the integral scale for their turbulent medium is on the order of a beam diameter.<sup>4</sup> For such an

environment, it is no longer permissible to neglect the term  $-\vec{v}_1 \cdot \nabla T_1$  in Eq. (I-2); the usual practice is to replace it by an eddy diffusion term  $\nabla \cdot (\kappa_e \nabla T_0)$  (see Ref. 5). While this is no doubt appropriate for their experiment, we believe that our order-of-magnitude analysis above shows that this term will not be important in the open atmosphere.

J. Herrmann  
L. C. Bradley

### 3. Calculations of Phase Correction for a Laboratory Thermal Blooming Experiment

In order to design a laboratory experiment for the study of the elimination of thermal blooming by an initial phase correction, a series of propagation calculations has been performed.

Figure I-10 shows the radius of the unbloomed beam near the focus for six aperture sizes. All cases assume a Gaussian beam truncated at this aperture size with a radius of curvature of 1 m. From Fig. I-10, the optimum experimental condition may be determined.

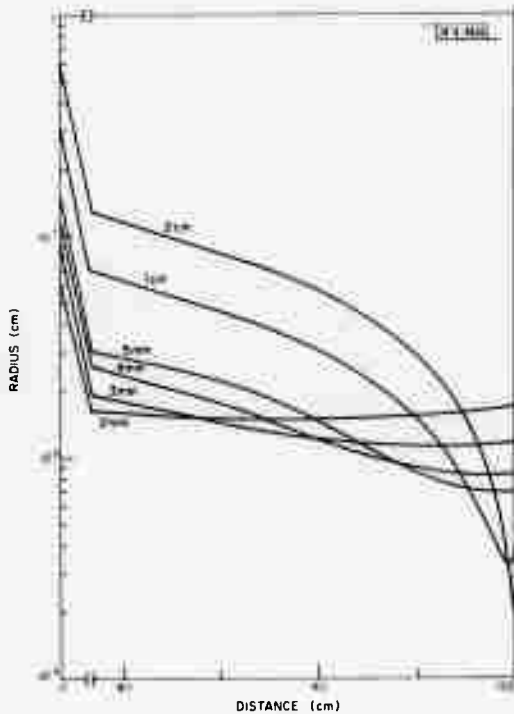


Fig. I-10. Equivalent radius of unbloomed beam for six aperture sizes. Gaussian beam is truncated at  $1/e^2$  power level and has wavefront curvature of 1-m radius. All curves apply to wavenumber  $k = 1.2 \times 10^5 \text{ cm}^{-1}$ .

Figure I-11 shows the 5-mm-aperture beam with thermal blooming (curve B). By applying an initial phase correction, thermal blooming is considerably reduced (curve C), approaching the unbloomed condition (curve A).

Figure I-12 shows the equivalent curves for a 2-mm-aperture beam.

J. Herrmann  
L. C. Bradley

## Section I

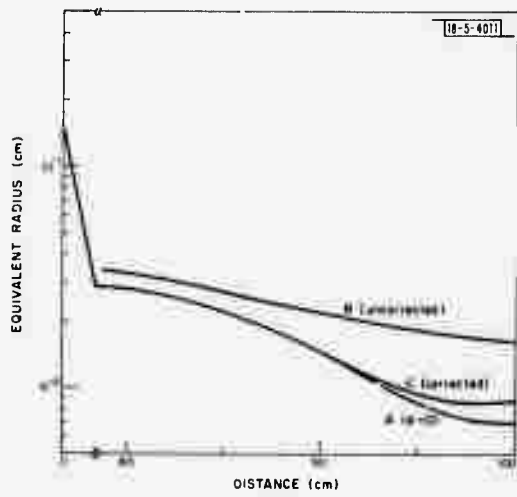


Fig. I-11. For a beam with a 5-mm-diameter aperture, curve A is the unbloomed case, curve B is with thermal blooming, and curve C is with initial phase correction. Blooming parameters are:  $P = 1 \text{ W}$ ,  $\alpha = 10^{-3} \text{ cm}^{-1}$ ,  $v = 0.2 \text{ cm/sec}$ , and  $\omega = 0.2 \text{ rad/sec}$ .

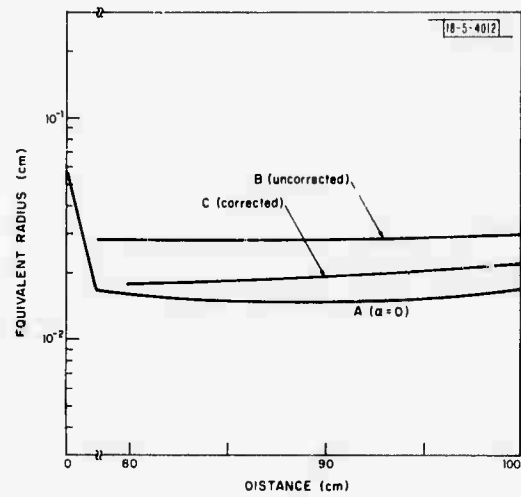


Fig. I-12. Same as Fig. I-11 for 2-mm-aperture beam. Blooming parameters also same, except  $v = 0.5 \text{ cm/sec}$  and  $\omega = 0.5 \text{ rad/sec}$ .

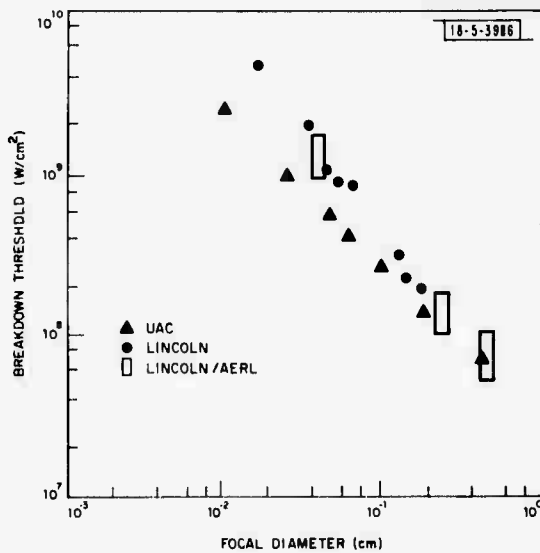


Fig. I-13. Breakdown thresholds measured for spot diameters 0.3 and 0.5 mm. Data for smaller spot size are from TEA laser results at Lincoln Laboratory and from Ref. 10.

## B. EFFECTS

### 1. Laser-Induced Air Breakdown

Several experiments were performed to investigate the effects of atmospheric dust on the breakdown threshold of 10.6- $\mu\text{m}$  laser beams with large focal spots.

#### a. AERL Breakdown Experiment<sup>6,7</sup>

In March 1972, we conducted a series of experiments at Avco Everett Research Laboratories (AERL) using their 1-kJ pulsed e-beam laser. This laser emitted a 10-  $\times$  20-cm beam which was from 1 to 2X diffraction-limited and had a peak pulse power  $\approx 4 \times 10^8$  W. With 25-m focusing optics, we were able to obtain breakdown at a maximum spot area of  $\approx 0.3 \text{ cm}^2$ . The focused power was varied by either changing the sustainer voltage or by inserting finely perforated screens with geometrical transmission of 0.70 and 0.5 in the beam. The threshold for breakdown was obtained to within a factor of approximately two. The results for large spot sizes are shown in Fig. I-13 together with Lincoln laboratory TEA laser results and the results from D. C. Smith.<sup>8</sup> As can be seen, the threshold continues to decrease at these spot sizes.

In general, for flux densities larger than the threshold, breakdown was not confined to the focal volume but instead consisted of a string of discrete breakdowns extending up the beam (Fig. I-14). The length of this string increased with increasing laser power, as shown in Fig. I-15. The breakdown string always extended well beyond the point where the beam flux was equal to the clean-air breakdown value ( $\approx 3 \times 10^9 \text{ W/cm}^2$ ). The minimum flux densities where breakdown occurred were  $\approx 10^7 \text{ W/cm}^2$ .

These results can be understood by assuming the discrete breakdowns are occurring off large dust particles in the beam. The size distribution of dust in the experimental area was monitored using a light scattering particle counter (Royco Model 225) and a 256-channel pulse-height analyzer (Northern Model NS-633). Particles in the size range 1 to 12  $\mu\text{m}$  could be measured in this way. A typical measured distribution is shown in Fig. I-16.



Fig. I-14. String of breakdowns extending from focal spot back toward laser.

Section I

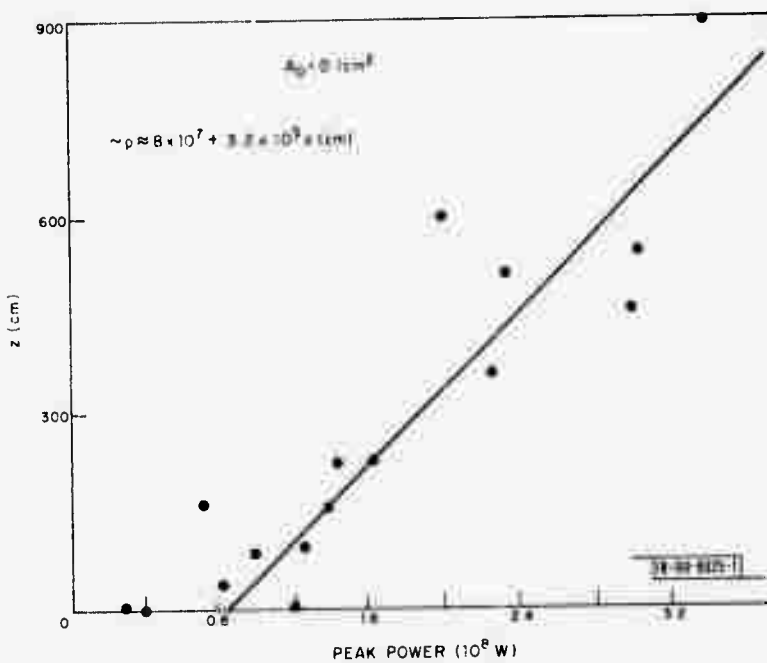


Fig. I-15. Maximum extent of breakdown string as a function of peak laser power.

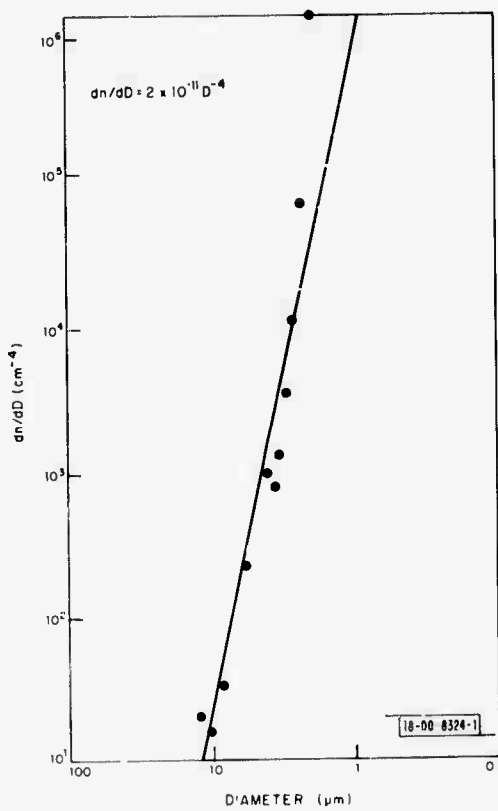


Fig. I-16. Measured dust-particle-size distribution.

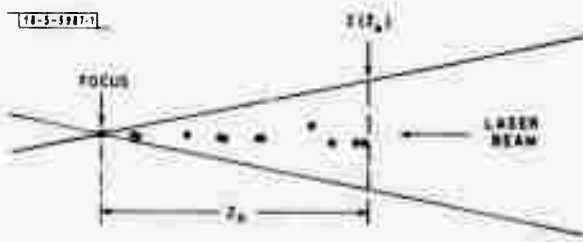


Fig. I-17. Beam geometry and notation. Breakdown string extends to position  $Z_o$  where flux density is  $I(Z_o)$ .

The functional dependence of the breakdown threshold on particle size can be obtained in the following way: Let  $I(Z_o)$  be the flux density at the furthest extent of the breakdown string  $Z_o$  (Fig. I-17). Assume that the breakdown is determined by the largest particle size  $D_o$  that can be present near this position. The density of particles of size  $D_o$  or larger is given by

$$N(D_o) = \int_{D_o}^{\infty} \frac{dn}{dD} dD \approx 10^{-11} D^{-3} \text{ cm}^{-3}$$

The largest particle that can be present near  $Z_o$  is given by the conditions

$$N(D_o) V(Z_o) \geq 10$$

where  $V(Z_o)$  is the volume of the laser beam from the focal spot to  $Z_o$ . That is, there will be a particle of size  $D_o$  near  $Z_o$  if there are approximately ten such particles in  $V(Z_o)$ . This gives  $D_o = f(Z_o)$  which, together with  $I(Z_o)$ , gives the threshold intensity on particle size shown in Fig. I-18. Note that the results for  $D_o$  are not very sensitive to the number of particles assumed to be present in  $V(Z_o)$ .

We conclude that the experimental results for breakdown threshold can be understood if the breakdown threshold depends on aerosol particle size in the manner shown in Fig. I-18.

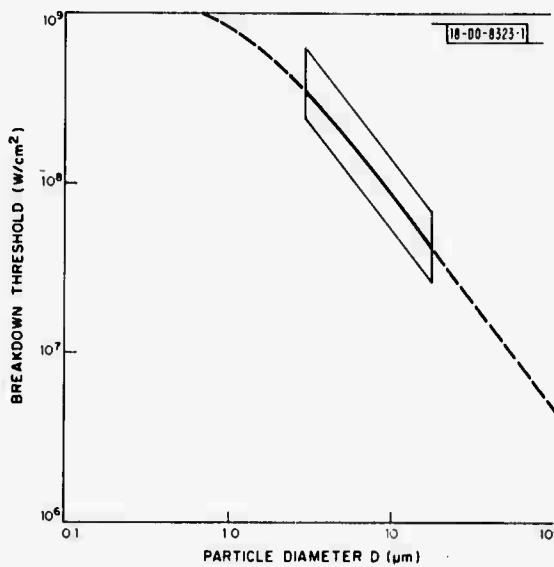


Fig. I-18. Particle-size dependence of breakdown threshold inferred from measured values of  $Z_o(P)$  and  $dn/dD$ .

Section I

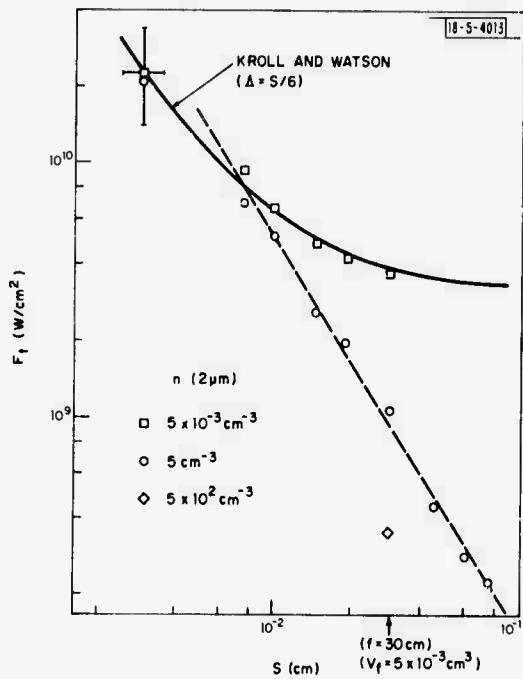


Fig. I-19. Breakdown threshold vs spot size for three different dust conditions.

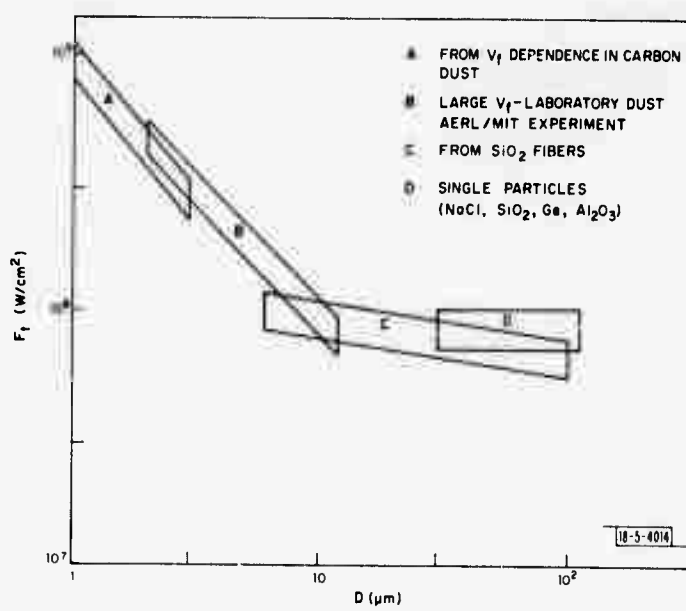


Fig. I-20. Summary of threshold dependence on particle from various methods.

### b. Breakdown Results with TEA Lasers<sup>7</sup>

It has been reported recently that the breakdown threshold for 10.6- $\mu\text{m}$  radiation decreases with increasing spot size well below the value predicted by classical microwave breakdown theory. We have verified the effect for focal spot sizes in the range  $10^{-2}$  to  $10^{-1}$  cm, but found that the threshold was sensitive to the amount of dust near the focal volume, especially at large spot sizes.

A chamber was designed and constructed which provided a variable atmosphere from dusty to highly filtered clean air. The dust count and size distribution within the chamber were monitored with a light scattering particle counter (Royco 225) and a 256-channel pulse-height analyzer (Northern NS-633). We were thus able to measure the size distribution in the range 1 to 12  $\mu\text{m}$ .

A series of threshold measurements was conducted in known atmospheres. For the very-clean-air case, the threshold approached an asymptotic value at large spot size which was close to that expected from microwave breakdown theory. Figure I-19 shows these data along with a theoretical curve obtained from Ref. 9. The focused spot was rectangular with dimensions  $S \times 5S$ . The fit to the data was for a diffusion length  $\Lambda = S/6$ . The other data in Fig. I-19 correspond to an atmosphere of carbon dust. As can be seen, the threshold continues to decrease with increasing spot size. The relative dust conditions for the three cases are indicated in the figure by the total density of particles with diameters larger than 2  $\mu\text{m}$ .

As in the previous section, these results can be explained by assuming that the breakdown threshold is determined by the largest particle present in the focal volume. Thus, for example, at  $S = 0.03$  cm in Fig. I-20 the three dust conditions give maximum particle sizes of 3, 1, and  $\ll 1$   $\mu\text{m}$  for the three data points. The inferred threshold dependence on particle size obtained in this way is shown in region A of the figure. Also shown are the results discussed in the previous section and the thresholds measured directly for thin glass fibers and single particles.<sup>10</sup>

The above results indicate that atmospheric aerosols can account for the threshold lowering at large spot sizes. Preliminary calculations of the cascade process in exploding particle vapors give the right order of magnitude as well as the particle-size dependence of the breakdown threshold.

Further work in this area will include studies of different material aerosols, some refinement of the theoretical models, and studies of the interaction of radiation with aerosols below the breakdown threshold.

D. E. Lencioni  
L. C. Marquet

## 2. Surface Interactions

### a. Impulse Delivery by a Pulsed Laser at 10.6 $\mu\text{m}$

Measurements and a correlation of impulse delivered to targets of various sizes and materials with the use of the AERL 1-kJ CO<sub>2</sub> laser are reported in this section. Some of these measurements and the experimental procedure are reported in detail elsewhere.<sup>11</sup>

The total impulse delivered to carbon and aluminum targets of different sizes was measured for focal spot areas of approximately 0.1 and 0.3 cm<sup>2</sup> (27-m focal-length mirror). AERL data<sup>12</sup> for aluminum and tungsten targets are also reported for focal spot areas of 0.02 and 0.6 cm<sup>2</sup> (10.6-m focal-length mirror). The delivered impulse was found to be independent of the target

## Section I

material (carbon, aluminum, and tungsten). There was no measurable mass loss from the aluminum targets ( $\Delta m < 10^{-4}$  g) and the mass loss from the carbon targets was less than  $10^{-3}$  g. The projected target areas ranged from 0.7 to  $40\text{ cm}^2$ .

A simple model based on an expanding cylindrical blast wave and a plasma front velocity proportional to the cube root of the power density is used to obtain impulse sealing relations. It is shown in Refs. 13 and 14 that the cylindrical-blast-wave relations can be modified to approximately account for time-dependent energy deposition. The shock-wave radius and the resulting pressure are shown to be proportional to the following relations:

$$R(t) \propto \left\{ \int_0^t [E_\ell(t)]^{1/2} dt \right\}^{1/2} \quad (I-5)$$

$$P(t) \propto E_\ell(t) \left\{ \int_0^t [E_\ell(t)]^{1/2} dt \right\}^{-1} \quad (I-6)$$

where the energy-per-unit-length  $E_\ell$  is defined as

$$E_\ell = \frac{E(t)}{\ell(t)} . \quad (I-7)$$

Here,  $E(t)$  is the total energy deposited in the plasma and  $\ell(t)$  is the distance the plasma front has moved away from the target during the time  $t$ . Then, for the case of a constant power density, we find

$$E_\ell \propto A_0(\bar{q})^{2/3} \quad (I-8)$$

where  $A_0$  is the focal spot area and  $\bar{q}$  is the average power density incident on the target. The impulse is given by

$$I \propto \int_0^\tau P(t) R(t)^2 dt \quad (I-9)$$

and for the case of a constant power density

$$I \propto A_0(\bar{q})^{2/3} \tau . \quad (I-10)$$

Two limiting cases may be identified which determine the termination of the impulse delivery  $\tau$ . For small free-standing targets, the impulse delivery ends when the cylindrical shock wave expands off the target. In this case, Eq. (I-5) yields  $\tau \propto A_T A_0^{-1/2} (\bar{q})^{-1/3}$ , where  $A_T$  is the target area. The impulse sealing relation is

$$I \propto A_T A_0^{1/2} (\bar{q})^{1/3} . \quad (I-11)$$

For an infinite target, the impulse delivery ends when the shock-wave pressure has decreased to about 1 atm. Then, Eq. (I-6) yields  $\tau \propto A_0^{1/2} (\bar{q})^{1/3}$  and the impulse sealing relation becomes

$$I \propto A_0^{3/2} (\bar{q}) = A_0^{1/2} \left( \frac{E}{\tau_0} \right) \quad (I-12)$$

where  $E$  is the total energy in the laser pulse and  $\tau_0$  is the pulse length.

The impulse normalized by the target area and the square root of the focal spot area are presented in Fig. I-21 as a function of the average power density as suggested by Eq. (I-11). The solid line is a least-squares fit to the data and has a slope of 0.27. The dashed line is fit to the data with a slope of  $1/3$  as predicted by Eq. (I-11). The scatter of the data makes it impossible to determine the precise power of the impulse dependence on the average power density, but a small exponent is indicated (i.e.,  $1/5$  to  $1/3$ ). It should be noted that, as pointed out in Ref. 13, the power density is only known to within about a factor of 3. Equation (I-11) indicates that the normalized impulse is relatively insensitive to the power density and correlates the data to within about a factor of 2.

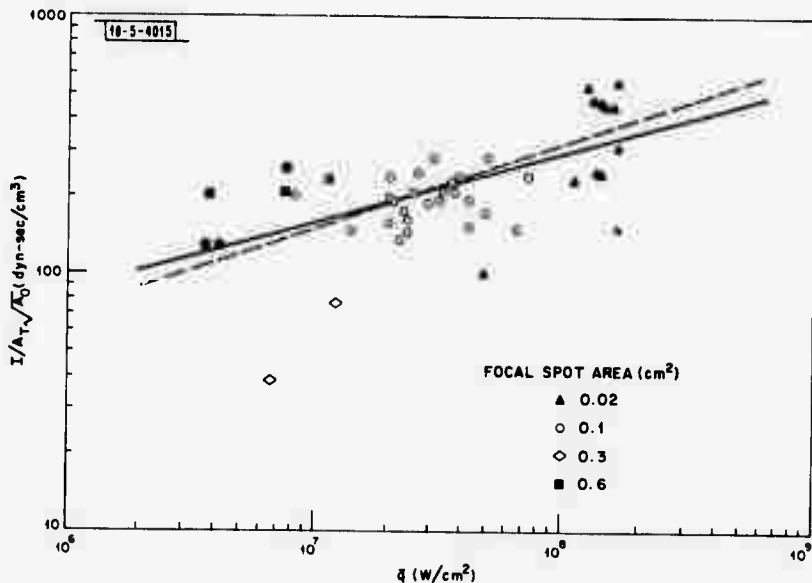


Fig. I-21. Plot of normalized impulse as a function of average power density for data obtained with use of AERL e-beam CO<sub>2</sub> laser. Solid symbols denote AERL data from Ref. 14. Solid line is least-squares fit to data,  $I/A_T \sqrt{A_o} = 2(\bar{q})^{0.27}$ ; dashed line is fit to data with slope of  $1/3$ .

Increasing the total energy above 300 J led to the formation of multiple aerosol-induced breakdowns in the laser beam. An open-shutter photograph of this effect is shown in Fig. I-22. The total impulse delivered to an effectively infinite target ( $40 \text{ cm}^2$ ) was measured on a number of runs both with and without the formation of aerosol-induced breakdowns. In Fig. I-23, the measured impulse is shown as a function of total energy in the laser pulse. The limited data show a linear increase of impulse with energy in agreement with Eq. (I-12) when multiple breakdowns were not observed, and an apparent saturation of delivered impulse when multiple breakdowns were observed. This interpretation of the data indicates that, with AERL machine pulse shape (an initial large spike), the increased energy above 300 to 400 J is being absorbed in the breakdowns and is decoupled from the target.\*

J. E. Lowder

\* An alternative interpretation of these data is possible if the assumptions of impulse delivery by a spherical blast wave (instantaneous deposition of energy at a point) and a finite target area are made.<sup>11,12</sup> This model predicts that the impulse is proportional to the square root of total energy. The impulse data shown in Fig. I-23 could be fit to within experimental error by a function of the square root of the energy. This interpretation then says the aerosol-induced breakdowns absorb only a small amount of energy and do not affect the measured impulse. It is clear that more data are necessary to really settle this point.

Section I



Fig. I-22. Open-shutter photograph of aerosol-induced breakdowns in laser beam which is focused on carbon target with 27-m focal-length mirror. Total energy in this shot was 514 J.

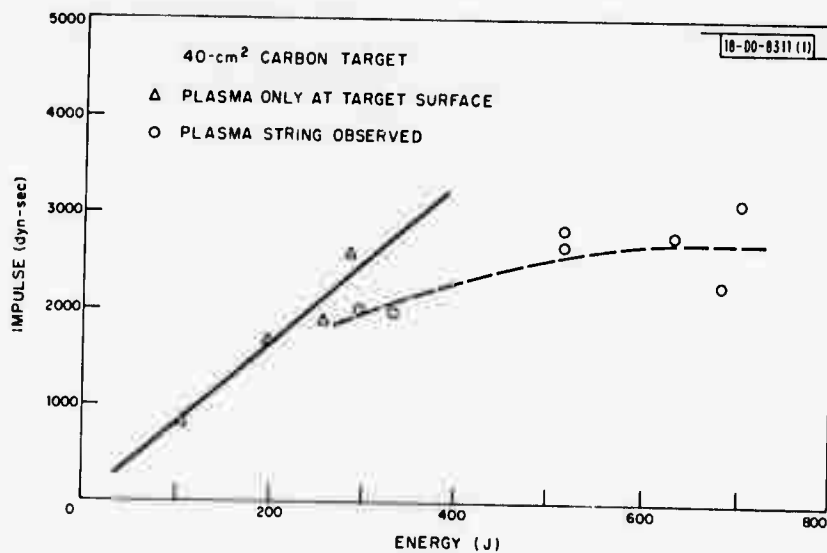


Fig. I-23. Plot of total impulse as a function of energy in laser pulse. Circles denote observation of aerosol-induced breakdowns in laser beam. Dashed line indicates trend of impulse saturation with increasing energy.

b. Plasma Properties Associated with Irradiation of a Surface by a Pulsed Laser

A number of experiments were performed with the Avco device to try to quantify some of the properties of the plasma produced in the laser-target interaction. The results of some earlier camera data (Ref. 11) indicated that a self-luminous front with velocities of  $2 \times 10^5$  to  $10^6$  cm/sec moved back in the direction of the laser beam. To supplement this information and provide two-dimensional data, the streak camera was replaced by a framing camera running at about  $2 \times 10^6$  frames/sec. In addition, the plasma was back-illuminated by a 40- $\mu$ sec-long pulse of 4881 radiation, so that essentially the second derivative of index of refraction (shadowgraph) rather than the self-lumination was viewed. The target was a carbon surface and the incident laser energy was approximately 200 J. Some typical results are shown in Figs. I-24 through I-26.

Figure I-24 shows the growth of the plasma on the target. The growth is approximately that of a spherical wave, with some asymmetry resulting because the impinging laser energy tended to arrive in two separate cones rather than in one. Figure I-25 shows similar data, except that in this case a fine copper wire was placed in front of the target, and breakdown initiated on the wire shows a distinctly spherical expansion with an expansion velocity of  $1.8 \times 10^5$  cm/sec. Finally, Fig. I-26 shows the resulting pattern in the late stages of expansion, after the laser pulse is completed and the initial shock wave has moved away. Notice the turbulent state of the medium. By using these types of data and neglecting the asymmetry due to the laser intensity distribution, the lateral and radial growth of a plasma ball was measured and is shown in Fig. I-27.

These data were used to help determine the absorptivity of the plasma. In an experimental arrangement similar to that described in Ref. 11 and illustrated in Fig. I-28, the transmission

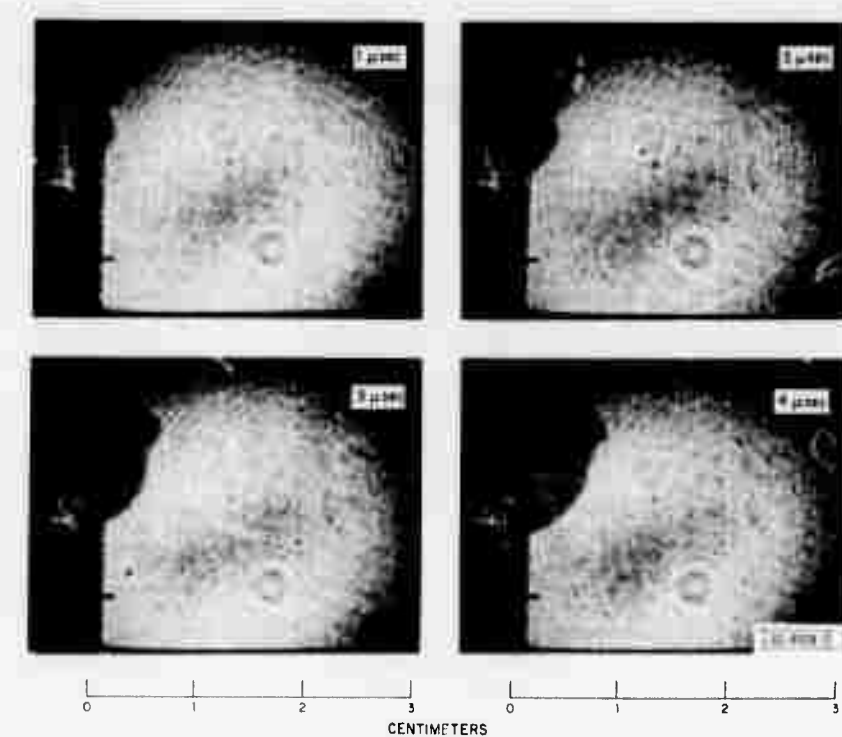


Fig. I-24. Back-illuminated framing camera data showing growth of a plasma on a target.

Section I

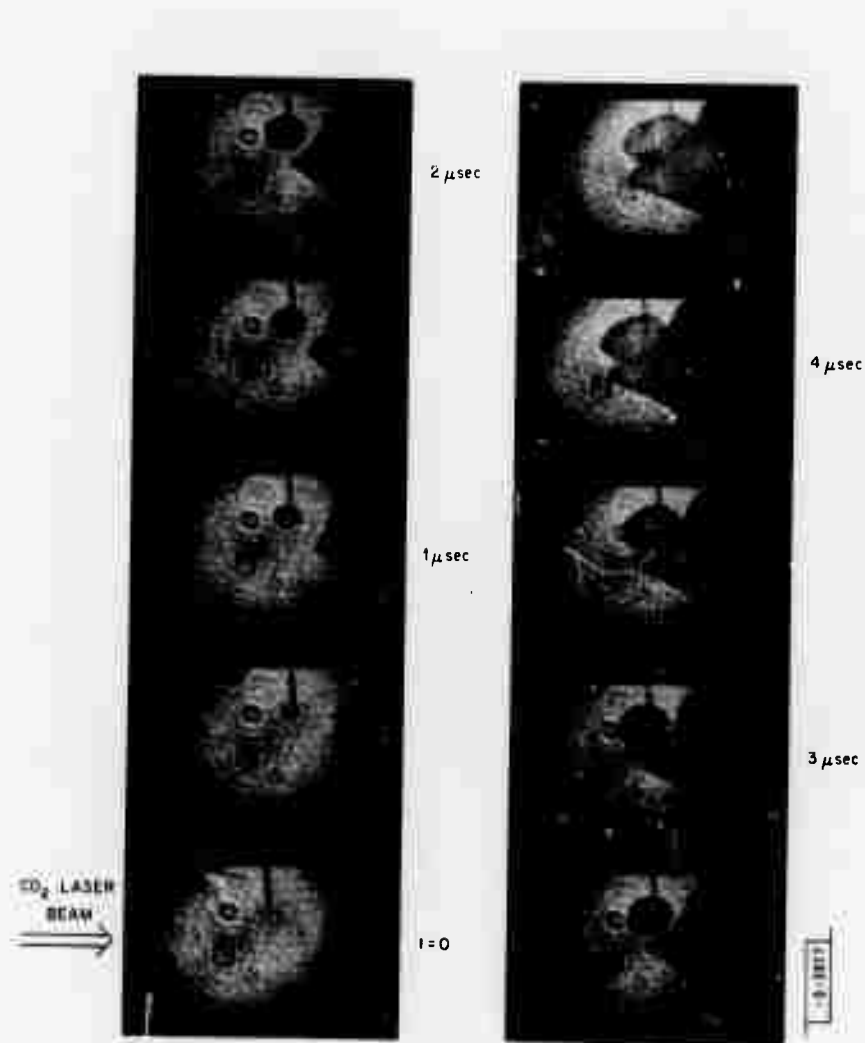


Fig. I-25. Back-illuminated framing data showing initiation and growth of a plasma on a fine copper wire. Interframe time is 0.5  $\mu$ sec.

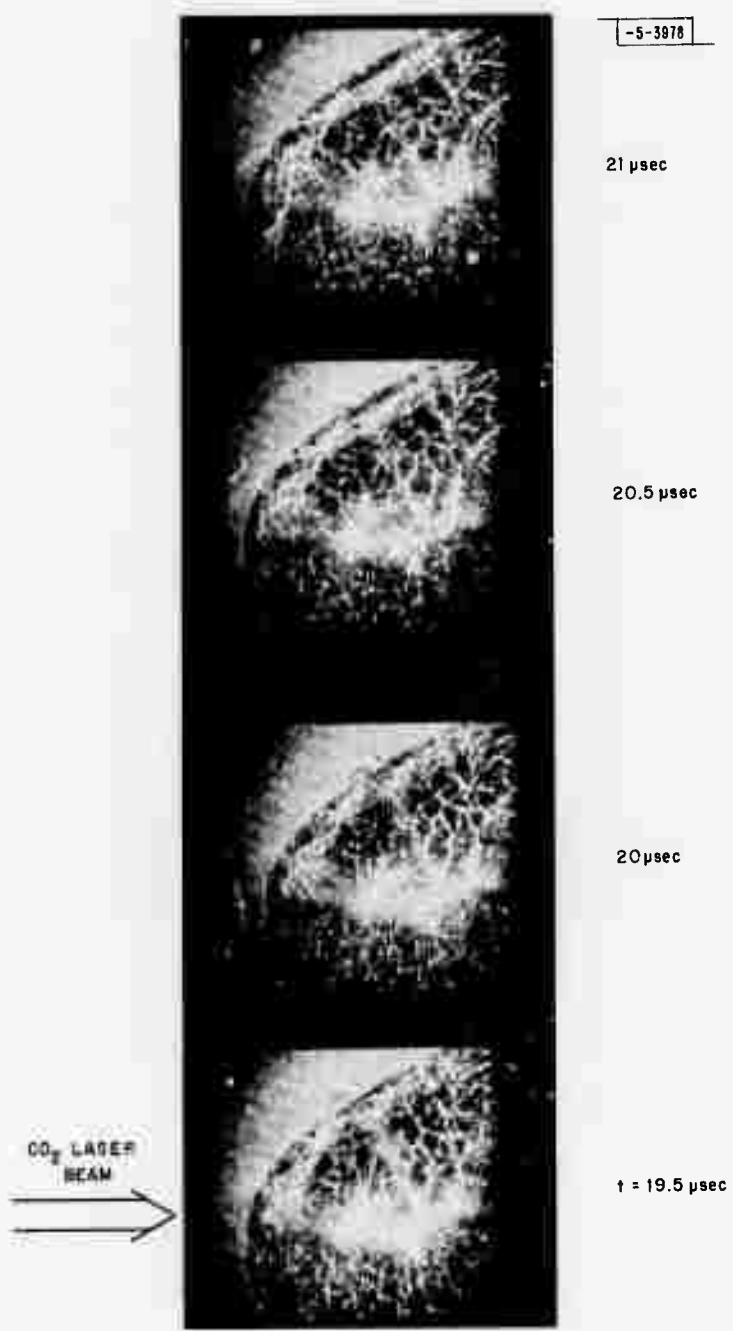


Fig. I-26. Late time development of a plasma initiated on a surface. Note turbulent nature of plasma medium. These data are typical ~30  $\mu$ sec after initiation of 10- $\mu$ m laser pulse.

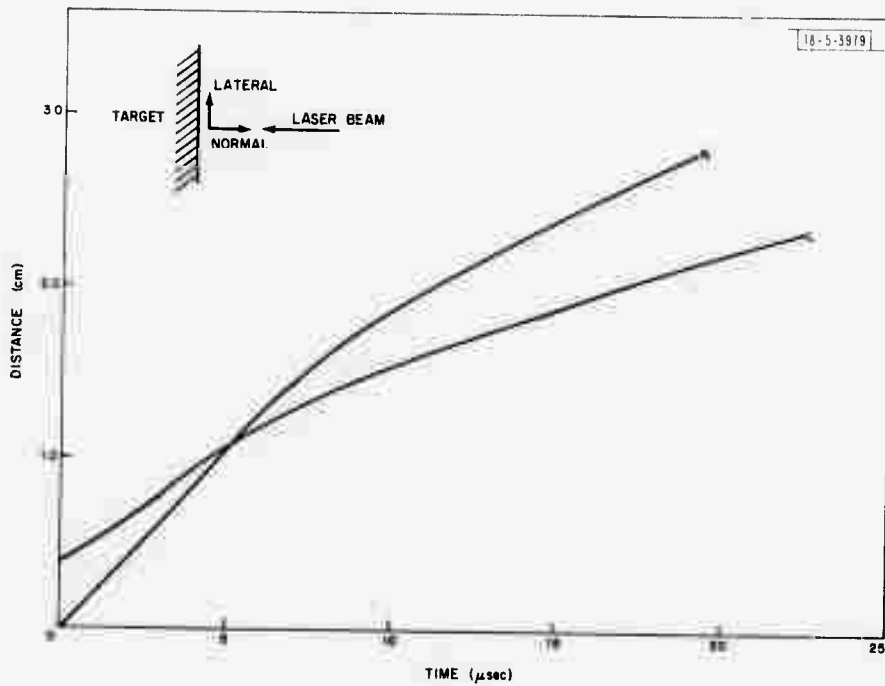


Fig. I-27. Lateral and forward growth of plasma on a carbon surface. Energy in pulse was about 200 J.

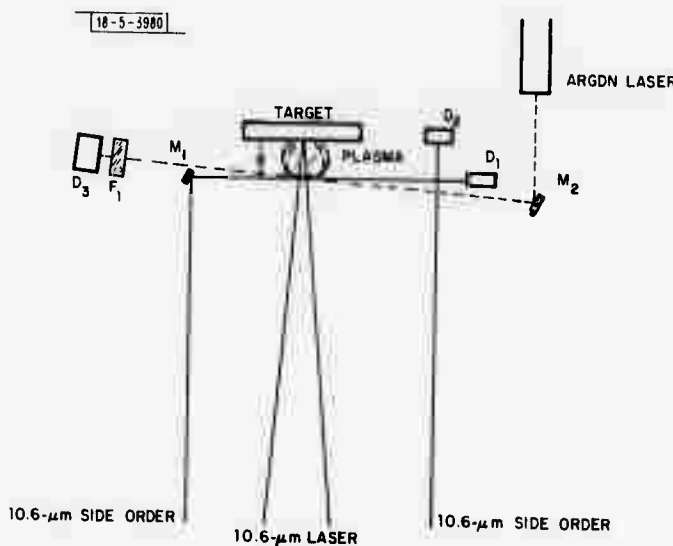


Fig. I-28. Experimental arrangement used to measure plasma opacity. An ion-argon laser ( $\lambda = 4881 \text{ \AA}$ ) and an order of 10-μm high-power laser are made to traverse same path through plasma medium a distance  $d$  in front of a target.  $M_1$  and  $M_2$  are bending mirrors,  $D_1$  and  $D_2$  are Ge photodiode detectors, and  $F_1$  is a chain of narrow-band 4881-Å filters.

history of  $10.6\text{-}\mu\text{m}$  and  $4881\text{-}\text{\AA}$  radiation through the plasma was monitored a distance  $d$  in front of the target.

The  $10.6\text{-}\mu\text{m}$  radiation used to probe the plasma was obtained by taking one of the grating side orders and transmitting it through the plasma and into a photon-drag detector  $D_1$ . At the same time, the unattenuated laser pulse was monitored with photon-drag detector  $D_2$ . A 1-W 40- $\mu\text{sec}$ -long pulsed argon-ion laser was triggered approximately  $10\ \mu\text{sec}$  before the  $\text{CO}_2$  laser pulse and passed through the same path as the deflected side order of the  $\text{CO}_2$  pulse. The argon laser pulse was passed through a series of  $4881\text{-}\text{\AA}$  narrowband filters into a Si photodiode  $D_3$ .

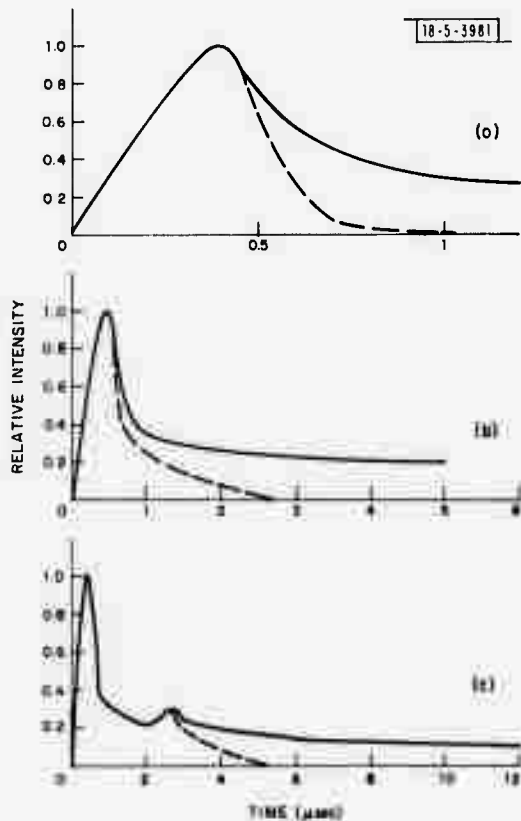


Fig. I-29. Normalized  $10\text{-}\mu\text{m}$  pulse shapes at different distance in front of a carbon target. Solid curves are unattenuated pulses, while dotted curves represent pulses after being transmitted through plasma medium. (a), (b), and (c) represent data taken at distances of 0, 3, and 10 mm in front of target, respectively.

Measurements were taken at three distances: 0, 3, and 10 mm in front of the target. For the  $10\text{-}\mu\text{m}$  data, the two pulses (attenuated and unattenuated) were normalized to peak unit intensity. The results are shown in Fig. I-29(a-c). Notice that the  $\text{CO}_2$  laser pulse has a rise time of 400 to 500 nsec. Absorption begins after a delay which is consistent with velocities in the range  $3 \times 10^5$  to  $10^6$  cm/sec. The framing camera data were used to determine the optical path length  $\delta(d, t)$  at a given distance  $d$  in front of the target and at a given time. The absorption coefficient

$$\alpha = -\frac{\ln I/I_0}{\delta}$$

was then calculated and is shown in Fig. I-30. The simplifying assumption of a uniform absorption across the plasma was used.

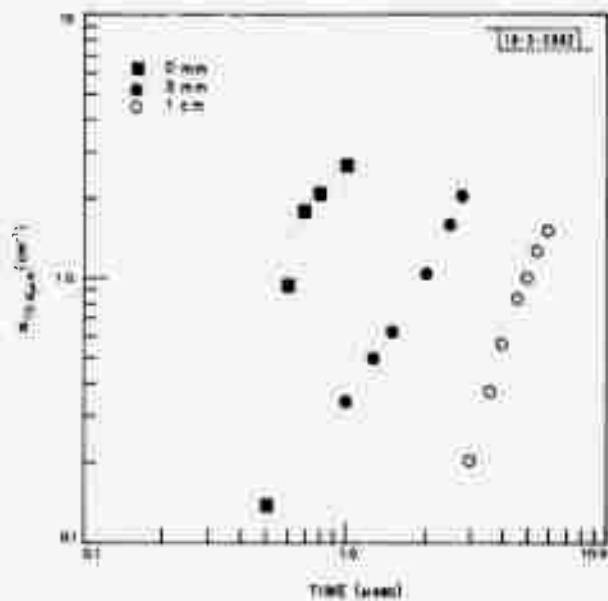


Fig. I-30. Time-dependent absorption coefficient at  $10.6 \mu\text{m}$  at three distances in front of target.

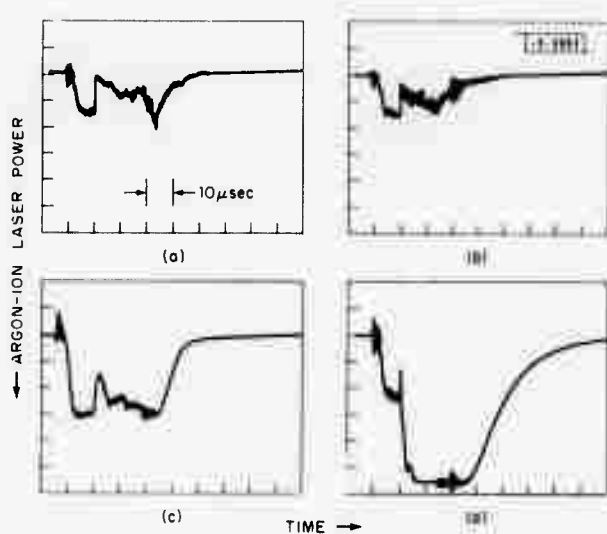


Fig. I-31. Argon-ion laser pulse transmitted through absorbing vapor in front of a carbon target. (a), (b), and (c) represent distances of 0, 3, and 10 mm in front of target, respectively. (d) is at 0 mm in front of target, but one 4881-Å filter was removed fram front of detector  $D_3$  (Fig. I-28) so that self-luminosity of plasma in wavelength regime was detected. Notice absorptian dip that occurs at  $t = 0$ , before self-luminosity of plasma is detectable.

Data from the 4881- $\text{\AA}$  laser are shown in Figs. I-31(a-d). The relative transmission at  $d = 0$ , 3, and 10 mm are shown in Figs. I-31(a-e), respectively. Figure I-31(d) is taken at 0 mm, but one of the narrowband filters in front of detector  $D_3$  was removed so that the plasma self-emission is shown. Notice that there is a narrow absorption spike ( $<1 \mu\text{sec}$ ) before the self-emission of the plasma builds up.

By analyzing these data in the same way as the 10- $\mu\text{m}$  data, the absorption coefficient at 4881  $\text{\AA}$  is shown in Fig. I-32.

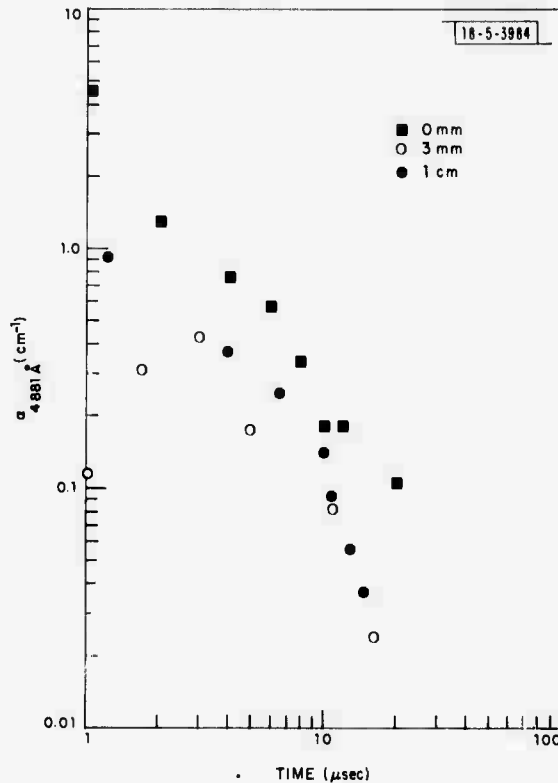


Fig. I-32. Time-dependent absorption coefficient data at 4881  $\text{\AA}$  at three distances in front of target. Because of jitter in firing of this laser, uncertainty in initial points of these curves is  $\sim 1 \mu\text{sec}$ .

If one makes the assumption that, for the 10- $\mu\text{m}$  radiation, the absorption is due to inverse bremsstrahlung, one can use the absorption coefficient to determine the electron density,<sup>15,16</sup> using the formula

$$\alpha(\text{cm}^{-1}) = 1.6 \times 10^{-37} \lambda^2 \eta_e^2 T_e^{-3/2} (1 - e^{-h\nu/kT_e}) \frac{kT_e}{h\nu} . \quad (\text{I-13})$$

Here,  $\alpha$  is the absorption coefficient in  $\text{cm}^{-1}$ ,  $\lambda$  is the wavelength in  $\mu\text{m}$ ,  $\eta_e$  is the electron density in  $\text{number}/\text{cm}^3$ ,  $T_e$  is the electron temperature in eV, and  $\nu$  is the laser frequency. The electron-density histories shown in Fig. I-33 were calculated with Eq. (I-13), the absorption coefficients given in Fig. I-30, and the assumption of a 1-eV plasma. Also shown in Fig. I-33 are electron densities obtained in the same manner from the 4881- $\text{\AA}$  absorption data. The assumption of a 1-eV plasma temperature is a reasonable estimate of the actual temperature; thus, the calculated electron densities are of the right order of magnitude and give correct relative values.

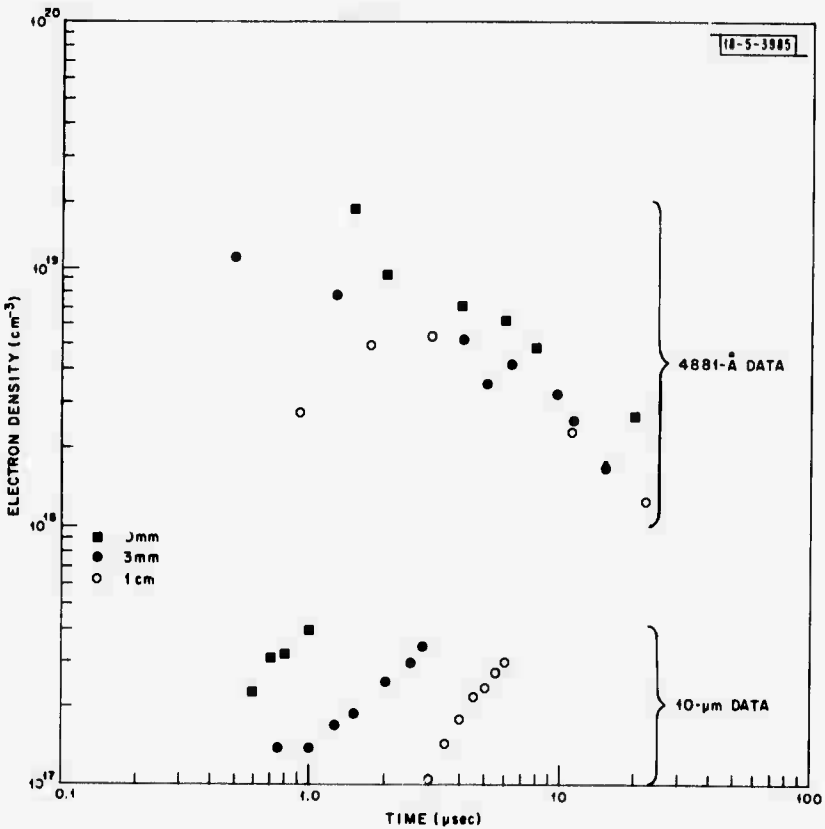


Fig. I-33. Electron densities calculated from data of Figs. I-30 and I-32 for 1-eV temperature and assumption that predominant absorption mechanism is inverse bremsstrahlung. This assumption is plausible for 10- $\mu\text{m}$  data and gives reasonable estimate for electron density time history in  $10^{17}$  to  $3 \times 10^{17}$   $\text{cm}^{-3}$ . The 4881- $\text{\AA}$  data suggest some photo-excited absorbing species as more probable candidates for vapor opacity.

These data indicate that the absorption at 4881 Å is not primarily due to free electrons. In fact, to within about  $\sim 1 \mu\text{sec}$ , the absorption at 4881 Å begins simultaneously at all three distances  $d$  in front of the target. Recall the absorption dip at the beginning of the 10-μm laser pulse in Fig. I-31(d) and notice that the absorption takes place before there is appreciable self-emission from the plasma, i.e., the plasma is still relatively cool with no appreciable electron density.

The simultaneous nature of the absorption onset suggests the production of a photo-excited species which absorbs strongly at 4881 Å and decays with a lifetime of about 10 μsec.

H. Kleiman  
R. W. O'Neil

### 3. Explosive Vaporization of Fog Droplets by a 10.6-μm Laser Pulse

Study continues of the explosive vaporization of fog droplets by a 10.6-μm laser pulse. The early stage (up to about 2 μsec) of the explosion process was described in previous Optics Research Reports.\* We studied the later stage of the process by observing the vapor "blob" produced by the evaporation of single droplets. These observations were made with a high-speed schlieren photography system that was described in the last Optics Research Report [(1971:2), DDC AD-901213]; early results on the vaporization of oversize droplets were also presented in that report.

In a ground fog or a cloud, the water droplets usually range in size from  $<1$ - to  $\sim 25$ -μm radius. In the present study, droplets ranging from 5- to 25-μm radius have been irradiated. In addition, some oversize droplets (25- to 70-μm radius) have been studied because their behavior does help in understanding the processes involved. The laser energy at the position of the water droplet was varied between 5 and 15 J/cm<sup>2</sup> in these experiments. The peak power density was typically 10 to 30 MW/cm<sup>2</sup>.

Electrical breakdown did not occur under these conditions. This was determined by means of time-exposed photomicrographs of the exploding droplet; these photos were taken without any back-illumination. No light was emitted during the explosive vaporization of a water droplet. If, however, instead of a water droplet, a 25-μm-radius glass fiber is placed at the same position and irradiated with an identical pulse, electrical breakdown does occur and a brilliant flash of light is produced.

#### a. Results and Discussion

The schlieren pictures show an expanding sphere of vapor surrounded by a rapidly expanding shock wave. Actually, the observed "vapor sphere" is a sphere of air that has been heated by the vapor. The sphere of heated air has an index of refraction different from that of the ambient medium, and this difference is sensed by the schlieren system.

Figure I-34 shows schlieren photographs of four exploding droplets at times from 0.7 to 37 μsec after the 10.6-μm laser pulse. The radius of each water droplet is indicated in the picture. At 0.7-μsec, the vapor sphere cannot be distinguished within the shock wave, but the second photograph (4.9 μsec) clearly shows the vapor sphere at the center of the shock-wave

\* Optics Research Reports, Lincoln Laboratory, M.I.T. (1970:3), DDC AD-882617, and (1971:1), DDC AD-888823-L.

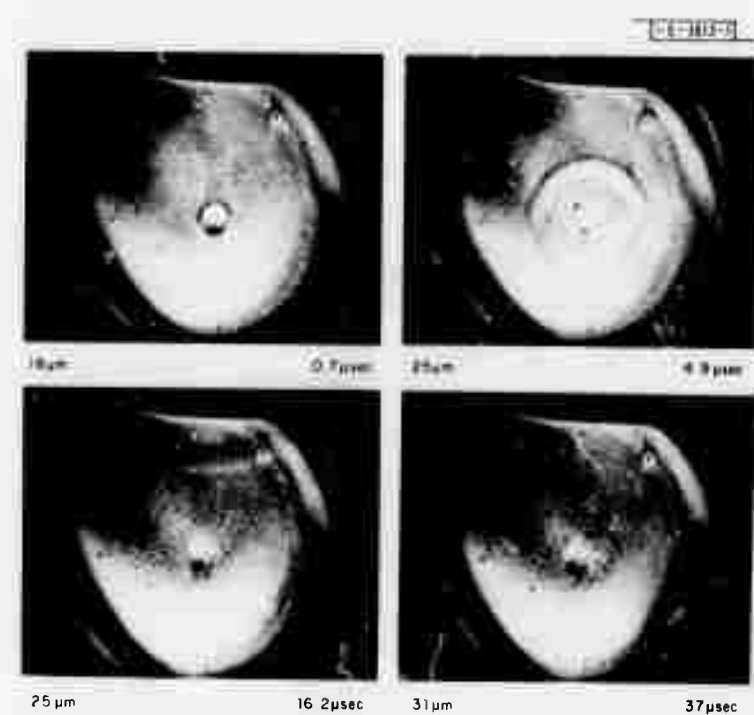
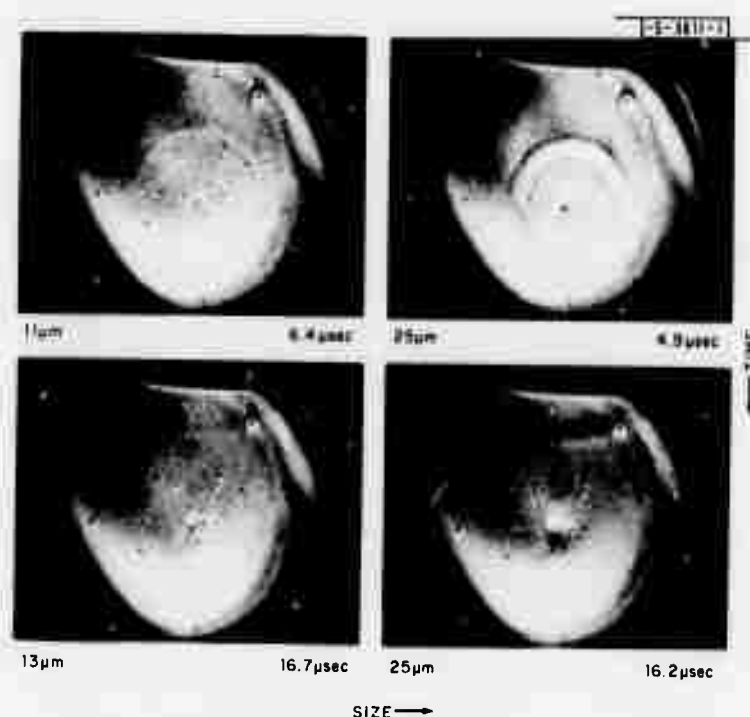


Fig. I-34. Schlieren photographs of four exploding water droplets. Radius of each droplet is shown at left, and elapsed time since 10.6- $\mu$ m laser pulse is shown at right. Laser pulse direction: left to right.

sphere. In the third picture (16.2  $\mu$ sec), the shock wave can be seen at the top, after it has reflected from the horizontal surface (which happens to be the bottom of the droplet generator). Finally (at 37  $\mu$ sec), the shock wave is beyond the FOV of the system. This sequence of pictures also shows the expanding volume of the vapor sphere. In these photographs, the direction of the 10.6- $\mu$ m laser pulse is from left to right; the schlieren knife-edge is oriented horizontally. (The pictures also show some extraneous features that are common to all the photographs; these are due to aberrations in the optical system and to imperfections in the lenses. They can be readily distinguished and disregarded.)

In the study of the early stage of the water-droplet explosion, we showed that the liquid-vapor mixture was expanding at a radial velocity of 0.13 mm/ $\mu$ sec in the time interval 0 to 2.3  $\mu$ sec. Our schlieren photographs show that the vapor sphere expands with a radial velocity of 0.015 mm/ $\mu$ sec in the time interval 5 to 16  $\mu$ sec, and the velocity has decreased to a value of 0.010 mm/ $\mu$ sec in the interval 16 to 37  $\mu$ sec. Even in this interval, the radial expansion rate is  $\sim$ 300 times greater than the diffusion velocity, indicating that the expansion process is still dominated by the momentum of the initial explosion.

In Fig. I-35, the photographs show the effect of droplet size on the magnitude of the observable effects. The small droplets (11- and 13- $\mu$ m radius) at the left produced a faint but clearly observable shock wave with a faintly distinguishable vapor sphere at the center. The pictures at the right show the much stronger effects produced by the explosive vaporization of 25- $\mu$ m-radius droplets, where the mass of water is  $\sim$ 8 times as great. In each of these shots, the energy density of the laser pulse was about 10 J/cm<sup>2</sup>, and the pulse shape was about the same.



**Fig. I-35.** Schlieren photographs of four exploding water droplets, showing effect of droplet size. Laser pulse direction: left to right.

Under certain conditions, the hot vapor assumed a nonspherical shape – usually when the water droplet was very large ( $\gtrsim 35\text{-}\mu\text{m}$  radius) or when the energy density was very low ( $\sim 5\text{ J/cm}^2$ ). In these cases, the vapor volume was shaped like a dumbbell with its axis oriented approximately along the direction of the laser pulse. Figure I-36 shows a typical example, an  $\sim 35\text{-}\mu\text{m}$ -radius droplet at 6.7  $\mu\text{sec}$  after the laser pulse. The left sphere of the dumbbell is at the center of the shock wave, and this is the site of the original explosion. If the absorbed energy is not sufficient to cause immediate (within  $\sim 2\text{ }\mu\text{sec}$ ) vaporization of the droplet, and if the droplet is large enough to undergo surface heating rather than volume heating, then the remainder of the evaporating



**Fig. I-36.** Schlieren photograph of large ( $\gtrsim 35\text{-}\mu\text{m}$  radius) exploding water droplet 6.7  $\mu\text{sec}$  after 10.6- $\mu\text{m}$  laser pulse. Laser pulse direction: left to right.

droplet is propelled by the rocket action of its vaporizing surface. The motion is always opposite to the direction that the blow-off vapor is moving, as required to conserve momentum.

A picture similar to Fig. I-36 was obtained with a 26- $\mu\text{m}$ -radius droplet irradiated with a laser pulse of  $4\text{ J/cm}^2$ . But when another droplet of the same size was irradiated with a  $9\text{-J/cm}^2$  pulse, the usual spherical vapor volume resulted. This behavior can be explained by the curves in Fig. I-37, which show the energy absorbed by a water droplet for pulses of various energy densities. Actually, this is the energy that would be absorbed by a water droplet that remained intact during the laser pulse. These curves were drawn using the absorption cross sections in the tables of Zel'manovich and Shifrin.<sup>17</sup> In the case of the  $9\text{-J/cm}^2$  pulse, the energy that

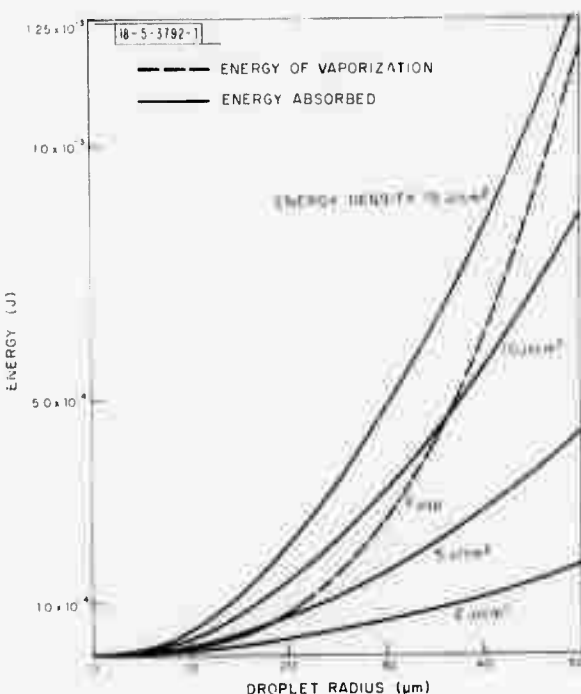


Fig. I-37. Energy absorbed by water droplet for incident  $10.6\text{-}\mu\text{m}$  laser pulses of indicated energy density. Energy of vaporization,  $E_{\text{vap}}$ , is also shown for comparison.

could be absorbed by the water droplet is substantially greater than the energy required for vaporization. In the case of the  $4\text{-J/cm}^2$  pulse, the energy absorbed by the droplet is much less than the energy of vaporization. Our early studies using the tri-scopic camera system showed that the droplets of radius  $\gtrsim 15\text{ }\mu\text{m}$  undergo surface heating. Such droplets when partially vaporized can be propelled along the general direction of the laser pulse; this is the case for the droplet in Fig. I-36, which could absorb barely enough energy for vaporization. In general, the asymmetric heating (surface heating) of optically thick droplets will result in an asymmetric vapor volume unless the absorbed energy is much greater than that required for vaporizing the droplet. The asymmetric volume will be shaped like a dumbbell or like an incipient dumbbell, with the second sphere undeveloped or partially developed.

## b. Energy of the Explosion

Figure I-38 shows the radius of the shock wave as a function of time for many different shots, covering three ranges of droplet size. Although the points fall close to the line of slope corresponding to a shock-wave velocity of Mach 1 (in air), it will be noted that the zero-time intercept is 0.5 mm, which is 20 times greater than the initial droplet radius. In the first couple of microseconds, the shock-wave velocity is much greater than Mach 1.

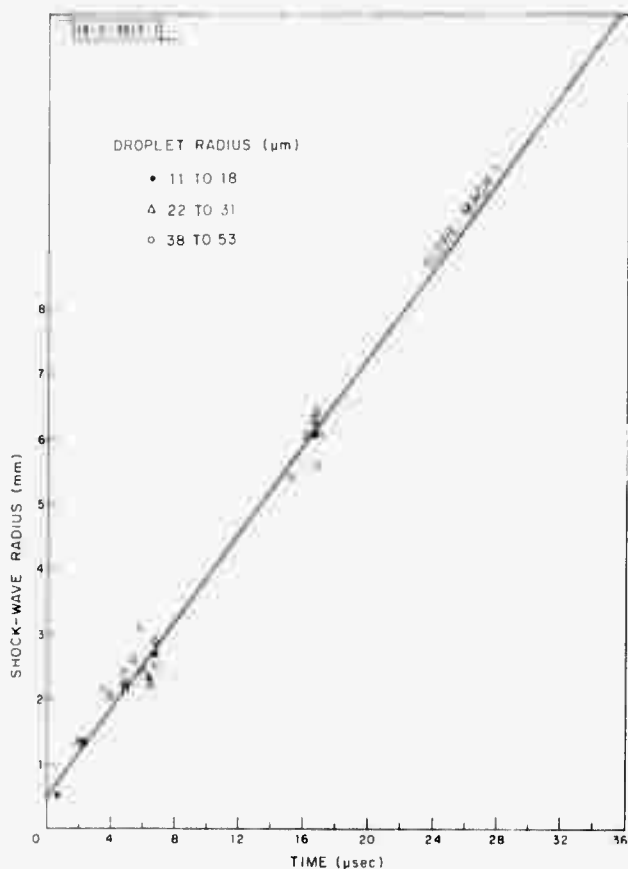


Fig. I-38. Radius of shock wave as function of time.

The radius of the shock wave at a given time can be used to calculate the explosive energy, as discussed in the last Optics Research Report [(1971:2), IDOC AD-901213]. We have calculated the explosive yield for 5 shots involving water droplets of 25-μm radius. The yield may be compared with the difference between the absorbed energy, as determined from Fig. I-37, and the energy needed to evaporate the droplets. The agreement is within about 25 percent. This energy balance cannot be used for large ( $\geq 40$ -μm-radius) droplets because they do not evaporate completely.

P. Kafatas  
J. Herrmann

Section I

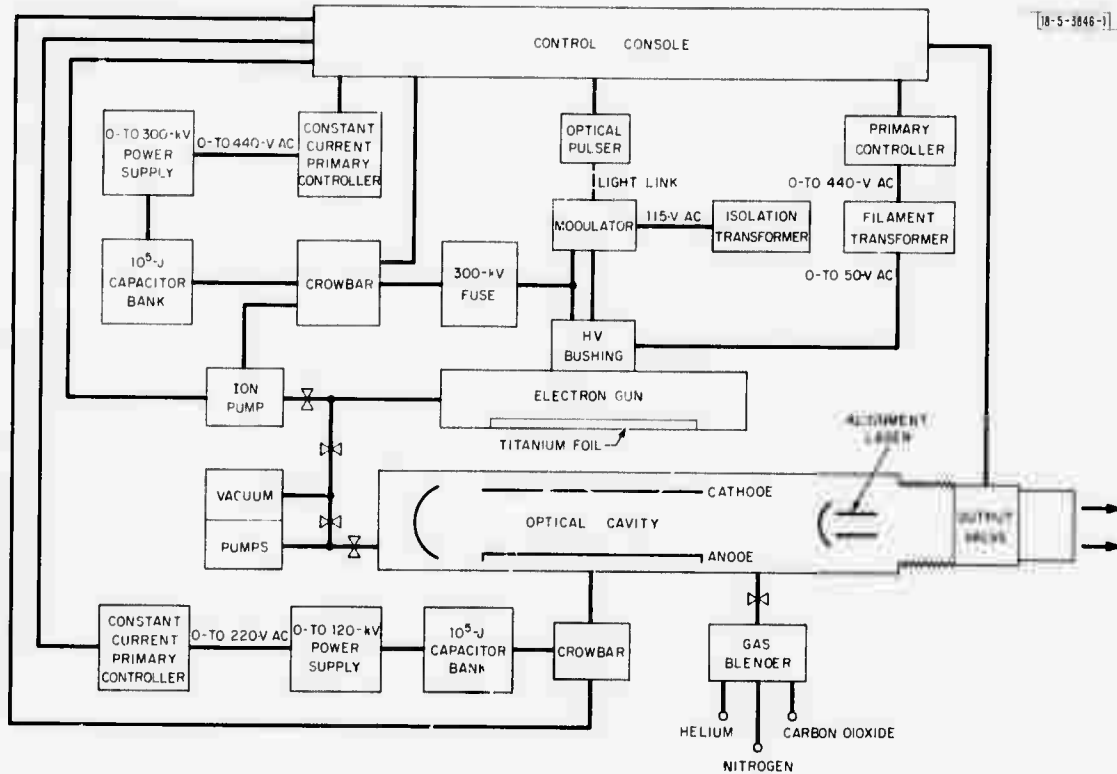


Fig. I-39. Schematic diagram of 500-J EDL.

## C. DEVICES

### 1. Electron Beam (e-Beam)

#### a. 500-J, e-Beam Excited Laser

Figure I-39 is a schematic diagram of the 500-J EDL now under construction.\* All major components are on hand and assembly is nearly complete. In keeping with its planned use as a source of high-energy  $10.6\text{-}\mu\text{m}$  pulses of good optical quality, the operating sequence has been automated as much as possible to keep the output reproducible and reliable.

The electron gun is a triode and can be grid controlled from cutoff to current densities in excess of  $100\text{ mA/cm}^2$  through a  $15 \times 104\text{ cm}$ , 1-mil titanium foil window. It is capable of pulses of from 1- to  $100\text{-}\mu\text{sec}$  duration with rise times of  $0.1\text{ }\mu\text{sec}$ .

The optical cavity has an effective length of  $2.5\text{ m}$  with a maximum cross section of  $15 \times 20\text{ cm}$ . The active volume is 22.5 liters.

To avoid the need for large, high-power windows, a fast shutter valve is opened to pass the outcoupled optical beam.

The optical cavity will be evacuated after each shot and then refilled with the laser gas mixture. A gas blower will allow the mixture to be easily optimized for the pulse length and power chosen by an experimenter.

First operation in a laser is expected early in August, followed by about 60 days of tests and diagnostics. We anticipate that the device should be operational in October.

A. J. Morency  
R. J. Carbone

#### b. e-Beam $\text{CO}_2$ Laser Kinetics

The  $\text{CO}_2\text{-N}_2\text{-He}$  rate equations of Douglas-Hamilton<sup>18</sup> were programmed using the Runge-Kutta method. In Douglas-Hamilton's approach, the  $\nu_1$ ,  $\nu_2$ , and  $\nu_3$  modes of  $\text{CO}_2$  and the vibrational levels of  $\text{N}_2$  are assumed to equilibrate internally so rapidly that each of these modes can be described by a vibrational temperature. The four equations describing these temperatures, plus a fifth equation describing the gas temperature, compose the coupled set of differential equations. With the electron excitation coefficients calculated by Nighan<sup>19</sup> and the relaxation rates reported by Taylor and Bitterman,<sup>20</sup> the computed gains, pulse lengths, and pulse energies were in reasonable agreement with the experimental results on the Avco e-beam laser.

In this analysis, the laser flux is determined by the constraint that, during the pulse, the laser gain is equal to the cavity losses. Accordingly, these equations do not correctly describe the initial portion of the pulse where the gain still greatly exceeds the losses, and the equations do not predict the experimentally observed initial spike. To remedy this, a sixth equation describing the growth of the stimulated emission was included. This indeed provided the initial spike, but its computed 50-nsec width is considerably smaller than the observed 300 to 500 nsec. This discrepancy may be due to the fact that on the time scale of the initial spike, the assumption of vibrational temperatures may be invalid. We are presently investigating this possibility.

S. Marcus  
D. Zanni

\* See Optics Research Report (1971:2), p. 23, DDC AD-901213.

Section I

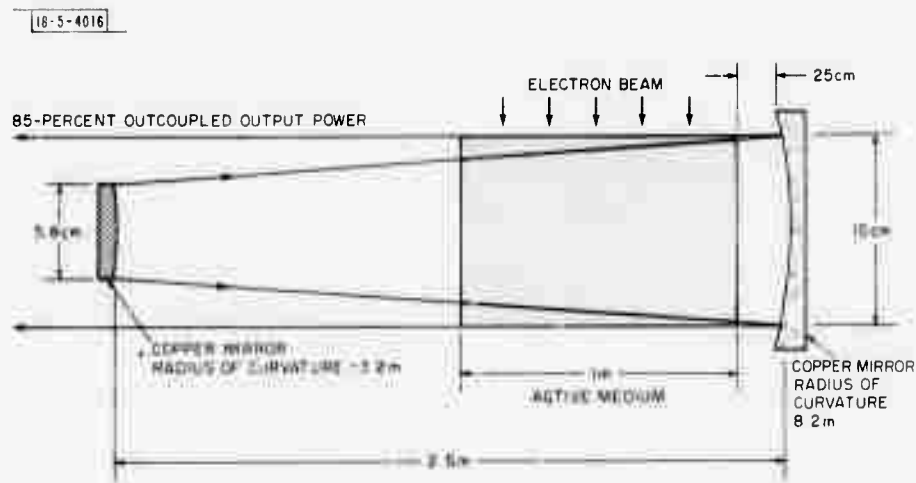


Fig. I-40. Geometry of 500-J pulse unstable confocal resonator cavity for optimum mode quality-energy product (outcoupling  $\delta = 0.85$ ).

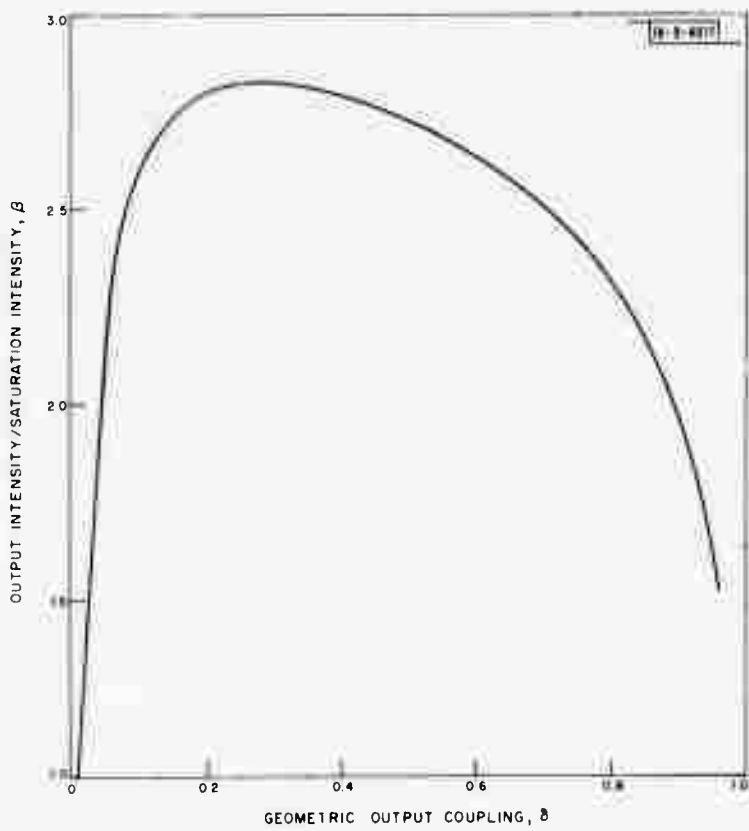


Fig. I-41. Output intensity normalized to saturation intensity as function of geometric outcoupling ( $\delta = 1 - (1/m^2)$ ) for uniform mode filling, with mirror reflectance  $R^2 = 0.99$ , cavity length 2.5 m, active length 1.0 m, and small signal gain  $0.032 \text{ cm}^{-1}$ .

### c. Cavity Design of a Pulsed 500-J CO<sub>2</sub> Laser

As its first priority, the EDL effort has a pulsed CO<sub>2</sub> laser device that is designed to out-couple 500J of 10.6-μm radiation.\* The volume of the laser medium will be 22.5 liters contained within a length of 1 m. A 2.5-m unstable, confocal, positive branch resonator (shown in Fig. I-40) was chosen to effectively utilize this large volume/short-length gain medium.

The cavity design was chosen so that optical energy will not focus within the device, and the forward and backward energy flow will very nearly fill the gain medium. The optimized resonator parameters were chosen as a tradeoff between total power output reduction while maintaining a single mode as the output coupling was increased. Figure I-41 illustrates the effect of power output vs coupling at a gain of 0.032 cm<sup>-1</sup> and 99-percent reflecting mirrors. The Rigrod<sup>21</sup> approach was used to determine the power extraction as a function of predicted gain and optimal energy storage. A reasonable tradeoff between mode quality and optimum energy output is at an output calculated to be 60 percent. Using a geometrical approach, this outcoupling will utilize at least 52 percent of the active volume for an inscribed (within a 15 × 15 cm square) circular mode, 65 percent for a 15 × 15 cm square mode, and 87 percent for a fitted rectangular mode of 15 × 20 cm. Several cavity outcouplings will be tested to experimentally verify the power output predictions, and to compare the experimental results with mode calculations that have been reported<sup>22-25</sup> and with calculations presently being done at Lincoln Laboratory.

~~The criterion used to judge beam quality outcoupled from the laser is the energy deposited in the Airy disks compared with 81 percent of the energy deposited in the first Airy disk for a uniformly illuminated aperture. For the 60-percent coupling case, 83 percent of the output energy will be deposited within the first three Airy disks, or 3X diffraction-limited by this criterion.~~

Optimization of mode quality is achieved by maximizing the product of the energy output and the energy fraction in the first Airy disk, as shown in Fig. I-42. This optimum outcoupling is at 85 percent, which corresponds to a reduction of about 15 percent in energy extracted per unit volume (relative to 60-percent outcoupling), approximately 82-percent volume filling factor, and about 45 percent of the net energy within the first Airy disk.

The absolute power outcoupled for the cavity design has been calculated from the rate equations and energy balance within the laser medium. The approach used followed that of Douglas-Hamilton.<sup>18</sup> Predictions of medium heating, pulse length, and gain are reliable, but calculated optical energy storage/cross-sectional area at 7.4 J/cm<sup>2</sup> with 2 mA/cm<sup>2</sup> e-beam pumping may be too high. This indicates an extraction of 74 J/liter for a 1 m device. Table I-1 gives typical computed values of pulse length, gain, and output energy for different e-beam current intensities.

R. J. Carbone  
H. Granek

### d. Mode Calculations for the Unstable Resonator

The Fredholm integral equation for the asymmetric unstable resonator cavity is used for the mode field distributions without a gain medium in the mirror planes. The field distributions are given by<sup>22</sup>

\* Optics Research Report (1971;2), p. 23, DDC AD-901214.

Section I

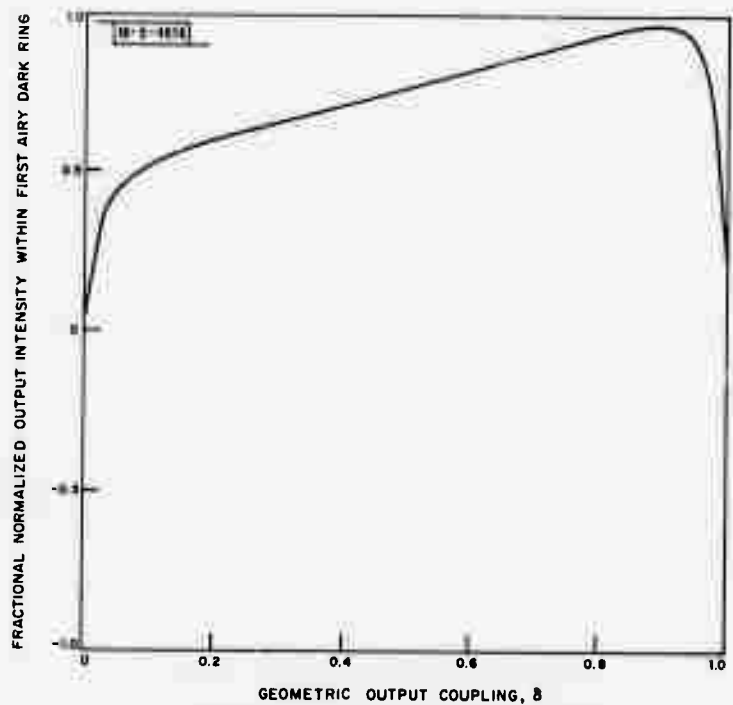


Fig. I-42. Amount of output intensity (normalized to saturation intensity) concentrated within first Airy dark ring of far-field pattern (incident plane wave approximation onto outcoupling annulus) for conditions given in Fig. I-41.

TABLE I-1 TYPICAL COMPUTED LASER PARAMETERS FOR GIVEN e-BEAM CURRENT INTENSITIES			
Current Density (mA/cm <sup>2</sup> )	Peak Zero-Flux Gain (cm <sup>-1</sup> )	Pulse Length (μsec)	Energy Out (J/cm <sup>2</sup> )
2	0.0282	43.8	7.4
10	0.0326	25.7	10.0
20	0.0339	20.1	11.1
30	0.0345	17.4	11.8

Section I

$$\gamma_1 \varphi_1(x) = j^{\ell+1} (k/L) \int_0^{a_1} y J_\ell(kxy/L) \exp[-j(k/2L)(g_1 x^2 + g_2 y^2)] \varphi_2(y) dy \quad (I-14)$$

$$\gamma_2 \varphi_2(y) = j^{\ell+1} (k/L) \int_0^{a_1} z J_\ell(kyz/L) \exp[-j(k/2L)(g_2 y^2 + g_1 z^2)] \varphi_1(z) dz \quad . \quad (I-15)$$

In this expression,  $g_i = 1 - (L/R_i)$ , where  $R_i$  is the radius of curvature,  $L$  is the mirror separation,  $\gamma$ 's are eigenvalues to be determined, and  $2a_i$  is the mirror diameter.

One can substitute Eq. (I-15) into Eq. (I-14) to determine an eigenvalue equation for the field at the output mirror. Use of Bessel function identities<sup>26</sup> permits elimination of the integral of the product Bessel functions and reduction to a form

$$\begin{aligned} \gamma_1 \gamma_2 \varphi_1(x) &= \left( j^{\ell+1} \frac{k}{2Lg_2} \right) \int_0^{a_1} \exp \left[ \left( -\frac{jk}{2L} (2g_1 g_2 - 1) \left( \frac{x^2 + y^2}{2g_2} \right) \right) \right] \\ &\quad \times J_\ell \left( \frac{k}{2g_2 L} xz \right) z \varphi_1(z) dz \quad . \end{aligned} \quad (I-16)$$

Manipulation of this expression and expansion of the unknown functions in the form<sup>23</sup>

$$\varphi(x) \exp \left[ -j \frac{c_1}{4g_2} (2g_1 g_2 - 1) x^2 \right] = \sum_{m=0}^{\infty} a_m L_m^{(\ell)}(x^2) \quad (I-17)$$

where  $C_1 = 2\pi a_1^2 / L$  allows simplification to an infinite matrix of the form<sup>27</sup>

$$\begin{aligned} (\gamma_1 \gamma_2) \frac{(\ell+t)!}{t!} a_t &= j^{\ell+1} \frac{C_1/4g_2}{t!} \int_0^{C_1/4g_2} \exp \left\{ -U' [2j(2g_1 g_2 - 1) + 1] \right\} (U')^{\ell+t} \\ &\quad \times \sum_{m=0}^{\infty} a_m L_m^{(\ell)}(U') \quad . \end{aligned} \quad (I-18)$$

Calculations of a truncated form of this matrix for the empty cavity modes of the unstable resonator are under way. Comparison of these results with propagation calculations and experimental data is anticipated.

H. Granek

e. Longitudinal e-Beam Excited Laser

The 3-nsec, 600-keV, e-beam source described in the previous Optics Research Report was used to ionize a CO<sub>2</sub>-N<sub>2</sub>-He medium from which laser pulses lasting up to 120 μsec were obtained. In the configuration being used, the e-beam is nearly colinear with the laser axis and normal to the sustainer electric field. An article describing the operation of this laser has been published.<sup>28</sup> In the meantime, the maximum output energy was increased to 22.4 J over the 11.5 J reported in that paper. This was accomplished by improving the design of the electrodes and by increasing the active laser volume. We are presently redesigning the laser cavity to permit passive Q-switching.

S. Marcus

## Section I

### f. Pulse Shaping a CO<sub>2</sub> Laser Beam

For a number of applications it is desirable to be able to shape in time high-energy laser pulses of 10.6-μm radiation. One approach is to try to build pulse-shaping capabilities into the laser itself, for instance, by modulating the grid of an e-beam pumped laser. However, for other classes of pulsed machines it is more practical to try to develop external pulse-shaping capability. Here, we report some successful preliminary attempts to generate simple waveforms using saturable absorbers external to the laser cavity. A similar technique has recently been reported for use in the visible range.<sup>29</sup>

The basic idea can be understood by considering the expression for absorption in a two-level system:

$$\alpha = \alpha_0 \left[ \frac{1 + \frac{I}{I_s} \exp\{-[1 + (I/I_s)]^{t/\tau}\}}{1 + \frac{1}{I_s}} \right].$$

Here,  $\alpha_0$  is the unsaturated absorption coefficient,  $I_s = h\nu/2\sigma\tau$  is the saturation intensity,  $\sigma$  is the cross section for molecular absorption,  $\nu$  is the laser frequency, and  $\tau$  is the relaxation time of the upper level. In all useful absorbers, the initial and final levels interact strongly with closely lying rotational and vibrational levels and, consequently, the two-level picture is not a valid one. However, it can be shown that, when the relaxation time among these levels is short compared with  $\tau$  and the laser pulse length, the above relation still holds except that  $I_s = h\nu/2\sigma\tau\delta$ , where the factor  $1/\delta$  is the effective number of interacting levels.

This gives the medium saturation time constant

$$\tau_s = \frac{\tau}{1 + \frac{1}{I_s}}.$$

Suppose we require the pulse length  $\tau_p \cong \tau_s$ . This would allow the medium to saturate gradually and generate a ramp function, which would require an intensity

$$I = I_s \left( \frac{\tau}{\tau_p} - 1 \right) = \frac{h\nu}{2\sigma\tau\delta} \left( \frac{\tau}{\tau_p} - 1 \right).$$

If the peak of the ramp is to be substantially unattenuated, then we must have  $I \gg I_s$  or, equivalently,  $\tau \gg \tau_p$ . In this case, a square pulse of intensity

$$I = I_s \frac{\tau}{\tau_p} = \frac{h\nu}{2\sigma\tau_p\delta}$$

should generate a ramp function. Figure 1-43 shows the experimental arrangement in which we used a CO<sub>2</sub> laser which generated a pulse with uniform power output of  $\approx 4 \times 10^5$  W for 30 μsec (see Ref. 28). This pulse was focused through a 20-cm absorption cell with Brewster angle windows. A KCl flat diverted about 5 percent of the energy to a BaTiO<sub>3</sub> calorimeter so that the pulse energy could be monitored. The pulse at the cell exit was monitored with a photon-drag Ge detector. The beam was approximately 1 cm<sup>2</sup> in area at the entrance and exit of the cell, and perhaps 1/4 that area at the center of the cell.

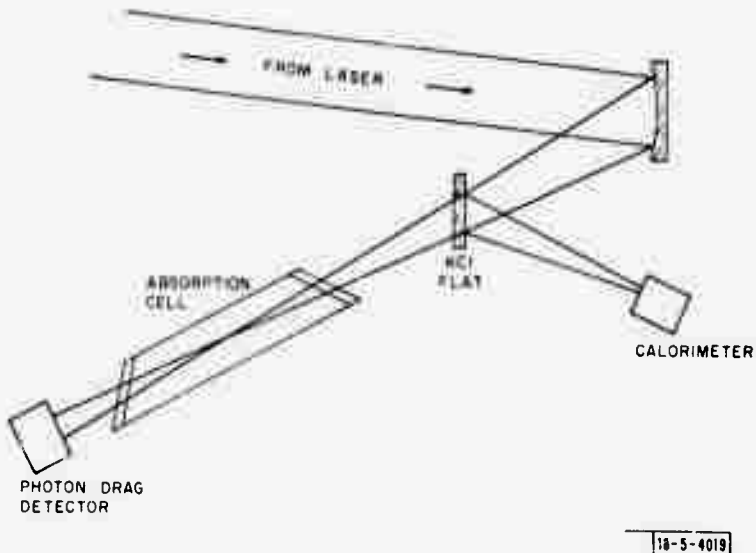


Fig. I-43. Experimental arrangement for observing pulse shaping.

Figure I-44(a-d) shows a series of waveforms generated at different pressures of SF<sub>6</sub>. In the region where  $\sigma$  is a function of pressure, the pressure and intensity can be adjusted to maintain the product  $I\sigma$  constant. This allows generation of the same waveform at varying intensity levels.

Figure I-45(a-d) shows the results of using Freon 12 as an absorbing gas. The relaxation time here is short compared with the pulse length, so that the intense leading edge of the pulse goes through unattenuated while the rear of the pulse is absorbed. This is the more familiar case of pulse shaping.

We have demonstrated the ability to produce slow or fast opening attenuators for uniform laser pulses, and to use these attenuators to produce ramp and spikes of desired temporal characteristics.

H. Kleiman  
S. Marcus

#### g. Feasibility Study for Amplification of Short Pulses and Frequency-Modulated Pulses

Here, we report the results of a feasibility study on the design of a very broad-band, high-power laser amplification system. There is current research interest in an amplifier at 10.6  $\mu\text{m}$  that could handle either a repeated burst sequence of nanosecond pulses or a repeated sequence of pulses less than a microsecond in length with FM up to 1.5 GHz. Energy outputs in excess of 3 J per pulse and average power of 20 kW are required, with total coherence time of the pulse sequence extending from circa 30  $\mu\text{sec}$  to 5 msec. To handle the information bandwidth of the pulses, the amplifier would have to operate at pressures of at least 150 to 200 torr for 500-MHz signals, and approaching an atmosphere of pressure for full bandwidth capacity.<sup>30-32</sup> There are four devices in the "high"-pressure regime that could possibly satisfy the requirements of minimum optical distortion ( $<\lambda/40$ ): longitudinal discharge, cross-flow laser<sup>33</sup>; waveguide laser<sup>34</sup>; preionized devices; and independently ionized devices. The first type has been limited to pressures below 100 torr, thus does not exhibit sufficient bandwidth to be applicable. The second is

Section I

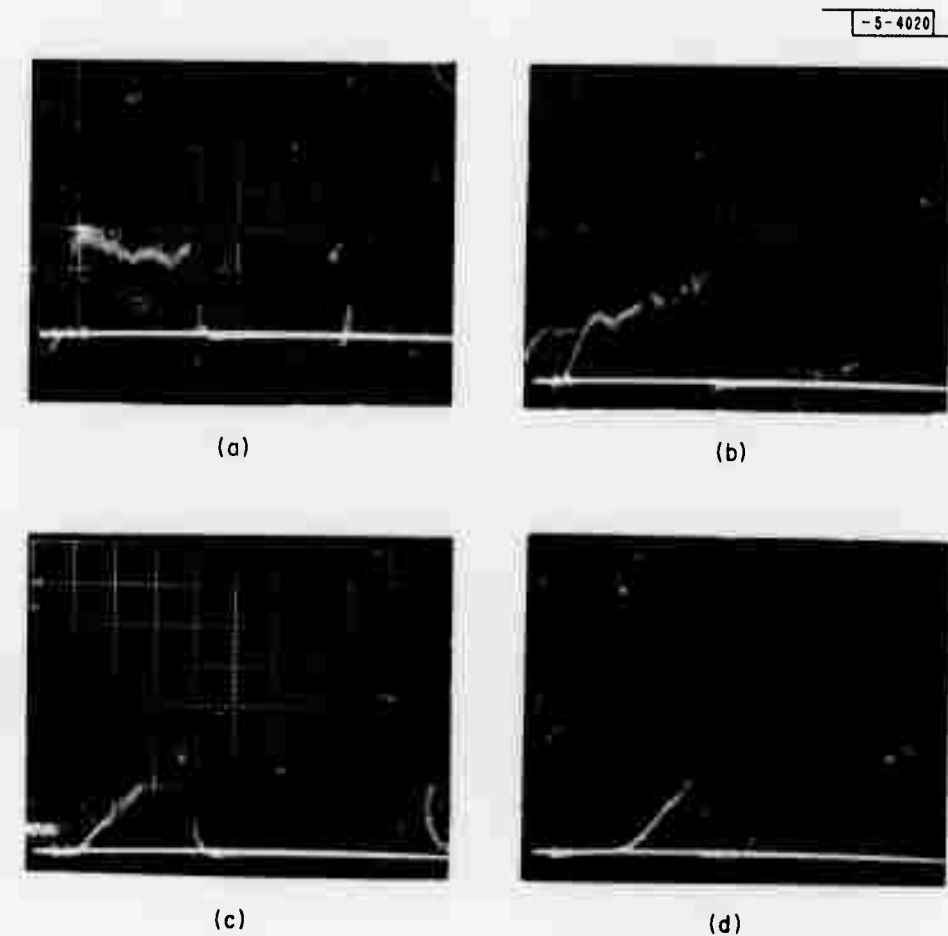


Fig. I-44. Pulse shaping using  $SF_6$  in absorption cell. Pressure of  $SF_6$  is (a) 0, (b) 10, (c) 20, and (d) 35 torr, respectively.

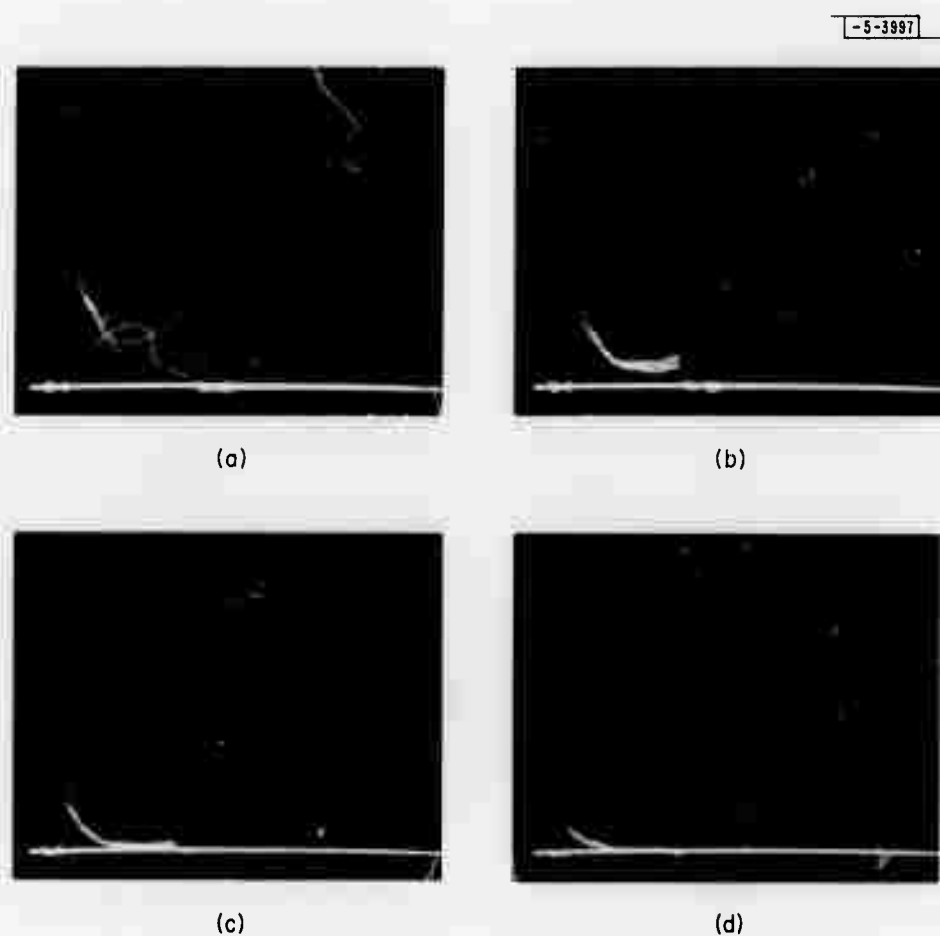


Fig. I-45. Pulse shaping using Freon 12 in absorption cell. Pressure of Freon-12 is (a) 0, (b) 40, (c) 100, and (d) 200 tarr, respectively.

## Section I

too small for appreciable energy extraction (although potentially useful in preamplification). In the third category, three electrode devices<sup>35,36</sup> are a possibility, but the discharge optically distorts the medium (especially in CO<sub>2</sub>-rich mixtures) and the gains are appreciably lower than in the last category. However, the e-beam preionized laser<sup>37,38</sup> (see also Sec. C-1-a) is a device that already approaches the capabilities necessary for the application. Likewise, the UV photoionized laser presently being researched<sup>39</sup> (see also Sec. C-2 a) offers similar promising possibilities for this application.

Both in the pulse burst and FM pulse modes, the problems of medium homogeneity and preservation of gain (and pulse coherence) during variable time intervals are important, and shall be treated subsequently. Likewise, temporal pulse distortion in both cases is important. However, there are differences that must be treated separately: the ability of the molecular medium to be reasonably utilized in times short compared with its relaxation rates, spurious FM effects due to medium dispersion, saturation, and pulse sharpening.

The following relaxation time calculations<sup>40</sup> were done for a He:N<sub>2</sub>:CO<sub>2</sub> mixture of 3:2:1 at a total pressure of 1 atm. The results are easily scaleable in pressure. The inter-rotational relaxation rate is  $\sim 0.12 \text{ nsec-atm}$ <sup>41</sup>; therefore, sufficiently strong nanosecond pulses will dump all the rotational levels of the 001 vibrational state, while such a pulse would be too fast to dump any of the higher vibrational 00r<sub>3</sub> states of CO<sub>2</sub> [ $\tau_{00\eta} \geq 3 \text{ nsec-atm}$  (CO<sub>2</sub>)], or allow replenishment by the nitrogen pump ( $\tau_{N_2} \sim 120 \text{ nsec-atm}$ ). Since these two mechanisms contribute to the efficiency of energy extraction in CO<sub>2</sub>, the saturation intensity would be reduced by at least an order of magnitude for individual pulses. However, the higher vibrational states would partially repump before the next pulse comes through, and the nitrogen would weakly repump during a sequence of such pulses.

A single arbitrary pulse (in time) passing through a high gain amplifying laser medium will distort in shape, because its leading edge always sees an unsaturated gain and will grow exponentially (until other loss mechanisms come into play), while the back sections of the pulse will see a successively more saturated gain medium. This results in pulse sharpening at the leading edge (and a corresponding frequency domain distortion that is important in the FM mode). For the nanosecond pulses, the CO<sub>2</sub> laser acts as a two-level (total vibrational state populations) system and the interaction of the population inversion and optical field growth can be shown to be described by<sup>42</sup>

$$\eta(x, t) = \frac{\eta_O(x) \exp[-N\sigma \int_0^x \eta_O(x') dx']}{\exp[N\sigma c \int_{-\infty}^{t-x/c} \varphi_O(t') dt'] + \exp[-N\sigma \int_0^x \eta_O(x') dx'] - 1}$$

and

$$\varphi(x, t) = \frac{\varphi_O(t - x/c)}{1 - \{1 - \exp[-N\sigma \int_0^x \eta_O(x') dx']\} \exp[-N\sigma c \int_{-\infty}^{(t-x/c)} \varphi_O(t') dt']}$$

where

$$\varphi = \frac{2\Phi}{n_1 + n_2} \quad , \quad \eta = \frac{n_2 - n_1}{n_2 + n_1} \quad , \quad N = n_2 + n_1$$

and

$\Phi$  = number of photons/volume

$n_i$  = particle density in respective vibrational states

$\sigma$  = resonance absorption cross section/active molecule.

For a uniform axial gain profile  $\eta(x, 0) = \eta_0$  and a specified pulse form  $\varphi(0, t)$ , the output pulse can then be integrably determined. The distortion of a Lorentzian pulse of shape

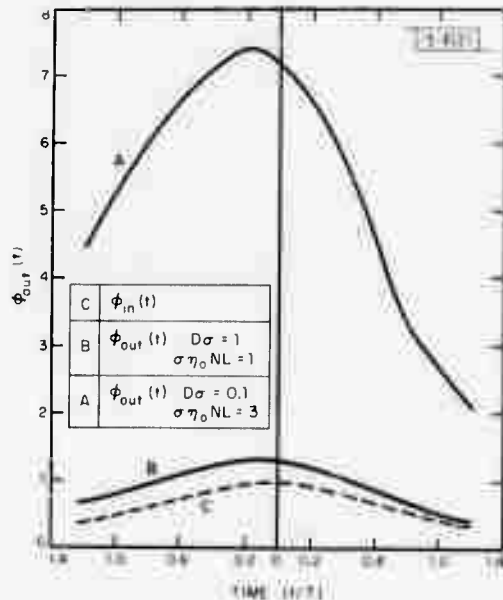
$$\varphi_{in}(t) = \frac{2DT}{N\pi C} \left( \frac{1}{t^2 + T^2} \right)$$

has an output shape of

$$\varphi_{out} = \frac{(2DT/N\pi C) [1/(t^2 + T^2)]}{1 - \{1 - \exp[-\sigma\eta_0 NL]\} \exp\{-D\sigma[1 + (2/\pi)\tan^{-1}(t/T)]\}}$$

as shown in Fig. I-46.

Fig. I-46. Photon pulse shape of output of amplifier normalized to input for a Lorentzian-shaped pulse. [Reprinted with permission from E.L. Steele, Optical Lasers in Electronics (Wiley, New York, 1968), p. 158.]



A square pulse going through the medium experiences a much more severe sharpening at the front edge:

$$\varphi_{in} = \frac{2\Phi_0}{N} [U_{-1}(t) - U_{-1}(t - \tau_0)]$$

$$\varphi_{out}(t) = \frac{(2\Phi_0/N) [U_{-1}(t) - U_{-1}(t - \tau_0)]}{1 - \{1 - \exp[-\sigma\eta_0 NL]\} \exp[-2\sigma\Phi_0 t]}$$

as exhibited in Fig. I-47.

Independent of the particular waveform, we can estimate the total energy that a pulse of a given input energy will extract from the medium, with a knowledge of the small signal gain and

## Section I

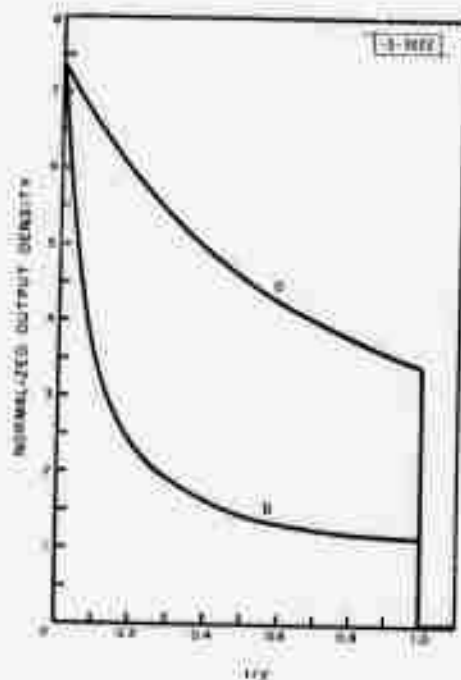


Fig. I-47. Ratio of output photon density  $\eta_L(t)$  to input photon density  $\eta_0$  vs time in units of pulse width  $\tau$  for an initially square pulse traversing an amplifying medium of length  $L = 10 \text{ cm}$ , initial difference of excited and ground state densities  $\Delta_0 = 8 \times 10^{18} \text{ cm}^{-2}$ , and resonance cross section  $\sigma = 2.5 \times 10^{-20} \text{ cm}^2$ . Total number of photons per unit area in pulse is  $\eta = 4 \times 10^{18} \text{ cm}^{-2}$  for curve a, and  $\eta = 4 \times 10^{19} \text{ cm}^{-2}$  for curve b. [Reprinted with permission from L.M. Frontz and J.S. Nodvik, J. Appl. Phys., 34, 2348 (1963).]

amplifier dimensions. Thus, we can write for the instantaneous power<sup>16</sup>:

$$P_{\text{out}}[t + (L/e)] = P_{\text{in}}(t) \left\{ G_0 / \left[ G_0 - (G_0 - 1) G_0^{-W_{\text{in}}(t)/W_0} \right] \right\}$$

where the stored energy in the medium is

$$W_0 = \frac{1}{2} h\nu \Delta N$$

$\Delta N$  is the initial population inversion,  $G_0 = e^{g_0 L}$  is the initial small signal gain, and

$$W_{\text{in}}(t) = \int_{-\infty}^t P_{\text{in}}(t') dt'$$

$$W_{\text{out}}(t) = \int_{-\infty}^t P_{\text{out}}(t') dt' .$$

From the power expression, we can estimate the expected length necessary for a given system and an effective amplifier cross section. It can be shown that the gain and energy satisfy the relation<sup>43</sup>

$$\frac{W_{\text{in}}/W_0}{G_0} G_0 = G_0 \frac{W_{\text{out}}/W_0}{G_0} + G_0 - 1$$

or

$$L = \frac{W_{\text{out}} - W_{\text{in}}}{h\nu \Delta N A} + \frac{1}{g_0} \ln \left( \frac{\sinh \frac{g_0 W_{\text{out}}}{h\nu \Delta N A}}{\sinh \frac{g_0 W_{\text{in}}}{h\nu \Delta N A}} \right) .$$

We have used a program implemented by S. Marcus (see Sec. C-1-b) to calculate the inversion for a 3:2:1 mixture pumped by a preionizing e-beam over a range of primary currents, and a range of total pressure holding E/P constant. Table I-2 gives estimates of the amplifier dimensions one might use for a multistage amplifier system to bring the individual pulses from  $2 \times 10^{-6}$  to 2 J total energy ( $\sim$ nanosecond pulses and  $10 \text{ mA/cm}^2$  primary current; the length restriction is somewhat relaxed for pulses long enough to tap the entire energy reservoir of the  $\text{CO}_2\text{-N}_2$  vibrational states). In practice, several stages would be used, the cross section increasing as the energy in the pulse increased.

At this juncture, it might be suggested that a solution to part of the restrictions is to run the amplifier system unsaturated, thus eliminating temporal pulse distortion (the unsaturated requirement being more easily achieved for the longer FM pulses). If the duty cycle of the amplifier is small, then it is necessary to avoid pumping the medium as hard with excitation energy because some fraction ( $\sim$ 75 percent) will always go into medium heating and the remainder will be dissipated by this means also, if not extracted as optical energy. Since a gas (translational) temperature rise of about  $300^\circ\text{K}$  completely shuts off the gain mechanism, and this is one of the two significant sources of pulse distortion, techniques to minimize the heating over the range of operational modes must be utilized. For the long coherence time, it should be possible to reduce the primary pumping (or secondary accelerating field) so that the gain buildup-to-optimum time is extended to about the time that the next pulse arrives. Thus, medium heating is reduced to preserve medium quality for longer periods. Sufficiently fast flow rates would aid in this effort. Calculations of the pumping and flow requirements are presently being made. A serious source of medium distortion is the pressure shock wave which emanates from the cathode. One hypothesis is that this develops from sharp temperature differences due to ion acceleration and then ion-neutral and ion-cathode collisions in the cathode fall region. Within the time for the wave to travel at the speed of sound transversely across the amplifying medium, significant index-of-refraction changes can occur and distort the medium. Basic research is needed to study this effect and means of diminishing or eliminating the shock during the operation time of the amplifier.

In the FM pulse sequence, another potential problem that was investigated was the artificial frequency chirping due to a strongly varying index of refraction (anomalous dispersion) in the frequency range over which the pulse changes. The medium index of the  $\text{CO}_2$  is given by<sup>44,45</sup>

$$\eta(\nu) = 1 - \frac{c}{\nu^2 \pi} \frac{g_0}{2} \frac{(\Delta\nu)(\nu_0 - \nu)}{(\Delta\nu)^2 [1 + (I/I_s)] + (\nu_0 - \nu)^2} + \beta = \eta_0(\nu) - \Delta\eta(\nu)$$

TABLE I-2  
SHORT-PULSE POWER AMPLIFIER LENGTH

A ( $\text{cm}^2$ )	L (m)
0.01	322
0.03	107
0.10	32
0.30	11
1.00	3.3
3.00	1.2
10.00	0.45
30.00	0.24
100.00	0.17

## Section I

where the first term is the VHF limit of  $\eta$ , the second term represents the significant dispersion in the gain region, and the third term represents the contribution from all other higher frequency molecular and electronic absorption bands. In this expression,  $g_0$  is the line center power gain,  $\nu$  is the frequency of the radiation,  $\nu_0$  is the line center gain frequency,  $\Delta\nu_0$  is the gain half-bandwidth (at half-power), and  $c$  is the speed of light. The second term could conceivably contribute significantly to index and, hence, wavenumber changes across our chirped pulse, producing a phase velocity dependent on frequency, and thus artificial chirping. Imagine that we send in a pulse whose envelope is a square wave of duration  $T$  and whose fine structure is given by

$$I(t) \propto \cos \left\{ 2\pi \left[ \nu_0 + \frac{\delta\nu}{T} (t - \frac{T}{2}) \right] t \right\}$$

then the approximate fine structure frequency distribution is given in Fig. I-48 vs the anomalous dispersion of the medium in that region.

18-5-4023

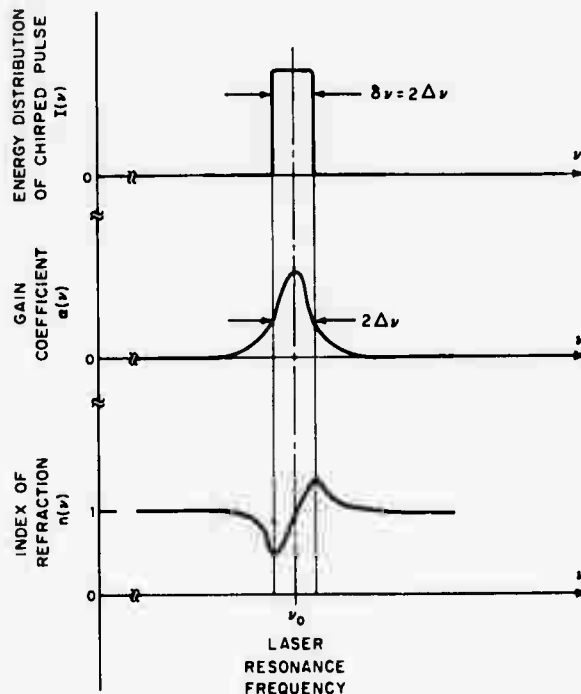


Fig. I-48. Frequency content of chirped pulse in region of resonant gain and anomalous dispersion.

If we ask the change in chirp, we find that a chirp of  $\delta\nu/T$  without dispersion becomes

$$\frac{\delta\nu}{T + \delta t} \approx \frac{\delta\nu}{T} \left( 1 - \frac{\delta t}{T} \right)$$

with dispersion. So the condition for the change in chirp to be negligible is for

$$\delta\nu\delta t = \delta\nu \frac{\Delta n z}{c} \ll 1$$

## Section I

For a chirp  $\delta\nu = 2\Delta\nu = 500 \text{ MHz}$ , and a length of 1 m,

$$\delta\nu\delta t = 10^{-15}$$

which is indeed negligible.

Power saturation of the medium is seen to simply smooth out the local dispersion effect. Saturation will also cause some bending of the wavefront at a fixed transverse cross section of the pulse if the intensity strongly varies across that cross section. It is clear that a power difference twice saturation across the transverse direction will produce a phase shift of half the magnitude at the leading edge ( $\delta\nu = \Delta\nu$ ) across the beam. The index change due to dispersion, if we assume  $\delta\nu = \Delta\nu$  and  $g_0 = 0.03 \text{ cm}^{-1} = 13 \text{ dB/m}$ , is then

$$\Delta\eta(\nu_0 + \Delta\nu) = \frac{-\lambda g_0}{8\pi}$$

which corresponds to a phase shift of

$$2\pi\Delta\eta z = \frac{-\lambda(g_0 z)}{4} = \text{one wavelength}/17.3 \text{ dB of gain}$$

(i.e., if we use the full bandwidth of the amplifier for chirping). If we reduce the amplifier bandwidth used, the phase shift goes down less than linearly.

H. Granek  
R. J. Carbonc

## 2. The Possibility of Generating Laser Plasmas by Photoionization

### a. Theoretical Investigation

The possibility of producing large volume uniform plasmas, via photoionization, with electron densities on the order of  $10^{12}/\text{cc}$  and greater in high-pressure gas laser media is investigated as an alternative to the e-beam ionization technique. As in the e-beam-excited lasers, the electrons generated by photoionization would be heated in an externally applied electric field to the optimum temperature for excitation of laser states.

Two major problems are encountered. The first relates to the magnitude of the photoionization cross section  $\sigma$ . For most atoms and molecules,  $\sigma$  is on the order of 1 Mbarn =  $10^{-18} \text{ cm}^2$  (1 megabarn) for photon energies above the ionization limit. At elevated ionizing gas pressures, a large value of  $\sigma$  limits the incident photons' penetration depth to a short distance. For instance, at 1 atm the gas density  $N$  is approximately  $3 \times 10^{19}/\text{cm}^3$ , and for  $\sigma \approx 1 \text{ Mbarn}$  the penetration depth  $L = 1/N\sigma$  is  $\approx 0.3 \text{ mm}$ . In this case, an enormous electron density is produced in a thin layer of the gas, which may be of use in special applications but not for the production of large-volume plasmas.

The second problem to be considered is that the ionization potentials of molecular and atomic species, which are known to be suitable for high-pressure gas lasers, are generally fairly large. In these cases, the corresponding photon wavelengths at energies above the ionization limit lie deep in the vacuum UV, where transparent windows are not readily available and where absorption processes other than photoionization may become important in nonionizing species in the laser medium.

## Section I

Two methods are proposed to overcome these problems. The first is to seed the high-pressure laser medium with a low-partial-pressure gas having a low-ionization potential to allow ionization by photons at wavelengths larger than UV cutoff limits of available windows, and also longer than the strong UV absorption bands of the high-pressure host laser medium. The low partial pressure allows deep penetration of the ionizing photon, and hence uniform production of photoelectrons. An example of this approach is a 1-atm CO<sub>2</sub>-He-N<sub>2</sub> laser seeded with 0.1-torr cesium. The threshold for photoionization of cesium is 3250 Å, well above the wavelengths for the onset of absorption in CO<sub>2</sub> (1700 Å), N<sub>2</sub> (1450 Å), and He (500 Å). Calculation<sup>46</sup> shows that, upon irradiations by a flashlamp emitting 1 MW/cm<sup>2</sup> between 3250 Å and 2600 Å, electron density in excess of 10<sup>13</sup>/cm<sup>3</sup> may be produced. Seeding with cesium may also be applicable in the high-pressure CO laser. By generating the fourth harmonic of a Nd:YAG laser, it is possible to produce 1 J of UV in 10 nsec at 2662 Å. This wavelength is near the peak of the photoionization cross section of rubidium. Using this intense source to ionize rubidium may produce electron densities of 5 × 10<sup>12</sup>/cm<sup>3</sup>. There are a host of organic molecules which have vapor pressure on the order of 1 torr at room temperature and also have ionization potentials low enough so that UV of wavelengths larger than 1700 Å may produce photoionization. Among these are tripentylamine, tripropylamine, and tributylamine. The list of organic compounds with low ionization limits is so extensive that a search is expected to reveal several that combine the necessary characteristics of high vapor pressure, large cross section, transparency at the laser wavelength, and low ionization potential.

The second method takes advantage of the inherently large photoionization cross section of most gases and attempts to induce photoionization by means of a two-step (or multiple-step) excitation where two (or several) incident photons are absorbed by the high-pressure gas to produce a single photoelectron. In a two-step process, the photon energies can be as low as about half the ionization limit, and hence the window transmission problems become less severe. Furthermore, in a multiple-step process, the reduced size of the effective photoionization cross section would allow deep penetration of the incident photons and production of electrons over a large volume. This method may be applicable to the photoionization of one of the molecular or atomic species of the gas laser medium, or it may be applied to multiple-step photoionization of an additional gas mixed in with the host gas laser medium. One attractive situation is found in CO where the lowest lying excited electronic states are triplets lying approximately half-way to the ionization limit. The transition to the ground state is only weakly allowed so the absorption cross section is small, permitting the use of CO at 1-atm pressure. The intermediate excited states are nearly metastable with a long radiative lifetime so that large intermediate state densities may build up and give efficient photoionization in the second step. Calculation<sup>46</sup> shows that, with 1-MW/cm<sup>2</sup> illumination between 1500 Å and 2000 Å, electron densities on the order of 10<sup>13</sup>/cm<sup>3</sup> may be produced in 1 atm of CO.

J. S. Levine  
A. Javan

### b. Experimental Investigation

An ionization cell has been constructed that contains a small linear Xe flashlamp and two flat parallel electrodes. The lamp is oriented parallel to the electrodes in their midplane and outside of the uniform field region which exists when a voltage is applied, so that the volume

## Section I

between the electrodes is illuminated. All metal corners and edges are removed to minimize ionization due to corona discharge. The cell may be filled with various buffer gases and low ionization potential vapors to be irradiated with an intense pulse of UV; the electrons formed by photoionization are drawn off by the electric field between the electrodes, and the current is measured as the voltage drop across a sensing resistor in series with the high-voltage supply. Because the drift velocity of electrons in the buffer gas (nitrogen) is known as a function of electric field divided by pressure E/P, the electron density may be determined from the current measurements from the relation  $j = nev_D$ , where

$$j = \text{current density} = \text{current}/\text{area of electrode}$$

$$e = \text{electronic charge}$$

$$v_D = \text{drift velocity of electrons in buffer gas.}$$

The Xe lamp was supplied by the Xenon Corporation. It is powered by a Xenon Corporation Micropulser and can be fired at voltages between 13 and 20 kV; the maximum voltage represents an input energy of 20 J. The lamp arc length is 8 inches (the electrodes are also 8 inches long). A suprasil envelope was used to permit passage of UV down to  $1650\text{\AA}$ , although it is expected that relatively little energy is emitted at that wavelength; the output peaks around  $2600\text{\AA}$ . The light pulse has a full width at half-height of 1  $\mu\text{sec}$ .

When the cell is filled with  $N_2$  to 500 torr and a potential of typically 10 kV is applied to the electrodes, a current pulse in the sensing resistor is seen which closely follows the light pulse as simultaneously monitored with a photomultiplier. The peak current corresponds to an electron density of  $2 \times 10^8/\text{cm}^3$ . This current is interpreted as the result of photoemission from the aluminum electrodes; the time delay of less than  $10^{-9}$  sec between photon absorption and electron emission is too small to be resolved.

When 0.2-torr tripropylamine is added to the  $N_2$ , a dramatic two-order-of-magnitude increase in the current flow is seen upon flashlamp ignition. The current is found to vary linearly with the electrode voltage between the limits corresponding to  $E/P = 0$  to  $E/P = 10$ . This implies that a peak electron density on the order of  $10^{10}/\text{cm}^3$  is produced independent of the electric field. In turn, this is strong evidence that the enhancement in electron production is due to photoionization and not to ionization of tripropylamine by electron collision. If the latter were the case, then an increase in electron density would be expected as  $E/P$  (and hence the average electron energy) is increased; this, in fact, is not observed.

The time development of the current pulse is markedly different from the case of pure  $N_2$ . As seen in Fig. I-49, the electron density starts to grow only after the illumination has reached its peak and continues to grow until the light pulse terminates. Thereafter, the electron density decays - rapidly at first, and then with a long exponential tail. These observations are

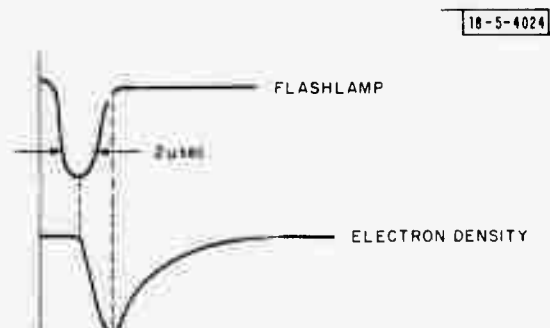


Fig. I-49. Upper trace shows light pulse from flashlamp measured by 1P28 photomultiplier tube. Lower trace is current flow between electrodes due to photoionization.

## Section I

tentatively explained as follows. Ionization takes place by a two-step process. This ionization potential is about 7.5 V so that two 2600-Å photons have sufficient energy to liberate an electron. The first photon populates intermediate states half-way to the ionization limit; the second photon then raises the excited electron into the continuum. The buildup of intermediate state population may account for the 1-μsec delay in the growth of the electron density. Initial rapid decay of the plasma may be due to recombination which proceeds at a rate proportional to  $n^2$ . When  $n$  falls to a sufficiently low value, attachment and diffusion become the dominant loss mechanisms which proceed at a rate proportional to  $n$  and give rise to an exponential decay.

The peak electron density has been measured as a function of flashlamp power. Preliminary results show that for relatively low lamp energy, the electron density increases approximately as the square of the lamp energy; for high lamp energy, electron density increases more slowly – approximately linearly with lamp energy. This behavior is consistent with two-step excitation for which ionization is proportional to lamp energy squared. At low lamp energy, and hence low electron density, electron loss varies as  $n$ ; thus, the equilibrium electron density varies as lamp energy squared. At high lamp energy, and hence high electron density, electron loss varies as  $n^2$ ; thus, the equilibrium electron density varies linearly with lamp energy.

Experimental studies are being pursued to:

- (1) Determine quantitatively the electron destruction mechanisms in tripropylamine,
- (2) Study the photoionization of other organic molecules,
- (3) Increase plasma densities by using more energetic lamps,
- (4) Produce plasmas via photoionization of cesium vapor,
- (5) Produce a low-pressure and ultimately an atmospheric-pressure  $\text{CO}_2\text{-N}_2\text{-He}$  photoionization excited laser.

J. S. Levine

### 3. Other Device Work

#### a. The Feasibility of a 10-atm $\text{CO}_2\text{-N}_2\text{-He}$ Laser

The variation in 10.6-μm small-signal gain of  $\text{CO}_2\text{-N}_2\text{-He}$  e-beam excited mixtures as a function of pressure is considered. The well-known formula for small signal gain is:

$$\alpha(\nu = \nu_0) = \frac{C^2}{8\pi^2 \nu^2 t_{\text{spont}} \Delta\nu_{1/2}} \left( N_2 - \frac{g_2}{g_1} N_1 \right)$$

where

$\alpha(\nu = \nu_0)$  = gain/centimeter at line center

$N_2$  = population density in upper level;  $g_2$  = degeneracy

$N_1$  = population density in lower level;  $g_1$  = degeneracy

$t_{\text{spont}}$  = spontaneous transition time from 2 → 1

$\Delta\nu_{1/2}$  = half-width at half-height of Lorentzian gain profile.

## Section I

In the case of CW pumping, the steady-state population density  $N_i$  in the absence of a saturating optical frequency field is the product of the excitation rate  $R_i$  and the level lifetime  $\tau_i$ . For direct electron excitation of the  $\text{CO}_2$  levels,  $R_i$  is proportional to the electron density, the  $\text{CO}_2$  ground-state density, and the electron collision cross section

$$R_i^e \sim \sigma n_e \bar{v}_e N_{GS}^{\text{CO}_2} .$$

A similar relation holds for the electronic excitation of nitrogen vibrational levels. In both cases, the rate of excitation is directly proportional to pressure. The rate of collisional transfer of excitation from nitrogen ( $\nu = 1$ ) to  $\text{CO}_2$  (001) is proportional to the excited-state nitrogen density  $N_2 (\nu = 1)$  and to the ground-state  $\text{CO}_2$  density

$$R^C \sim N_2 (\nu = 1) N_{GS}^{\text{CO}_2} \sim N_2 (\nu = 0) N_{GS}^{\text{CO}_2} .$$

Since  $N_2 (\nu = 1)$  is proportional to  $N_2 (\nu = 0)$ , the collisional transfer rate should increase with the second power of pressure. At 10 atm, the 10- $\mu\text{m}$  transitions are totally pressure-broadened; so,  $\Delta\nu_{1/2} \sim \text{pressure}$ . Further, level lifetimes are inversely proportional to pressure.

So far it appears that, in the CW limit,  $\alpha$  should vary inversely with pressure with respect to direct electron excitation, and be constant in pressure with respect to collisional transfer between  $N_2$  and  $\text{CO}_2$ . However, in the case of e-beam excitation,  $n_e$  is proportional to the square root of the energy loss of the ionizing beam to the gas per centimeter (assuming recombination is the dominant mechanism for ion loss). This stopping power is, in turn, proportional to the gas density or  $n_e \sim \sqrt{\text{pressure}}$ . Therefore, if sufficient primary electron energy is available to penetrate the medium, the gain of a high-pressure (collisionally broadened)  $\text{CO}_2$  laser should exhibit a pressure variation that is the sum of two terms. One term, due to direct electron excitation, varies as  $(\text{pressure})^{-1/2}$ ; the other, due to collisional transfer from  $N_2$  to  $\text{CO}_2$ , should increase as  $(\text{pressure})^{+1/2}$ .

The parameters appearing in the gain equation are evaluated for an 8:1:1 mixture of  $\text{He:CO}_2:\text{N}_2$  at 10-atm pressure assuming longitudinal e-beam excitation by a  $10^4 \text{ A}$ , 3-nsec e-beam source (Febatron 706). Peak gain for the  $P_{20}$  line is estimated as 2.2 percent/cm.

J. S. Levine

### b. Construction of a 10-atm $\text{CO}_2-\text{N}_2-\text{He}$ Laser

A laser has been constructed based on the calculations outlined in the preceding section. Dimensions of the active volume are  $1 \times 1 \times 20 \text{ cm}$ . Electron-beam excitation is in the axial direction, parallel to the optical axis. The e-beam is focused by means of a magnetic lens placed between the Febatron 706 source and the 2-mil titanium electron window on the laser. The mirror nearest the e-beam source is formed by a thin aluminized mylar film stretched taut over an optically flat pyrex annular ring. This mirror permits free passage of the ionizing beam while providing 96-percent reflectivity at 10.6  $\mu\text{m}$ . The far end of the laser is terminated by a KCl Brewster angle window. The optical cavity is completed by a curved, partially transmitting germanium mirror.

Further development of this system awaits the availability of the Febatron source.

J. S. Levine

## Section I

### c. Lamb Dip in Sealed-Off CO Lasers

We have completed measuring and evaluating data on the Lamb dip for 16 different rotational-vibrational transitions in sealed-off CO lasers operating at a total pressure of 1.5 torr. The experimental data of power output vs frequency were matched to theoretical curves which included relaxation across the velocity profile as a major factor limiting the depth of the Lamb dip. As a result of these investigations, the following parameters were accurately determined: the inhomogeneous and homogeneous linewidths, the relaxation rate out of the lasing level, and the cross-relaxation rate. We found that the cross-relaxation rates were of the same order in magnitude as the dephasing time. A full report detailing our work is nearing completion.

C. Freed  
H. A. Haus

## REFERENCES

1. J. W. Strohbehn, in Progress in Optics, E. Wolf, Ed., Vol. IX (North-Holland, Amsterdam, 1971), p. 73.
2. J. Herrmann and L. C. Bradley, "Numerical Calculation of Light Propagation," LTP-10, Lincoln Laboratory, M.I.T. (12 July 1971), DDC AD-902041-L.
3. F.G. Gebhardt, D. Smith, R.G. Buser and R. Rohde, J. Opt. Soc. Am. 62, 924 (1972).
4. F.G. Gehhardt, United Aircraft Research Laboratories Report 921004-8, Annual Report on Army Contract DAAB07-70-C-0204 with U.S. Army Electronics Command for period 30 April 1971 to 29 April 1972 (July 1972).
5. J.O. Hinze, Turbulence (McGraw-Hill, New York, 1959).
6. D.E. Lencioni, L.C. Marquet and R.J. Hull (to be published).
7. L.C. Marquet, R.J. Hull and D.E. Lencioni, "Studies of Breakdown in Air Induced by a Pulsed CO<sub>2</sub> Laser," VII International Quantum Electronics Conference, University of Toronto, Ontario, Canada, 8-11 May 1972.
8. D.C. Smith, Appl. Phys. Letters 19, 405 (1971).
9. N. Kroll and K.M. Watson, Phys. Rev. A 5, 1883 (1972).
10. Optics Research Report, Lincoln Laboratory, M.I.T. (1971:1), p. 11, DDC AD-888823-L.
11. J.E. Lowder, R.W. O'Neil, L.C. Marquet, D.E. Lencioni, C.W. Kielline, H. Kleiman, R.J. Hull and T.W. Hilton, LTP-17, Lincoln Laboratory, M.I.T. (to be published).
12. A.N. Pirri, Appl. Phys. Letters 21, 79 (1972).
13. S.I. Drabkina, Zh. Eksp. Teor. Fiz. 21, 473 (1951).
14. N.M. Gegechkori, Zh. Eksp. Teor. Fiz. 21, 493 (1951).
15. A.A. Offenberger, R.D. Kerr and P.R. Smy, J. Appl. Phys. 43, 574 (1972).
16. A.A. Offenberger and R.D. Kerr, J. Appl. Phys. 43, 354 (1972).
17. I.L. Zel'manovich and K.S. Shifrin, Tables of Light Scattering, Vol. III: Coefficients of Extinction, Scattering, and Radiation Pressure (Hydrometeorological Press, Leningrad, 1968), p. 345.

18. D.H. Douglas-Hamilton, private communication (to be published).
19. W.L. Nighan, private communication.
20. R.L. Taylor and S. Bitterman, Rev. Mod. Phys. 41, 26 (1969).
21. W.W. Rigrod, J. Appl. Phys. 36, 2487 (1965).
22. A.E. Siegman and H.Y. Miller, Appl. Opt. 9, 2729 (1970).
23. J. Wallace, AERL private communication.
24. R.L. Sanderson and W. Streifer, Appl. Opt. 8, 2129 (1969).
25. W.F. Krupke and W.R. Sooy, IEEE J. Quantum Electron. QE-5, 575 (1969).
26. I.S. Gradshteyn and I.W. Ryzhik, Table of Integrals, Series, and Products (Academic Press, New York, 1965), Eq. 6.633.2.
27. W. Magnus, F. Oberhettinger and R.P. Soni, Formulas and Theorems for the Special Functions of Mathematical Physics (Springer-Verlag, New York, 1966), p. 242.
28. S. Marcus, Appl. Phys. Letters 21, 18 (1972).
29. G. Mouron, B. Dronin and M. Denariez-Roberge, Appl. Phys. Letters 20, 453 (1972).
30. E. Gerry and D. Leonard, Appl. Phys. Letters 8, 227 (1966).
31. T.J. Bridges, H.A. Haus and P.W. Hoft, IEEE J. Quantum Electron. QE-4, 777 (1968).
32. C. Freed and A. Javan, Appl. Phys. Letters 17, 53 (1970), DDC AD-714750.
33. A.E. Eckbreth and J.W. Davis, IEEE J. Quantum Electron. QE-8, 139 (1972).
34. T.J. Bridges, E.G. Burkhardt and P.W. Smith, Appl. Phys. Letters 20, 403 (1972).
35. A.K. LalFlamme, Rev. Sci. Instr. 41, 1578 (1970).
36. P.R. Pearson and H.M. Lamberton, IEEE J. Quantum Electron. QE-8, 145 (1972).
37. C.A. Fenstermacher, M.J. Nutter, W.T. Leland and K. Boyer, Appl. Phys. Letters 20, 56 (1972).
38. J.D. Daugherty, E.R. Pugh and D.H. Douglas-Hamilton, 24th Annual Gaseous Electronics Conference, Gainesville, Florida, 5-8 October 1971.
39. H.J.J. Sequin and J. Tulip, VII International Quantum Electronics Conference, University of Toronto, Ontario, Canada, 8-11 May 1972.
40. R.L. Taylor and S. Bitterman, Rev. Modern Phys. 41, 26 (1969).
41. P.K. Cheo and R.L. Abrams, Appl. Phys. Letters 14, 47 (1969).
42. E.L. Steele, Optical Lasers in Electronics (Wiley, New York, 1968).
43. A.E. Siegman, J. Appl. Phys. 35, 460 (1964).
44. D.H. Close, Phys. Rev. 153, 360 (1967).
45. M. Born and E. Wolf, Principles of Optics (Pergamon Press, New York, 1959).
46. J.S. Levine and A. Javan, "The Possibility of Generating Laser Plasmas by Photoionization" (to be published); A. Javan and J.S. Levine, "The Feasibility of Producing Laser Plasmas via Photoionization," IEEE J. Quantum Electron. (to be published).

## II. OPTICAL MEASUREMENTS AND INSTRUMENTATION

### A. ZnS UP-CONVERSION

Additional parameters relevant to the up-conversion process in ZnS have been measured. Whereas previous measurements have been primarily concerned with the effects of DC IR radiation, AC effects have also been measured now using chopped IR radiation as a source and constant UV illumination for excitation. Under these conditions, an AC visible output is observed on a DC background. At frequencies on the order of typical TV scanning rates, the following results were obtained:

- (1) Peak-to-peak AC visible output decreases about 50 percent in going from 1 to 64 Hz;
- (2) AC visible output increases with increasing UV intensity;
- (3) AC to DC background ratio decreases with increasing UV intensity;
- (4) AC signal-to-noise ratio (SNR) increases somewhat with increasing UV intensity;
- (5) AC SNR is 1 to 2 orders of magnitude worse than the SNR obtained in previous measurements where the phosphor is exposed to DC IR radiation after (not during) UV excitation. This is due to the large background noise caused by constant UV illumination in the AC case.

These results, and others, simply confirm the fact that in these materials it takes a finite time (several seconds) to excite electrons to states which will produce the maximum stimulation effect. Under AC operation, even at low frequencies, there is not enough time for significant UV excitation between IR pulses. In other measurements, we have determined that the spectral character of the visible output is dependent upon the IR stimulation wavelength. Our results show that 10- $\mu\text{m}$  radiation produces a band of visible radiation centered near 5300 Å, while 2- $\mu\text{m}$  radiation produces a band centered nearer 5400 Å.

Presently, we are constructing apparatus to determine the S/N characteristics of the phosphor screen resolution elements under uniform IR illumination. We expect to determine the degree of nonuniformity in response due to irregularities in particle size, particle distribution and layer thickness. The smallest particle size range is 10 to 20  $\mu\text{m}$ .

W. J. Scouler

### B. IR CAMERA (4 inch)

In measurements relevant to the imaging quality of the ZnS up-converter phosphors, we have used the cooled, 4-inch-diameter, f/1.0, 3-element-refractor camera shown schematically in Fig. II-1.

The camera has a 0.25-rad FOV and is diffraction limited over the design wavelength range of 7.5 to 12  $\mu\text{m}$ .\* A refractor was chosen over a reflector for the f/1.0 design as it has a simpler and more compact configuration.

\* Optical design by David Grey Associates, Waltham, Mass.

## Section II

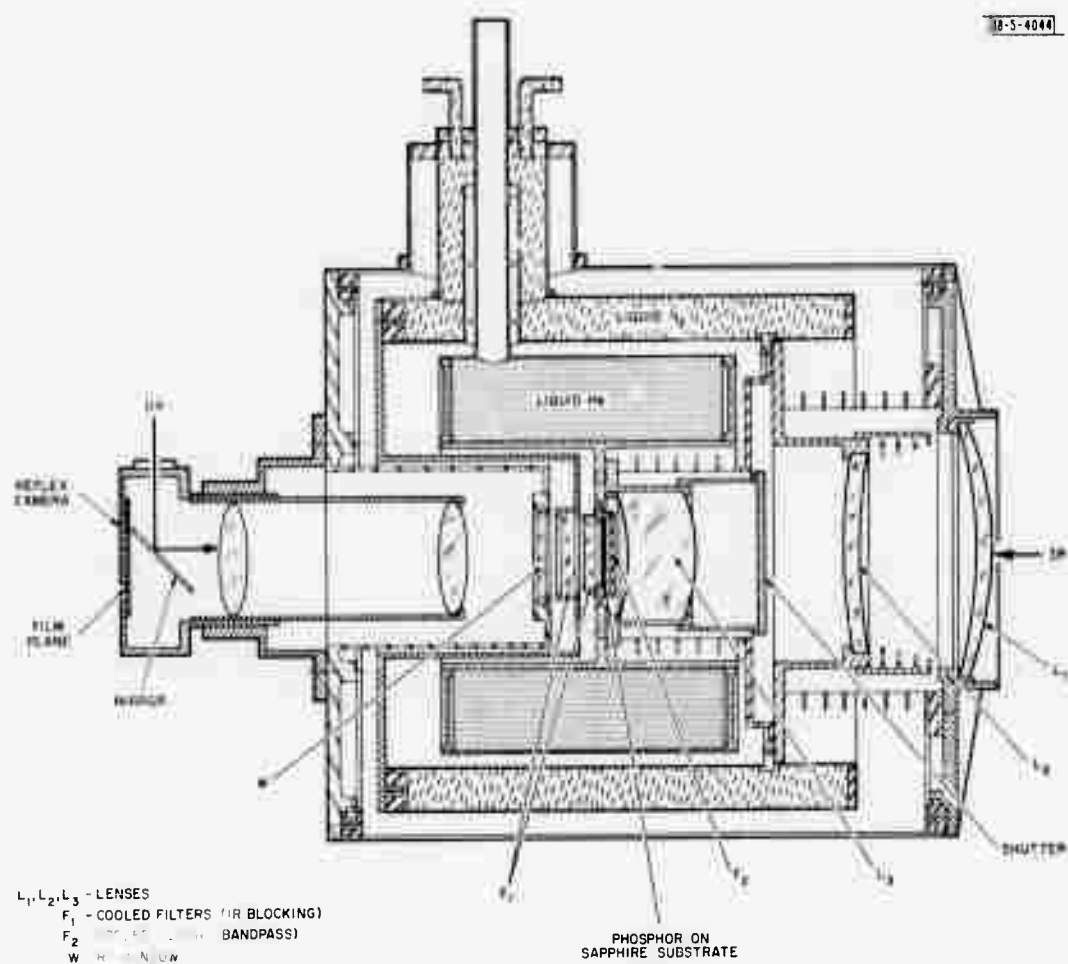


Fig.II-1. Schematic of 4-inch f/1, 0.25-rod FOV, diffraction limited IR camera.

## Section II

An important consideration in the design is the reduction to a minimum of extraneous IR radiation at the image plane. This was achieved by cooling  $L_3$  to liquid-He temperature and  $L_2$  to liquid- $N_2$  temperature and then mounting between them a shutter cooled to nearly liquid-He temperature and activated via an O-ring seal at room temperature. Cooling  $L_2$  to liquid- $N_2$  temperature reduces the heat load to the liquid-He section while reducing emission from  $L_2$ . The cooled shutter prevents any front-end IR radiation from reaching the phosphor until the scene is to be viewed.

Behind the phosphor screen are IR blocking filters which absorb radiation greater than  $2\text{ }\mu\text{m}$  while being highly transmitting to both visible and UV radiation. Each set of filters, one at liquid- $N_2$  and one at liquid-He temperature, consists of one 3-mm-thick Oriel 7100 filter and one 3-mm-thick piece of plexiglas. The attenuation of  $\text{IR} > 2\text{ }\mu\text{m}$  is about  $10^{-5}$  in each set. The UV excitation light and the visible luminescence from the phosphor are viewed via the reflex camera used to photograph the phosphor image.

The 4-inch-diameter Ge collector lens  $L_1$  also serves as the vacuum window. A simple stress analysis shows that the atmospheric pressure produces no measurable deterioration of the diffraction limited image.  $L_1$  is held in an adjustable holder to permit some focusing ability for objects closer than infinity. A bandpass filter directly in front of the phosphor can be used to limit the wavelength range to any band between 7.5 and  $12\text{ }\mu\text{m}$ .

The reservoirs for the coolants are 1.9 and 2.7 liters, respectively, for liquid He and liquid  $N_2$  giving an operating time in excess of  $4\frac{1}{2}$  hours. Typical cool down times are on the order of 3 hours.

Mechanical rigidity and thermal isolation of the three different temperature sections are achieved using specially fabricated ribbed stainless steel tubing. These isolators have a high resistance to twist or distortion and a high thermal resistance.

Tests have demonstrated that the mechanical integrity of the design is maintained at cryogenic temperatures and that its performance is diffraction limited. This was determined experimentally by replacing the ZnS phosphor screen with a Ge:Cu detector located behind a knife edge in the focal plane, looking at a chopped blackbody source at different pointing angles. The variation in angle from cut-on to maximum signal is a measure of the image size. From our measurements of a 1-cm source at 45 m, the best image obtained had a  $38\text{-}\mu\text{m}$  diameter. This is to be compared to a theoretically calculated value of  $34\text{ }\mu\text{m}$ , which is within experimental limits.

Rotation of the camera through large angles produces the signal vs angle curve of Fig. II-2. This curve was obtained with a Ge:Cu detector located behind a mask at the focal plane defining an area on the detector of  $1.5 \times 3\text{ mm}$ . The width of the central peak corresponds to the 1.5-mm slit width, which is much larger than the image size. Thus, the detector acceptance area for scattered radiation is much larger than is necessary to view the direct image. If the detector area were reduced to just accept the direct image, then the off-axis signal would be about 3 orders of magnitude lower than shown. Note that at angles of about  $18^\circ$  from the normal, there are peaks at about  $1/3000$  of the signal detected with the camera pointed at the source. Some effort has been made experimentally (so far unsuccessfully) to determine the cause of these peaks. In addition, computer calculated ray-traces of several assumed reflection possibilities have produced no equivalent path of suspected rays.

## Section II

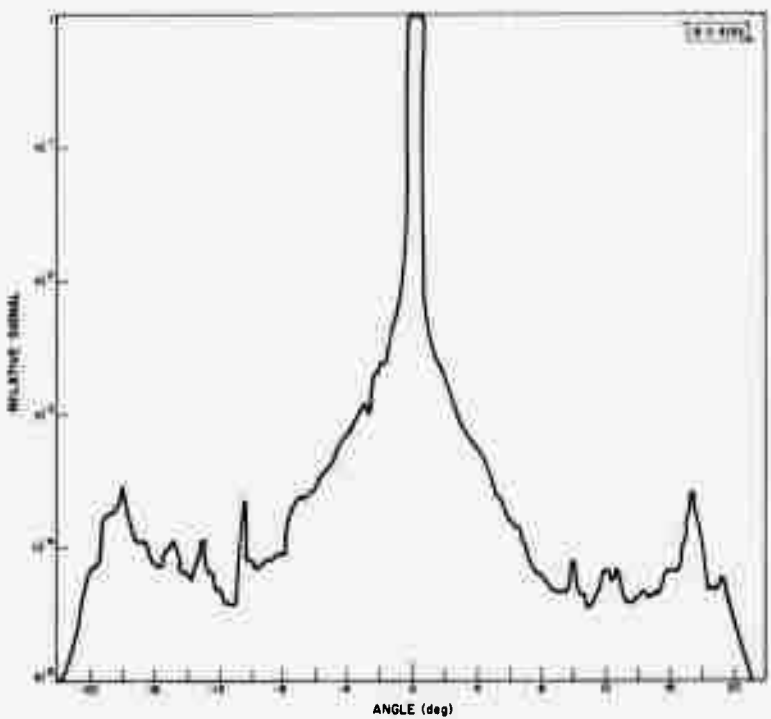


Fig. II-2. Detector signal vs angle. Angle in degrees is amount blockbody source is located off optical axis.

Presently, a second set of lenses ( $L_1$ ,  $L_2$  and  $L_3$ ) is being set up on an optical bench at room temperature in an attempt to discover the path of the extraneous rays.

D. H. Dickey  
T. M. Quist  
W. J. Scouler

### C. INTERFEROMETRIC IMAGING TECHNIQUES

#### 1. Introduction

The most serious limitation to using the interferometric imaging technique from the KC-135 aircraft in flight is suspected to be the presence of an image degrading boundary layer. The earlier reported retroreflector type measurements showed that an image degradation arises between the wing tip of the aircraft and the skin.<sup>1</sup>

In these experiments, the measured modulation transfer function (MTF) fell quite rapidly to low contrast values, and there was some question raised as to whether the MTF actually represented only the boundary layer (near the skin of the aircraft). In order to confirm that the degradation was in fact localized near to and just outside the aircraft window, a new experiment was designed and carried out.\*

The boundary layer localized in the first 25 cm away from the skin of the aircraft was measured in this experiment. In so doing, it was shown that the interferometer performed properly

\* Experiment planned and implemented in cooperation with D. G. Kocher and B. W. Bryant in support of the LFLC telescope seeing assessment work, but using the interferometer as a sensor.

## Section II

out to the highest spatial frequency (maximum shear value) and demonstrated that the effects of vibration, air currents inside the aircraft cabin near the window and temperature gradients across the optical window produced no significant part of this degradation.

MTF measurements of the boundary layer were made both at the front (LFLC) window and at the third window in the aft array. The measurements were then compared with the earlier retroreflector results.

### 2. Experimental Program

A schematic of the experimental setup is shown in Fig. II-3. A 5-mW He-Ne CW laser (wavelength 632.8 nm) was mounted rigidly on top of the interferometer. A high quality 50-mm-aperture laser beam expanding telescope was used with the laser to provide a collimated and coherent laser beam. A mirror and a beam splitter, mounted to allow angular adjustments in each case, were arranged to direct the 50-mm collimated laser beam through a 75-mm-diameter optical window in the side of the aircraft. The beam then propagated through the

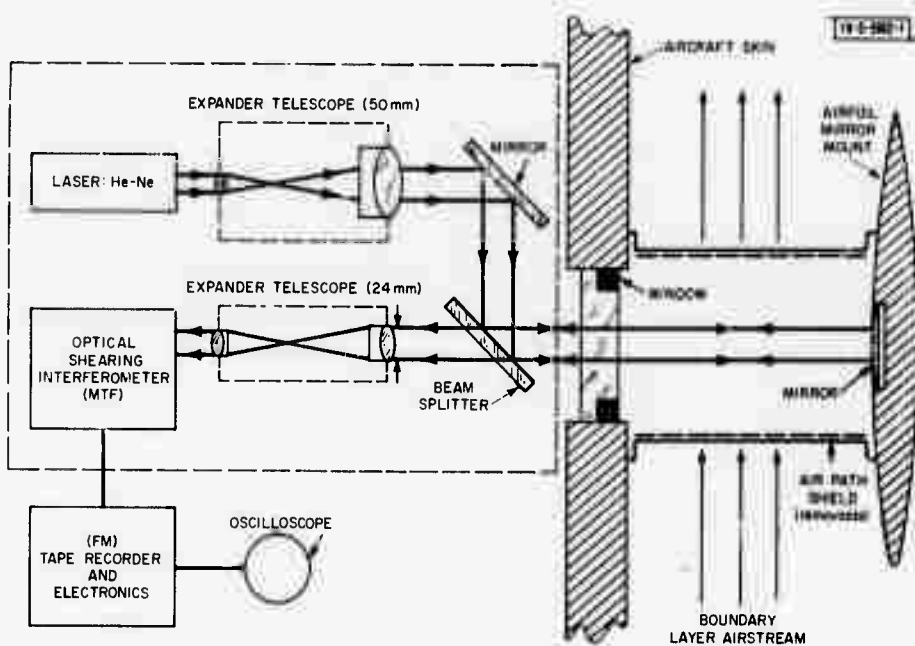


Fig. II-3. Schematic of interferometric boundary layer MTF measurement.

airstream (the boundary layer) to a gold-coated mirror 34 mm in diameter (supported on an airfoil outside the aircraft) where it was reflected back through the boundary layer and the optical window. The mirror was located 25 cm from the window face outside the aircraft. Both the window and mirror were mounted in an aerodynamically designed airfoil plate unit made of aluminum, which can be fitted into any of the aircraft window locations in place of the standard 22-inch-diameter optical windows of the KC-135 aircraft.\* An aerodynamically designed tube (an airflow

\* Airfoil plate design by R. Stiles, Airborne Research & Engineering, Hanscom AFB.

## Section II

shield) could also be readily fitted (on the ground) between the gold-coated mirror and the 75-mm-optical window to completely enclose and shield the light path outside the aircraft from the boundary layer.

The laser beam returned through the optical window, following the double pass through the boundary layer, and passed next through the beam splitter to a second smaller 24-mm-aperture beam reducing telescope. The beam was reduced in diameter to about an 8-mm collimated beam and then passed through a dove prism and finally to the corner cube shearing interferometer.<sup>2</sup> The dove prism rotated the wavefront around the optical axis, to allow measurements for different diametrical orientations of the shear axis. The diameter of the collimated laser beam through the boundary layer was limited by the diameter of the entrance aperture of the telescope to a nominal 24 mm.

All the auxiliary optical components arranged in this experimental setup were of very high optical quality, to ensure that the wavefront entering the interferometer, in the absence of the boundary layer, was plane to within 1/10 wave.

A photograph of the interferometer and the laser source, with the auxiliary optical components in place, is shown in Fig. II-4(a). The complete unit was mounted on a rigid tripod, which allowed angular and translational adjustments to be made and allowed the laser beam to be directed through the 75-mm-diameter window in the airfoil plate (a paper mask in the photograph shows the location of the airfoil plate and the two windows). A photograph of the airfoil plate in position outside the aircraft is shown in Fig. II-4(b). The laser beam passes and returns through the left hand window in Fig. II-4(b). The tripod was bolted to the floor to produce a relatively rigid mounting. The laser beam was aimed through the right hand window as seen in Fig. II-4(a) and a second window (to the left of the laser beam window) in the airfoil plate served simply for visual observation.



Fig. II-4(a). Interferometer at LFLC window position in aircraft.



Fig. II-4(b). Airfoil plate from outside aircraft (airflow shield removed).

All the electrical measurements were recorded on an FM tape recorder and the data were analyzed on the ground in the laboratory. An oscilloscope display of all the signals provided continuous real-time monitoring of the data being recorded and permitted accurate electro-optic focusing of the telescope in flight before each MTF run.

Both of the two airfoil plate windows had provision for either a single or double (airspaced) optical window mounting (to circumvent frosting problems), but only the single window unit was employed in the experiment reported here.

### 3. Results

Seven daylight flights (at about 40,000 feet altitude) were carried out. In-flight MTF measurements were performed with the airflow shield in place (no boundary layer) and with it removed (boundary-layer measurement). An earlier check of the complete system was done in the laboratory and in the aircraft on the ground. MTF measurements in flight were made at the LFLC window position (located well forward of the wing, 7 m from the aircraft nose) and at the third mount aft array window position (located over the wing, 18 m from the aircraft nose). The interferometer was tripod-mounted for the LFLC window measurement, and was placed on the fixed gimbaled mount (with micrometer adjustments) for the third mount measurement.

MTF measurements were made for different orientations ( $2\varphi$ ) of the wavefront, corresponding to the MTF along a horizontal ( $2\varphi = 0^\circ$ ), inclined ( $2\varphi = 45^\circ$ ) and vertical ( $2\varphi = 90^\circ$ ) axis. This will suffice to establish whether there is any asymmetry in the wavefront arising from a non-symmetry in the boundary layer. Each telescope could be independently and accurately focused, and the focus was checked before each MTF run by maximizing the signal on the scope display at a shear setting of approximately  $s = 1.0$ . The parameter  $s$  is defined as a reduced spatial frequency  $s = 2\lambda RF$ , where  $\lambda$  is the wavelength (in cm),  $R$  is a spatial frequency (in cycles per cm), and  $F$  is the ratio of the focal length to aperture diameter of the optics.

The MTF measurements obtained at the third mount aft array window are shown in Fig. II-5 (from 3 flights). A similar set of data were obtained at the LFLC position, and the respective mean MTF for each window position, is shown compared in Fig. II-6. In both figures the diffraction limited (clear aperture) MTF curve is shown. The data represent a double pass through the boundary layer.

With the airflow tube in place (no boundary layer), the MTF is close to the diffraction limited curve (curve 1, Fig. II-5). When the tube is removed (boundary layer present) the MTF falls (curve 2, Fig. II-5). These data characterize the image degradation due to the boundary layer during daylight flights at 40,000 feet altitude and at normal cruising speed. There is no significant difference in data obtained for different pupil rotations (at  $0^\circ$ ,  $45^\circ$  and  $90^\circ$ ) corresponding to different shear orientations along the wavefront diameter. There appears therefore to be no asymmetry in the degradation due to the boundary layer.

Since with the air flow tube in place the MTF measured is virtually diffraction limited, there cannot be any significant degradation arising from extraneous air currents near the window inside the aircraft, nor from temperature gradients in the optical window itself.

In order to compare these data with the theoretical prediction available at this time, the characteristics of the refractive index (or temperature) fluctuations in the turbulent airstream must be evaluated. These in turn will determine the random wavefront errors from which the MTF can be computed for this case.

## Section II

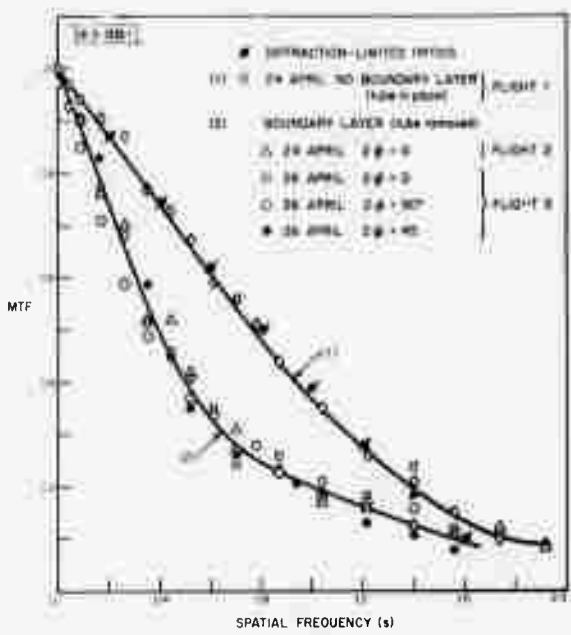


Fig. II-5. MTF of aircraft boundary layer at third window/aft array.

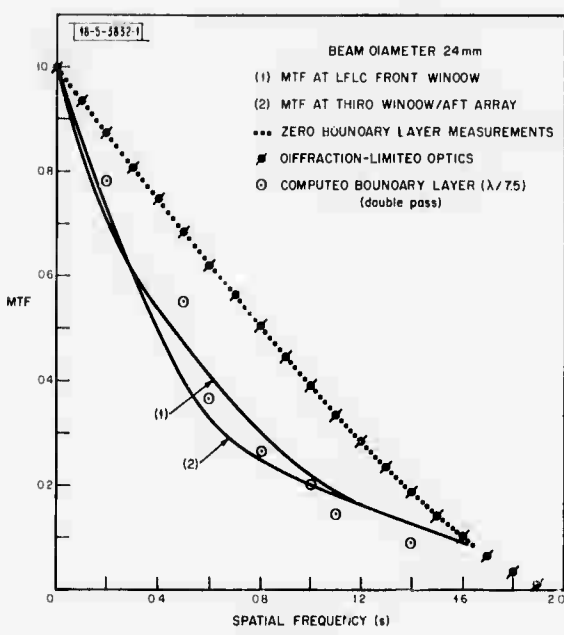


Fig. II-6. MTF of in-flight aircraft boundary layer at front (LFLC) and third window/aft array.

As a rough estimate of the wavefront errors in the present instance for a double pass through the aircraft boundary layer, a fluctuation for the optical phase (path length) of  $\lambda/7.5$  is believed to be of the right order.\* This value will be used without detailed discussion to make a preliminary comparison with theory. Barakat<sup>3</sup> has shown that the MTF can be calculated from random wavefront errors. Using his method, the correlation parameter<sup>4</sup> was roughly estimated from our earlier retroreflector MTF measurements. For  $\sigma = \lambda/7.5$ , the MTF [ $\psi(s)$ ] was then computed from the relationship given by Barakat

$$\frac{\psi(s)}{\psi_0(s)} = \exp\{-k^2\sigma^2 [1 - \exp(-as^2)]\}$$

where  $\psi_0(s)$  is the diffraction-limited MTF,  $s$  is the reduced spatial frequency and  $k = 2\pi/\lambda$ .

This computed curve, for the conditions spelled out above, is shown by the points on Fig. II-6. While the present analysis is incomplete and should be regarded as tentative, a comparison between the measured and computed curve shows satisfactory agreement.

In order to compare the present results with those previously obtained in the wing-tip retroreflector experiment, in which data for effectively a single pass were obtained with an 89-mm-diameter beam (with a central obscuration  $\alpha = 0.34$ ), a certain amount of extrapolation is called for.

The equivalent single-pass MTF through the boundary layer, can be obtained from the actual measured double-pass data (Fig. II-5) by assuming that the relationship between the MTF ( $\psi$ ) and the path length  $L$  through the boundary layer is of the form:  $L = k \log(\psi_0/\psi)$  where  $k$  is a constant and  $\psi_0$  is the optical diffraction limited MTF. The equivalent single-pass MTF, computed

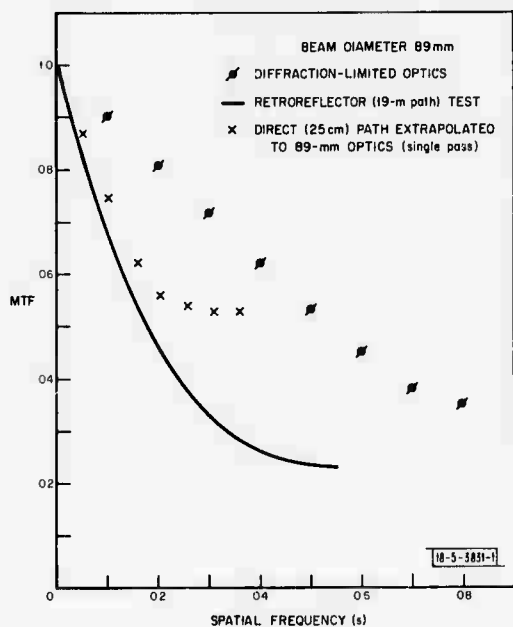
\* Estimated from sheared interferograms photographed during the aircraft flights.

## Section II

in this way from the double-pass measured curve, is next extrapolated from the 24-mm-diameter clear aperture case to the 89-mm-diameter obscured aperture case.

In this extrapolation, it is assumed that there is no inherent aperture size dependence, except for scaling, on the degradation. It is simply an extrapolation along the spatial frequency axis, to correlate this parameter with the respective beam diameter. The resulting curve from this extrapolation is shown in Fig. II-7, in the case of the third window/aft array measurement. It is compared on the same figure with the MTF measurement made in the retroreflector experiment at this same window (daytime flying). For the lower spatial frequencies (below  $s = 0.2$ ) there is relative agreement between the two curves. The extrapolated curve above  $s = 0.2$  is not very

Fig. II-7. MTF of in-flight aircraft boundary layer at third window/aft array [comparison of direct (25-cm) path and retroreflector (19-m) path].



accurate, since it is determined from data at the higher spatial frequencies in the 24-mm-beam experiment where the SNR is poor. Nevertheless, it provides a direct comparison of the in-flight MTF measurement for the local (25-cm) path and the retroreflector experiment (19 m to the wing tip) path at the third window/aft array location. A similar comparison was made for the LFLC position, with slightly poorer agreement between the two curves, due mainly to the influence of window astigmatism on the retroreflector MTF curve at the LFLC position.

### 4. Conclusions

The boundary layer is mainly responsible for the degraded imaging observed in flight through the two aircraft windows mentioned, the seeing being slightly better at the front window. By comparing the local (25-cm) path measurements with the longer (19- or 27-m retroreflector) path measurements it is concluded that the degradation apparently is confined mostly within the 25-cm path.

An attempt made to obtain theoretically computed MTF curves, based upon present knowledge (this ultimately has come from wind tunnel data to date), gives reasonable agreement between theory and experiment for the airplane. The assumptions and estimations made here should be

## Section II

regarded as tentative, until better substantiation of the value for the wavefront errors is obtained.

In summary, the interferometric system has been demonstrated to be capable of MTF measurements over its complete range (to maximum shear) on board an aircraft in flight, and has established the existence of image degradation due to a boundary layer.

D. Kelsall

### D. AIRBORNE IMAGE STUDIES

#### 1. Measurements of the Tropopause Effect

In the fall of 1971, four flights were made with the Lincoln Laboratory KC-135 in the neighborhood of Christchurch, New Zealand, in order to obtain high resolution stellar photographs both above and below the atmospheric tropopause. The purpose was to determine whether any effect could be observed on the images caused by the turbulent air in the boundary region and to relate the measurements, if possible, to proposed  $C_N$  profiles. D. Kelsall has reported<sup>5</sup> the results of MTF measurements which were made on the same flights. He noted no significant trend in the MTF above and below the tropopause, nor any elevation angle dependence (Ref. 5, p. 47).

A 30-cm-diameter Schmidt-Cassegrainian diffraction-limited telescope was used to photograph the images on Kodak plus-X film. Images formed by this telescope in flight have been extensively analyzed; the various sources of image degradation have been identified and measured. In this series of experiments we had hoped to extract the "tropopause component" T in the same way that the other components were found, namely by root differences of squares. Specifically, two separate experiments were performed. The first consisted simply of photographing a star from 5 kft below the tropopause and then from 5 kft above; a complete focus run was made at each altitude. Determining the average altitude of the tropopause was facilitated by balloon soundings received every 12 hours from several locations within a radius of 100 to 200 miles. The Christchurch meteorological office was particularly helpful in obtaining the necessary observations and forecasting information. The estimated tropopause position was checked by recording the free stream temperature vs altitude on the aircraft during the experiment and by noting the altitude at which temperature inversion occurred. The second experiment consisted of photographing a star for 10 sec every minute as the aircraft climbed through the "disturbed" region. This was repeated at a predetermined focus setting on each flight. The rate of climb varied, but averaged about 1000 feet/min.; the total climb was about 10,000 feet. The main advantage of the second experiment over the first was that local weather changes could be kept to a minimum during passage through the tropopause.

After the photographs were developed, about 5 images were selected at random under each condition, enlarged approximately 400X, and their diameters measured by estimating the diameter containing 90 percent of the exposed grains using calibrated circles. This method has been calibrated by an actual grain count to establish the "eye ball" 90-percent-circle. Two sets of independent measurements were made, one by D. G. Kocher and the other by B. W. Bryant. The results were averaged to minimize observer bias. The results of the 4 flights are shown in Fig. II-8. There appears to be little if any dependence of image size on the tropopause position for any of the flights. Other disturbances, possibly local weather, account for most of the changes in image size. For example, the unusually fine images on flight 3 at about 14° elevation

## Section II

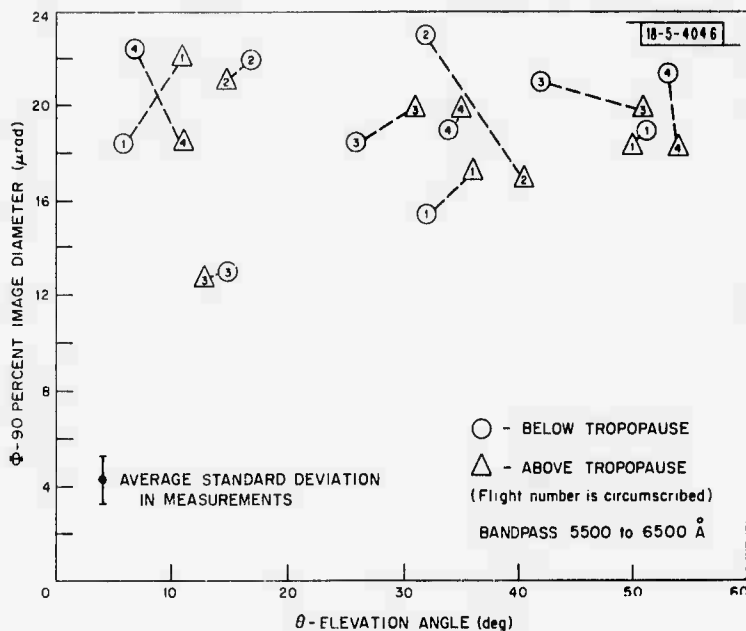


Fig. II-8. Image size vs elevation angle, above and below the tropopause. Flights out of Christchurch, New Zealand, September 1971.

are otherwise very difficult to understand. Of course, the tropopause is a very ill-defined region, in general; the strength of the atmospheric turbulence there can vary greatly. Consequently, one would certainly not expect to find a constant tropopause component. If we let  $\varphi_B$  be image size below the tropopause and  $\varphi_A$  be that above, then the mean value of the component  $T = (\varphi_B^2 - \varphi_A^2)^{1/2} = (\Delta\varphi_i^2)^{1/2}$ . However, from Fig. II-8, one finds that  $\Delta\varphi_i^2$  is negative (T imaginary) about 40 percent of the time. Only at the largest elevation angles do there seem to be consistently better images above the tropopause with  $\bar{T} \approx 7 \times 10^{-6}$  rad, but this is probably illusory since  $7 \times 10^{-6}$  is about the lower limit of statistical significance. In fact, if there were a significant T-component on any of our flights, one would have expected to see a greater and more consistent difference at low elevation angles where the path through the disturbed region is greater. If one is located just at the base of the disturbed region, then the path length varies approximately as cosec of the elevation angle. The path at 4° elevation is about 10X what it is at 50° and therefore  $T(4^\circ)$  should be about 3X  $T(50^\circ)$ . All of our climb-out data were obtained at rather low elevations in order to gain as much sensitivity to the turbulent region as possible. Figures II-9 through -12 summarize these data. Again, the fluctuations appear to be independent of the position of the tropopause within the sensitivity of the measurements. Only in flight 4 (Fig. II-12) where the elevation angle was 4.1° is there even a suggestion of smaller images in the stratosphere. These data lead to  $T \approx 13 \times 10^{-6}$  rad as an upper limit for the contribution of the stratospheric boundary-layer turbulence to the 90-percent image size.

Admittedly, these data represent a small sample at one location and time of year. However, similar data were collected near Anchorage, Alaska, in August 1968. Though not as extensive, the results were very similar to those shown in Fig. II-8. The main limitation to the sensitivity of this method is the existence of a large and variable "airborne seeing" component (now identified

## Section II

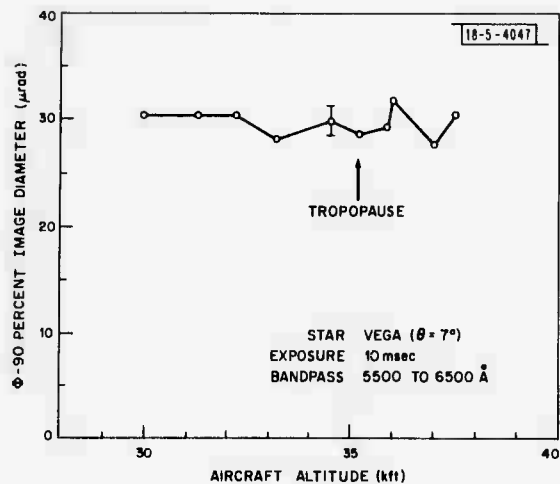


Fig. II-9. Image size vs altitude, flight 1,  
4 September 1971

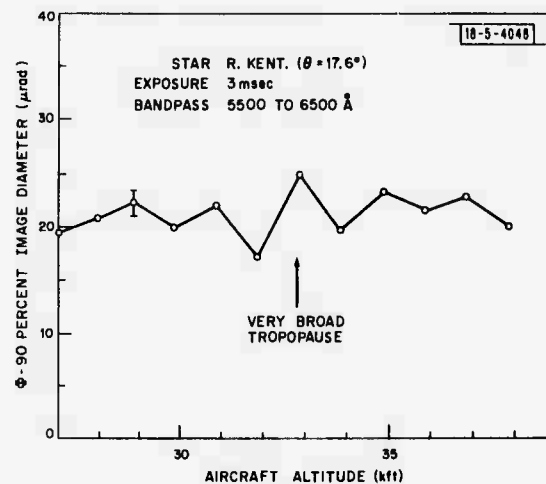


Fig. II-10. Image size vs altitude, flight 2,  
6 September 1971.

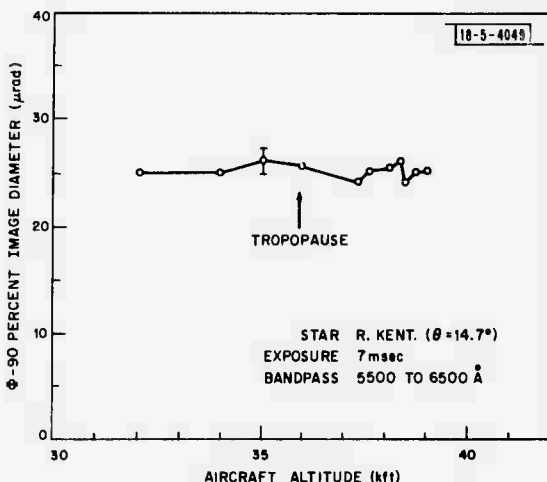


Fig. II-11. Image size vs altitude, flight 3,  
9 September 1971.

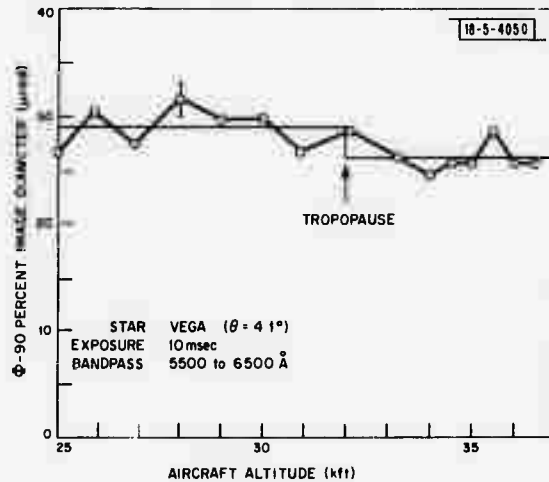


Fig. II-12. Image size vs altitude, flight 4,  
12 September 1971.

## Section II

principally with the aircraft boundary layer), which causes the images to be much larger ( $\sim 20 \times 10^{-6}$  rad) than the Airy disk ( $\sim 4 \times 10^{-6}$  rad). The causes for its fluctuation are not known, but may be related to the air mass changes in the upper atmosphere. During relatively quiet periods, the sensitivity limit is determined by the statistical fluctuations in the measurements ( $\sigma \approx 1 \times 10^{-6}$  rad) of these "enlarged" images. Therefore, the limiting sensitivity,  $S_{\text{limit}} = 10^{-6} \sqrt{(21)^2 - (20)^2} \approx 6.3 \times 10^{-6}$  rad; i.e., any component less than this is lost in the "noise." Because additional noise sources are always present, the practical limit is probably closer to 8 or  $9 \times 10^{-6}$  rad. These results are currently being compared with various theoretical models of the upper atmosphere.

### 2. Boundary Layer

Another series of aircraft experiments was planned and carried out in March and April of 1972 which showed convincingly that the turbulent boundary layer, a region about 10 to 25 cm thick, just beyond the outer surface of the KC-135 fuselage is a major cause of airborne image degradation. The measurements were made using an interferometer, which was originally designed by D. Kelsall for another purpose, and which fortunately became available in time for its inclusion in the planning of a boundary-layer experiment. The description of the experimental setup and the salient results, some of which are used here, are discussed in Sec. II-C of this report. Here, we compare one of these results with the residual B-term (Ref. 1., p. 42) in the experimental formula for the 90-percent image diameter; this term was tentatively ascribed to boundary-layer turbulence. Experimentally, the magnitude of B is approximately  $18 \times 10^{-6}$  rad. The point spread function of the boundary layer can be found by extracting the Fourier transform of the single-pass boundary-layer MTF measured at the LFLC window (see Sec. II-C). Figure II-13 illustrates the MTF as far as the diffraction limit of the 1-inch probe beam will allow its computation. The MTF was computed by dividing the diffraction-limited MTF into the "measured" MTF

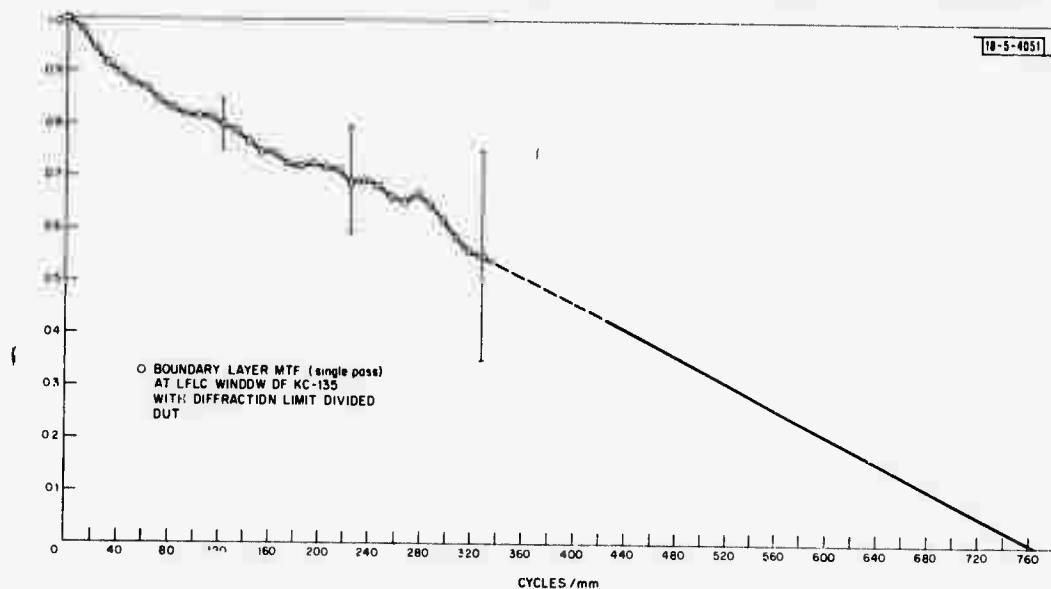


Fig. II-13. Single-pass boundary layer MTF with diffraction limit divided out.

## Section II

(slightly corrected for noise at the high spatial frequencies), which included both boundary layer and diffraction. Unfortunately, the MTF rapidly becomes indeterminate near the diffraction limit, as indicated by the error bars which are rough estimates of the uncertainties. The curve was extended to high-frequency cutoff by an arbitrary linear extrapolation, which is probably not unreasonable, but obviously not very accurate.

The transform was carried out numerically using the Cooley-Tukey fast Fourier transform algorithm. The resultant point spread function (Fourier amplitude squared) is shown in Fig. II-14 along with the 90 percent width, which indicates the points on a 2-dimensional curve which correspond to the circle on a 3-dimensional curve of rotation which enclosed 90 percent of the volume.

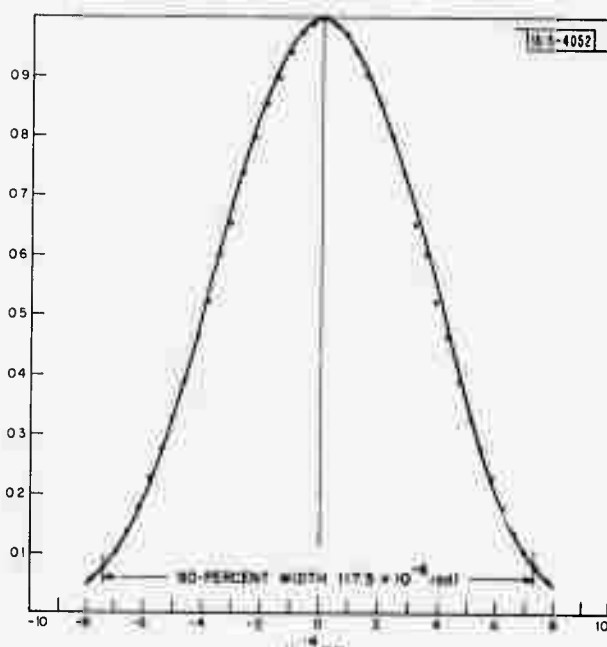


Fig. II-14. Boundary layer point spread function with indication of 90-percent image width.

The abscissa can be converted to an angular scale by dividing by the focal length (85 mm) of the entrance optics to the interferometer. The 90-percent angular width was computed to be  $17.5 \times 10^{-6}$  rad, which is close enough to  $18 \times 10^{-6}$  to leave little doubt that the B-term represents the boundary-layer component.

A number of persons participated in various aspects of these experiments; among them are D. G. Kocher, D. Kelsall, E. A. Davidson and Lt. R. Stiles.

B. W. Bryant

## E. TUNABLE INFRARED LASER SPECTROSCOPY OF SULFUR DIOXIDE

### 1. Introduction

Sulfur dioxide ( $\text{SO}_2$ ) is one of the most common and harmful of the atmospheric pollutant gases. With the advent of laser techniques for remote or *in situ* monitoring of  $\text{SO}_2$  and other gases by their IR "signatures,"<sup>6</sup> knowledge of their fundamental spectra becomes imperative. As we described earlier,<sup>7</sup> tunable semiconductor diode lasers are being developed for air

## Section II

pollution monitoring applications as well as for ultra-high-resolution IR spectroscopy. Doppler-limited spectra have already been obtained for several gases in different spectral regions: sulfur hexafluoride ( $SF_6$ ), ammonia ( $NH_3$ ), and ethylene ( $C_2H_4$ ) around  $10.6\text{ }\mu\text{m}$  using  $Pb_{0.88}Sn_{0.12}Te$  tunable diode lasers;<sup>8</sup> and carbon monoxide (CO), nitric oxide (NO), and water vapor in the 4- to  $6\text{-}\mu\text{m}$  region using  $PbS_{1-x}Se_x$  diode lasers.<sup>9</sup>

In an earlier report<sup>10</sup> we showed preliminary diode-laser studies of the  $\nu_1$  band of  $SO_2$ , centered around  $8.7\text{ }\mu\text{m}$ . The purpose of the present report is to show agreement between the experimental data and theoretical predictions based on accurate microwave absorption data; and thereby to establish a new, more accurate value for the band center. We also show how these results can be used to predict the IR spectra of this gas under varying conditions of temperature and pressure, so that optimum wavelengths for monitoring applications can be selected.

### 2. Diode Laser Fabrication and Experimental Procedure

In order to produce diode lasers which emit between  $1100$  and  $1200\text{ cm}^{-1}$ , single crystals of  $Pb_{1-x}Sn_xTe$  were grown from the vapor phase by a closed-tube process,<sup>11</sup> at three different compositions:  $x = 0.0575$ ,  $0.0700$  and  $0.0745$ . The crystals were cleaved into rectangular parallelepipeds, each containing a p-n junction, of average size  $0.084 \times 0.025 \times 0.029\text{ cm}$  for the six diode lasers used in this study. Low-resistance ohmic contacts were formed, and the lasers were mounted onto the cold-finger of a liquid-He Dewar. Fine-tuning of the wavelength within a single longitudinal mode of the laser was achieved by changing the diode current, which alters the refractive index of the semiconductor through heating of the junction region.

Each of the six lasers exhibited a maximum total CW power from the front face in the 6 to  $44\text{-}\mu\text{W}$  range. Absorption spectroscopy was performed by transmitting the tunable laser radiation through a 30-cm-long cell containing the  $SO_2$ , through a grating spectrometer and onto a Ge:Cu detector. (The purpose of the spectrometer is to provide approximate calibration of the laser wavelength and to limit the IR bandpass to a single longitudinal mode.) The spectra were displayed on an X-Y recorder, whose X-axis was driven by a signal proportional to the diode current (usually quite linear with respect to the wavenumber of the emitted radiation). The Y-axis was driven by a signal proportional to the transmitted IR power, as monitored on the detector by a lock-in amplifier synchronized to a mechanical chopper at the spectrometer entrance slit.

The  $SO_2$  was obtained from the Matheson Company, Inc. of East Rutherford, New Jersey, with a quoted purity of 99.98%. Gas pressure was measured with a capacitance manometer at and below 1 torr, and with a Wallace-Tiernan gauge at higher pressures. The usual test sequence consisted of scans of  $SO_2$  at 0-, 0.1-, 1- and 10-torr pressure, followed by  $NH_3$  for calibration purposes. Use was made of recent precise measurements of the  $NH_3$ -line positions in this region made available to us by Rao, Curtis and Yin.<sup>12</sup>

### 3. Theory

Because of the thousands of relatively strong rotational transitions in  $SO_2$ , identification of individual lines in the  $\nu_1$  vibration-rotation band is somewhat difficult. Fortunately, there are accurate microwave absorption data for both the ground and the first excited vibrational states.<sup>13</sup> For both vibrational states, the microwave measurements can be used to evaluate the constants

## Section II

occurring in a symmetrized expansion of the rotational Hamiltonian in powers of the angular momenta  $J$ .<sup>14</sup> For values of  $J$  up to 60, the energy levels as well as the transition frequencies and strengths for the  $Q_{-1,1}$ ,  $Q_{1,-1}$ ,  $R_{1,1}$ ,  $P_{-1,-1}$ ,  $R_{-1,3}$  and  $P_{1,-3}$  transitions have been calculated. ( $P$ ,  $Q$  and  $R$  have their usual meaning, with the first and second subscripts referring to  $\Delta K_A$  and  $\Delta K_C$ , respectively.) In order to calculate band strengths from measurements on a single spectral line at room temperature, the rotational partition function was evaluated and found to be  $Q_R = 5805$ .

### 4. Results

Figure II-15 shows a  $1.4\text{-cm}^{-1}$ -wide scan, between  $1156.3$  and  $1157.7\text{ cm}^{-1}$ , for  $\text{SO}_2$  at pressures of  $0.1$ ,  $1$  and  $10$  torr, together with two  $\text{NH}_3$  lines for calibration. The  $10\text{-torr}$  curve shows definite pressure-broadening and overlap of closely-spaced lines separated at the lower pressures. Absorption at  $0.1$  torr is difficult to observe because of the noise level. However, it can be seen for several of the strong transitions. Some spectra in other wavelength regions where the laser power was greater were considerably less noisy, and stronger transitions than those shown in Fig. II-15 could be easily seen at pressures below  $0.1$  torr. The individual  $\text{SO}_2$  transitions were identified by comparing their relative positions and intensities with theory, and some of the stronger lines in Fig. II-15 are tabulated in Table II-I. Less than 5 percent of the lines strong enough to be measured by the 20 separate spectral regions covered with the tunable diode lasers could not be explained by theory. In order of decreasing probability, we estimate these lines to be caused by: (a) "hot" bands, the  $v_2$  state being 8-percent occupied at room temperature, (b) other isotopes and (c) weaker transitions not included in the calculation.

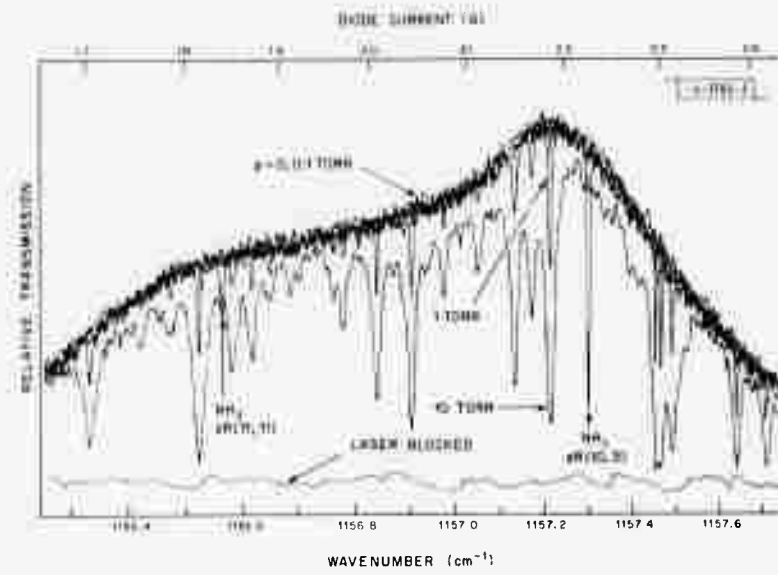


Fig. II-15. Diode laser scans of  $\text{SO}_2$  at pressures of  $0$ ,  $0.1$ ,  $1$  and  $10$  torr at room temperature with a  $30\text{-cm}$  cell. Scan of  $\text{NH}_3$  of  $1$  torr was also made for calibration. Diode laser excitation (and tuning) current is shown by upper horizontal scale. Wavenumber scale represents theoretical positions of observed lines (see Table II-1) using  $1151.71\text{ cm}^{-1}$  as band center.

TABLE II-1  
IDENTIFICATION OF LINES\* IN FIGURE II-15

Transition†	Predicted Wavenumber (cm <sup>-1</sup> )	Predicted Relative Absorption Coefficient
$^6_{1,5} \rightarrow ^6_{2,4}$	1156.335	3.55
$^{21}_{5,17} \rightarrow ^{20}_{6,14}$	.336	1.11
$^{18}_{1,17} \rightarrow ^{18}_{2,16}$	.523	7.82
$^4_{1,3} \rightarrow ^4_{2,2}$	.580	2.18
$^{17}_{3,15} \rightarrow ^{18}_{2,16}$	.615	2.14
$^{23}_{4,20} \rightarrow ^{24}_{3,21}$	.780	1.56
$^{14}_{0,14} \rightarrow ^{14}_{1,13}$	.841	4.67
$^9_{1,9} \rightarrow ^{10}_{0,10}$	.911	5.58
$^3_{1,3} \rightarrow ^3_{2,2}$	.979	1.40
$^{20}_{5,15} \rightarrow ^{19}_{6,14}$	1157.056	1.10
$^6_{0,6} \rightarrow ^7_{1,7}$	.141	4.15
$^{15}_{4,12} \rightarrow ^{14}_{5,9}$	.146	1.10
$^5_{1,5} \rightarrow ^5_{2,4}$	.183	2.33
$^{20}_{1,19} \rightarrow ^{20}_{2,18}$	.222	6.94
$^{22}_{2,20} \rightarrow ^{22}_{3,19}$	.442	7.63
$^{24}_{2,22} \rightarrow ^{24}_{3,21}$	.455	7.21
$^{13}_{2,12} \rightarrow ^{14}_{1,13}$	.478	3.34
$^7_{1,7} \rightarrow ^7_{2,6}$	.481	3.01

\* Only those lines for which the relative absorption coefficients are greater than 1.0 are included.

† Lower energy state is listed first.

## Section II

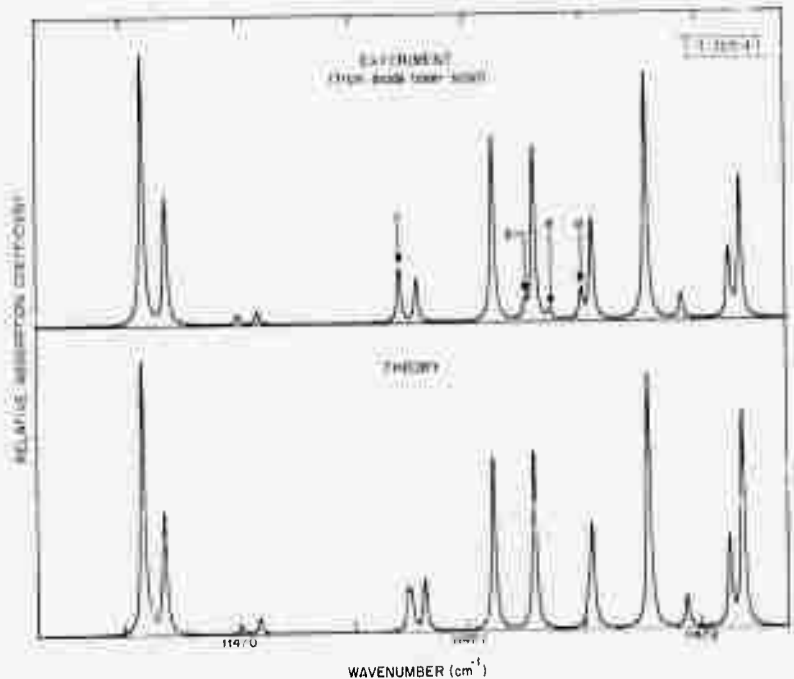


Fig. II-16. Comparison between measured and predicted strengths and positions for some lines in  $\nu_1$  bond of  $\text{SO}_2$ . Scans were computer-generated using Lorentzian line profiles. Lines designated as a, b and c represent transitions  $28_7, 21 \rightarrow 29_6, 24$ ,  $34_8, 26 \rightarrow 35_7, 29$  and  $27_3, 25 \rightarrow 26_4, 22$ , respectively, which appear to be shifted slightly to lower wavenumber (see text). Line d is not predicted by theory.

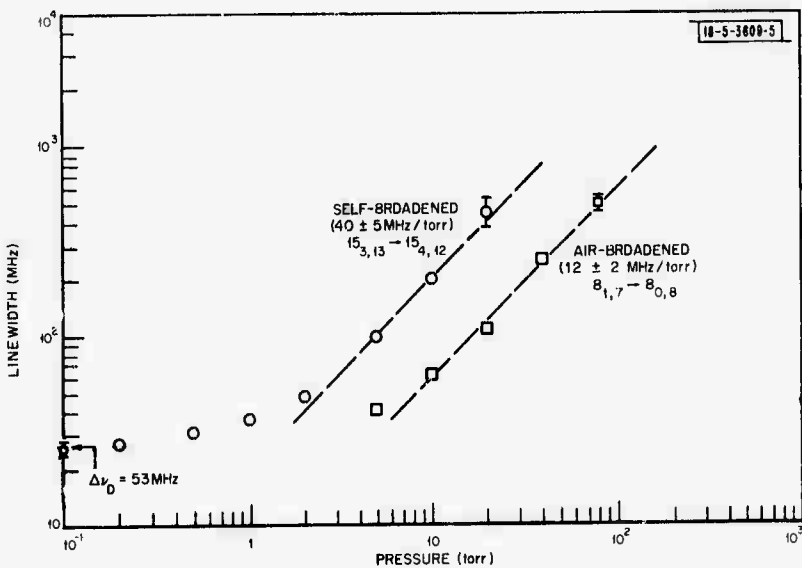


Fig. II-17. Self-broadened and air-broadened dependence of full width at half maximum intensity for two lines at room temperature:  $15_{3,13} \rightarrow 15_{4,12}$  at  $1163.297 \text{ cm}^{-1}$  and  $8_{1,7} \rightarrow 8_{0,8}$  at  $1148.810 \text{ cm}^{-1}$ .

## Section II

The present results yield a value of  $1151.71 \pm 0.01 \text{ cm}^{-1}$  for the  $\nu_1$ -band center frequency of  $^{32}\text{S}^{16}\text{O}_2$ , which can be compared with  $1151.38 \text{ cm}^{-1}$  obtained by Shelton, Nielsen and Fletcher.<sup>15</sup> The uncertainty of  $\pm 0.01 \text{ cm}^{-1}$  in our determination is due in part to possible errors in the  $\text{NH}_3$  spectra, the theoretical calculations, and the intercomparison between the  $\text{NH}_3$  and  $\text{SO}_2$  traces.

Figure II-16 represents a detailed comparison between experimental data from a diode laser scan in the  $1147\text{-cm}^{-1}$  region and the theoretical prediction for lines in this region. The curves marked "experimental" are Lorentzian fits to the line intensities, incorporating a linewidth which best approximates the shape of the experimental curve for the 1-torr pressure at which the data were obtained. (Actually, at 1-torr pressure the  $\text{SO}_2$  line profile is a Voigt convolution of Lorentzian and Gaussian shapes.) There are minor, but significant differences between the two curves, as indicated at a, b and c, where transitions of high  $J$  value appear to be shifted to the left in the experimental curve by a few MHz/unit change in  $J$ . At point d is a line which is not predicted theoretically and may be caused by one of the reasons mentioned above.

Figure II-17 illustrates the pressure-broadening rates for two  $\text{SO}_2$  lines. Self-broadening of the  $15_{3,13} \rightarrow 15_{4,12}$  line at  $1163.297 \text{ cm}^{-1}$  occurs at a rate of  $40 \pm 5 \text{ MHz/torr}$  for the full width at half-maximum at pressures above a few torr. Similarly, the effect of increasing the partial pressure of air on an  $\text{SO}_2$  line at fixed pressure is shown for the  $8_{1,7} \rightarrow 8_{0,8}$  transition at  $1148.810 \text{ cm}^{-1}$ , where the broadening rate is only  $12 \pm 2 \text{ MHz/torr}$ . Although Fig. II-17 does not represent linewidth measurements on the same transition, measurements of the widths of several lines do not indicate any noticeable variation from the pressure-broadening rates shown here. Consequently, the ratio of  $3.3 \pm 0.7$  between self-broadening and air-broadening rates is significant and can be compared to the  $5 \pm 1$  obtained by Burch, *et al.*, when dry  $\text{N}_2$  is used instead of air. (The presence of water vapor in the laboratory atmosphere used for our air-broadening studies may, in fact, be the reason for the smaller ratio.)

By using measured absorption constants and pressure-broadened linewidths at 10-torr pressure for several  $\text{SO}_2$  lines, we have calculated their fundamental line strengths. On the basis of these determinations, and using the theoretical ratios of total partition function to line strength, the total strength of the  $\nu_1$  band is found to be  $358 \pm 20 \times 10^{-20} \text{ cm}^{-1} \text{ molecule}^{-1} \text{ cm}^2$ . This can be compared with the value of  $371 \pm 20 \times 10^{-20} \text{ cm}^{-1} \text{ molecule}^{-1} \text{ cm}^2$  measured by Burch, *et al.*,<sup>16</sup> and is in the range found by earlier workers<sup>17-19</sup> using conventional techniques. An effective dipole moment of  $0.086 \pm 0.003$  Debye is found by a similar calculation.

### 5. Application of Theoretical Spectra to Pollutant Gas Monitoring

Knowledge of the strengths, wavelengths and widths of individual vibration-rotation lines of gaseous pollutants can be used to predict the IR spectra corresponding to a variety of pressure and temperature conditions. For the case in which  $\text{SO}_2$  in smokestack effluent is to be monitored, the gas is at atmospheric pressure and can have wide temperature fluctuations. Using the theoretical data for the thousands of lines in the  $8.7\text{-}\mu\text{m}$  band of  $\text{SO}_2$ , it was possible with the aid of a digital computer to display the absorption spectra for several temperatures. A segment of this band, from  $1110$  to  $1142 \text{ cm}^{-1}$ , is illustrated in Fig. II-18 for selected temperatures from  $0$  to  $400^\circ\text{C}$ . Below  $1126 \text{ cm}^{-1}$ , absorption is highest for higher gas temperatures, whereas the converse is true above  $1126 \text{ cm}^{-1}$ . Consequently, IR absorption of  $\text{SO}_2$  has the smallest temperature dependence around  $1126 \text{ cm}^{-1}$ , which makes this region particularly appropriate for in-stack

## Section II

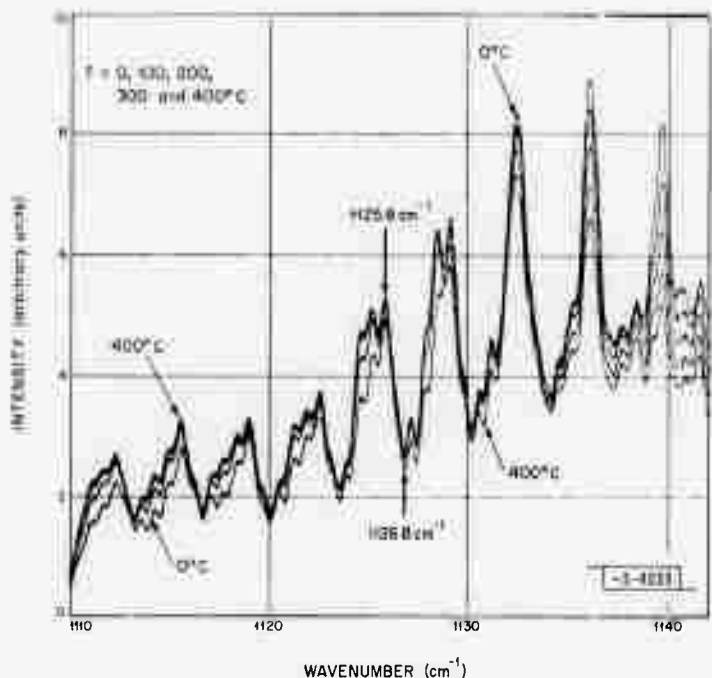


Fig. II-18. Computed spectra for a portion of  $\nu_1$  band of  $\text{SO}_2$  in air at atmospheric pressure, at temperatures from  $0^\circ$  to  $400^\circ\text{C}$ . A constant width of  $0.3 \text{ cm}^{-1}$  was used for all lines.

monitoring of  $\text{SO}_2$ . Moreover, by alternately tuning the laser from  $1125.8$  to  $1126.8 \text{ cm}^{-1}$  and electronically measuring the logarithm of the ratio of the transmitted signals at the two wavelengths, the resulting voltage is directly proportional to pollutant concentration and is not affected by absorption or scattering processes which are invariant over the small wavelength interval.

### 6. Acknowledgments

Appreciation is expressed to Prof. K. N. Rao and his associates at Ohio State University for pre-publication values of the  $\text{NH}_3$ -line positions.

E. D. Hinkley    P. L. Kelley  
S. A. Clough\*    D. I. Underwood  
A. R. Calawa

### F. EXTENSION OF TUNABLE LASER TECHNIQUES TO AIR POLLUTION DETECTION

We have continued to apply techniques using tunable infrared lasers to the problem of detection and measurement of air pollution. As part of this effort we have considered the use of acousto-optic absorption cells in conjunction with discretely tunable gas lasers and tunable diode lasers. We have used tunable diode lasers for *in-situ* measurements of auto exhaust, as well as for long path studies of background concentrations. The work described concerns the gas ethylene ( $\text{C}_2\text{H}_4$ ), although we have also studied  $\text{SF}_6$ ,  $\text{NO}$  and  $\text{CO}$ .

\* Author not at Lincoln Laboratory.

### 1. Spectrophone Investigation

As an alternate method to tunable semiconductor laser transmission measurements for pollutant detection, we have considered a technique whereby an acoustic signal, driven by the absorption of IR radiation, is used to measure trace gas concentration. The technique, first investigated in the 19th Century,<sup>20</sup> has been used recently to measure decay times in gases<sup>21</sup> and to detect traces of methane and nitric oxide in air samples.<sup>22</sup>

The acousto-optic absorption cell, or spectrophone, can assume a variety of forms. The constructions we have used consist of an inner and an outer chamber separated by a capacitance microphone. The air sample is admitted to the outer chamber and diffuses into the inner chamber by means of a small hole. Laser radiation passes in and out of windows attached to the inner chamber. If the laser frequency coincides with an absorption line of the gas, some of its energy is lost to the gas and appears as translational energy causing a pressure differential between the inner and outer chambers. By chopping the laser beam and synchronously detecting the capacitance change produced by this pressure differential, we have measured ethylene concentrations as low as 28 ppb. This measurement used a 0.5 W stable CO<sub>2</sub> laser tuned to the P(14) line, which nearly coincides with an absorption line in ethylene.

Unfortunately, at this low concentration a signal produced by absorption in the windows is dominant and must be subtracted from the measured signal to calculate the effect of the trace gas. In this particular example, the (BaF<sub>2</sub>) window signal was 2.5X the intensity of the signal due to 28 ppb of C<sub>2</sub>H<sub>4</sub>. Consequently, a high degree of stability in laser amplitude and in configuration alignment is required to complete the measurement.

This is not the case with lower power lasers where the sensitivity of the spectrophone determines the lower limit of detection. Several of the spectrophone cells we constructed were capable of detecting less than 10<sup>-8</sup> W of absorbed power (in the absence of a large window absorption signal). With a 5-μW PbSnTe diode laser we were thus able to detect an  $\alpha'cL$  of  $2 \times 10^{-3}$ , where the length L used was 10 cm, c is the gas concentration (ppm) and  $\alpha'$  is its absorption coefficient in (cm · ppm)<sup>-1</sup>. Since  $\alpha'$  is typically 10<sup>-6</sup>/cm · ppm for C<sub>2</sub>H<sub>4</sub>, this corresponds to a minimum detectable concentration near 200 ppm.

In Fig. II-19 we show a comparison between the spectrophone output and the signal received by a Ge:Cu detector after the 5-μW PbSnTe laser radiation has passed through the spectrophone. The diode radiation was tuned over a region near 10.6 μm, and the Doppler-limited spectrum is evident in both the spectrophone and the transmission signals. While the minimum detectable concentration using the spectrophone was more than 10<sup>2</sup> ppm, a detection limit of 1 ppm was possible with the liquid-Hg-cooled Ge:Cu detector under these conditions. This reflects the fact that the spectrophone NEP was near 10<sup>-8</sup> W, while the GeCu detector had a NEP of approximately 3 × 10<sup>-11</sup> W.

### 2. In-Situ Auto Exhaust Measurements

The diode laser, being compact, stable and easily-operated, is highly suitable for field measurements. Utilizing this capability we have performed fast response in-situ measurements of the ethylene concentration in auto exhaust. The undiluted exhaust was drawn through a windowless 1.1-m sample cell and exhausted with a standard garage exhaust fan. Radiation from a

## Section II

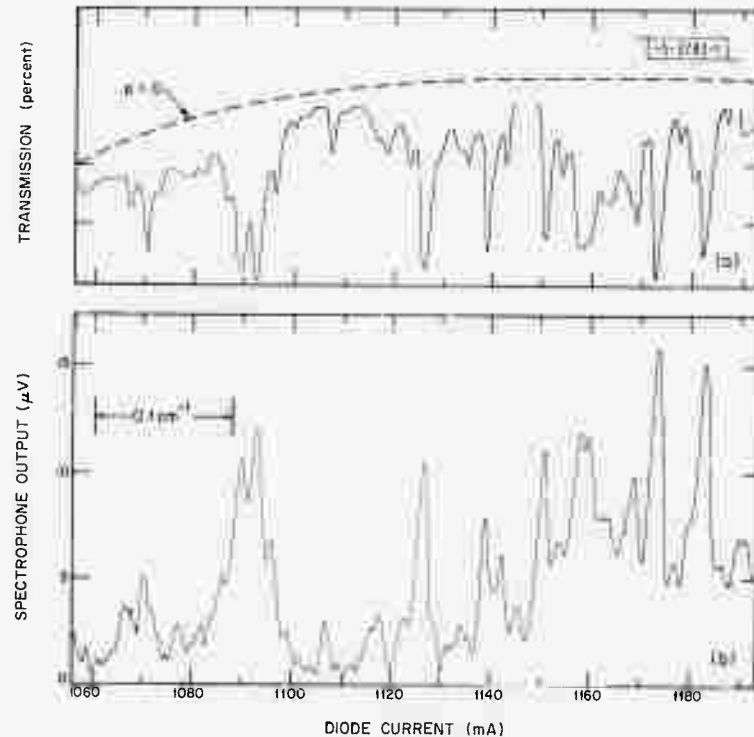


Fig. II-19. Detection of  $\text{C}_2\text{H}_4$  as diode laser emission wavelength is tuned near  $10.6 \mu\text{m}$ : (a) transmission through spectrophone cell (detection  $\tau = 0.03 \text{ sec}$ ); (b) spectrophone output (detection  $\tau = 3 \text{ sec}$ ). Cell length = 10 cm;  $\text{C}_2\text{H}_4$  pressure = 5 torr; air pressure = 15 torr.

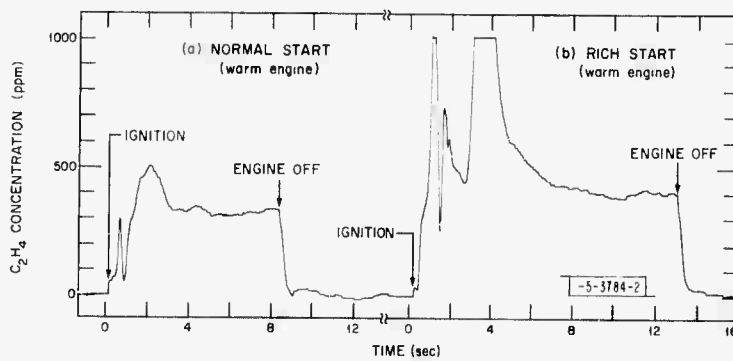


Fig. II-20. On-line  $\text{C}_2\text{H}_4$  emission test for 1972 station wagon (system using pulsed  $\text{Pb}_{0.88}\text{Sn}_{0.12}\text{Te}$  diode laser at  $10.57 \mu\text{m}$ ).

## Section II

PbSnTe diode laser operating at  $10.57\text{ }\mu\text{m}$  was collimated, passed through the sample cell, and collected by a Ge:Cu detector. The detector output was amplified with a logarithmic amplifier and fed to a strip recorder whose deflection was proportional to  $\text{C}_2\text{H}_4$  concentration.

Calibration was accomplished by substituting a cell with known ethylene concentration. Calibration and lack of interference from other gases was further checked by low pressure (Doppler regime) studies of exhaust samples and samples of known concentration.

A typical measurement sequence is shown in Fig. II-20. In Fig. II-20(a) the  $\text{C}_2\text{H}_4$  emission from a 1972 station wagon is measured after a "normal" start. The emission shows two concentration peaks after which the level approaches 350 ppm. Figure II-20(b) shows a "rich" start for which the accelerator pedal was depressed once before starting. The emission exceeds 2000 ppm briefly then approaches the 350 ppm steady-state level. Removal of the air cleaner on this vehicle leaned the fuel-air mixture and reduced the steady state ethylene concentration to 160 ppm. Other vehicles tested showed somewhat higher concentrations. Figure II-21 shows the ethylene content of a poorly tuned 1964 sedan. The average concentration is 800 ppm. The wide trace is not due to system noise, but rather to rapid fluctuations in this car's ethylene output.

These tests were designed to demonstrate the suitability of diode laser transmission studies to real-time measurement of pollution sources. They will be extended to include other gases, such as nitric oxide and carbon monoxide.

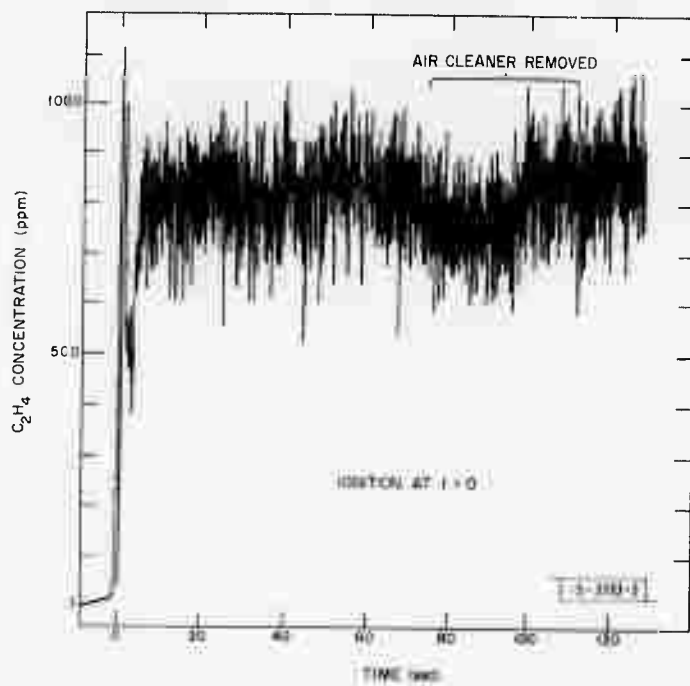


Fig. II-21. On-line  $\text{C}_2\text{H}_4$  emission test for untuned 1964 sedan (system using pulsed  $\text{Pb}_{0.88}\text{Sn}_{0.12}\text{Te}$  diode laser at  $10.57\text{ }\mu\text{m}$ ).

## Section II

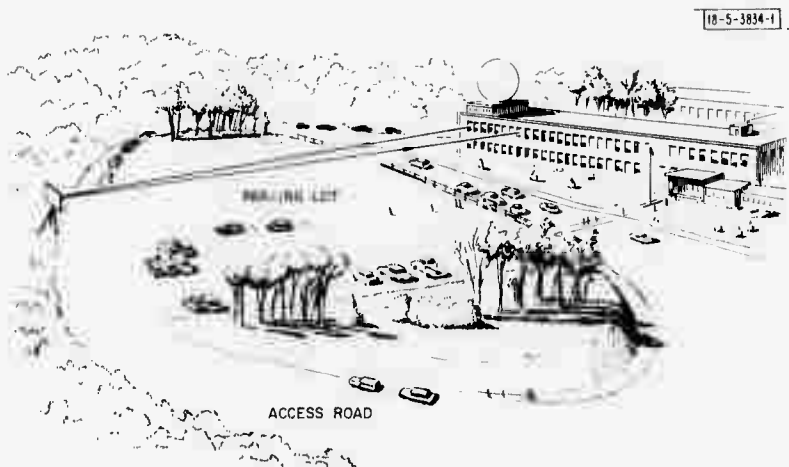


Fig. II-22. Long-path tunable-laser ambient air monitoring setup.

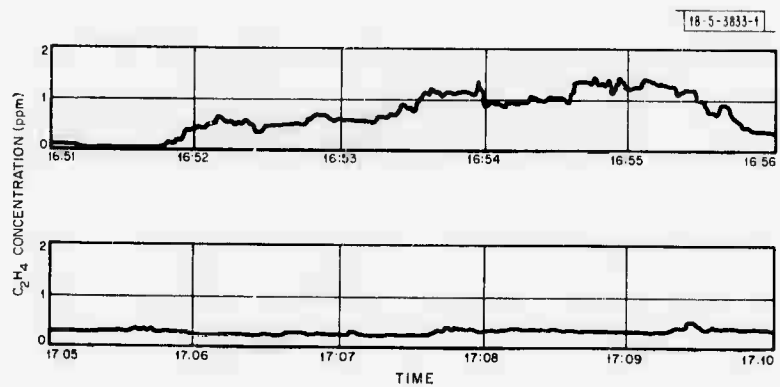


Fig. II-23. Measurement of ambient C<sub>2</sub>H<sub>4</sub> concentration using Pb<sub>0.88</sub>Sn<sub>0.12</sub>Te diode laser (0.5-km path).

### 3. Long-Path Laser Transmission Studies

To increase the sensitivity of the diode laser transmission technique to measure pollutant levels in ambient air (typically 10 to 100 ppb) it is necessary to use longer path lengths than are convenient for laboratory application. Also, the integrated concentration obtained from long path measurements is often more suitable than point by point results for regional air quality studies.

We have operated the PbSnTe diode laser, described above, over a 0.5-km path from Lincoln Laboratory to a remote reflector and back. The experimental path, illustrated in Fig. II-22, passed over the Laboratory parking lot and allowed us to measure changes in the ethylene content during peak traffic hours. Figure II-23 shows an increase in the measured  $C_2H_4$  concentration of over 1 ppm during the late afternoon departure of Laboratory personnel. Peaks due to individual cars (such as the poorly tuned 1964 sedan mentioned above) were also noted.

In this experiment, the laser radiation was collimated to a  $2 \times 4$ -cm beam before transmission. It was collected by a larger mirror, used off-axis, and concentrated on the liquid-He-cooled detector. With this very simple arrangement, we were able to collect more than 30 percent of the transmitted energy. The SNR obtained was limited by atmospheric fluctuations, rather than diode power or detector considerations. As a result of these measurements, we expect to be able to extend the path length to many kilometers without difficulty. By using the two-pulse frequency scanning technique, developed for the EPA smokestack measurement apparatus, we expect to obtain detection sensitivities near 1 ppb.

H. A. Pike  
E. D. Hinkley  
A. R. Calawa

## Section II

### REFERENCES

1. Optics Research Report, Lincoln Laboratory, M. I. T. (1971:2), pp. 35, 42, DDC AD-901213.
2. Op. cit. (1970:3), p. 35, DDC AD-882617.
3. R. Barakat, "The Influence of Random Wavefront Errors on the Imaging Characteristics of an Optical System," Optical Acta. 18, 683 (1971).
4. Ibid., p. 687.
5. Ref. 1, p. 42-47.
6. For recent review articles, see H. Kildal and R. L. Byer, Proc. IEEE 59, 1644 (1971); I. Melngailis, IEEE Trans. Geosci. Electron. GE-10, 7 (1972), DDC AD-742624.
7. Ref. 2, pp. 40-43.
8. E.D. Hinkley and P.L. Kelley, Science 171, 635 (1971), DDC AD-723786.
9. K.W. Nill, F.A. Blum, A.R. Calawa and T.C. Harman, Appl. Phys. Letters 19, 79 (1971), DDC AD-734114; Chem. Phys. Letters (to be published).
10. Optics Research Report, Lincoln Laboratory, M. I. T. (1971:1), pp. 35-46, DDC AD-888823-L.
11. Solid State Research Report, Lincoln Laboratory, M. I. T. (1971:1), pp. 4-5, DDC AD-724074.
12. K.N. Rao, J.B. Curtis and P. Yin (to be published); the NH<sub>3</sub> transitions are identified using the notation of J.S. Garing, H.H. Nielsen and K.N. Rao, J. Molec. Spectros. 3, 496 (1959).
13. G. Steenbeckeliers, Ann. Soc. Sci. Bruxelles 82, 331 (1968).
14. W.S. Benedict, S.A. Clough, L. Frenkel and T.E. Sullivan, J. Chem. Phys. 53, 2565 (1970).
15. R.D. Shelton, A.H. Nielsen and W.H. Fletcher, J. Chem. Phys. 21, 2178 (1953).
16. D.E. Burch, J.D. Pembrook and D.A. Gryvnak, private communication.
17. J. Morcillo and J. Herranz, Anales real Soc. espan. fis. y quim. A 52, 207 (1956).
18. J.E. Mayhood, Can. J. Phys. 35, 954 (1957).
19. D.F. Eggers, Jr. and E.D. Schmid, J. Phys. Chem. 64, 279 (1960).
20. J. Tyndall, Proc. Roy. Soc. 31, 307 (1881); W.C. Rontgen, Phil. Mag. 11, 308 (1881); A.G. Bell, Phil. Mag. 11, 510 (1881).
21. M.E. Delaney, Sci. Progr. 47, 459 (1959).
22. L.B. Kreuzer, J. Appl. Phys. 42, 2934 (1971); L.B. Kreuzer and C.K.N. Patel, Sci. 173, 45 (2 July 1971).

### III. LASER RADAR AND TRACKING

#### A. INSTRUMENT FOR ATMOSPHERIC MODULATION TRANSFER FUNCTION MEASUREMENTS

##### 1. Introduction

A modulation transfer function (MTF) instrument which is of simple design and easily transported has been constructed for visible atmospheric propagation measurements. A picture of this instrument and a schematic drawing of its operation are shown in Figs. III-1(a, b).

An 8.6-cm-diameter Questar telescope is used to form an image of a distant point source, e.g., a He-Ne laser. This point source is re-imaged onto the rotating MTF reticle, which is a Siemann star pattern of alternately reflecting and nonreflecting  $2^\circ$  segments or bars. The bar spacing, that is, the spatial frequency, is a function of radius on the reticle and is selected by tilting the scan mirror. The modulation of the reflected light at each radius setting produced by the spinning reticle and detected at the photomultiplier gives a direct measure of the MTF at that spatial frequency.

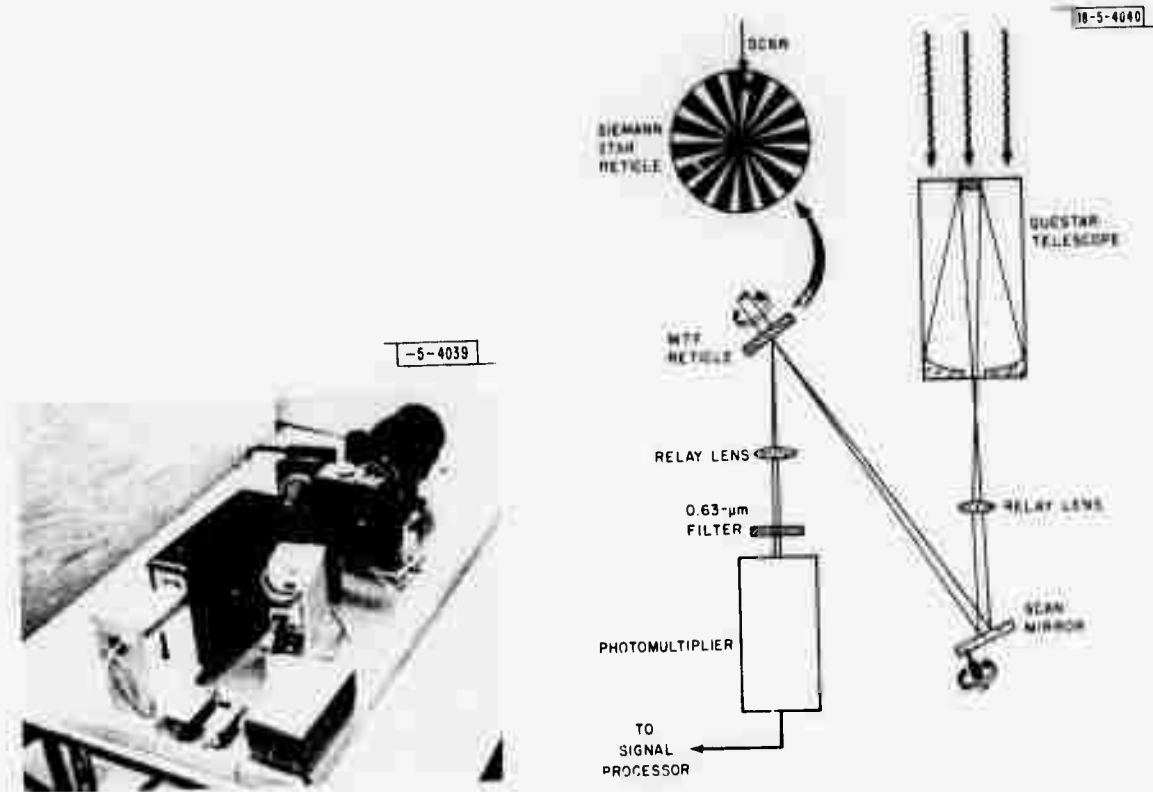


Fig. III-1. MTF instrument: (a) photograph; (b) schematic diagram.

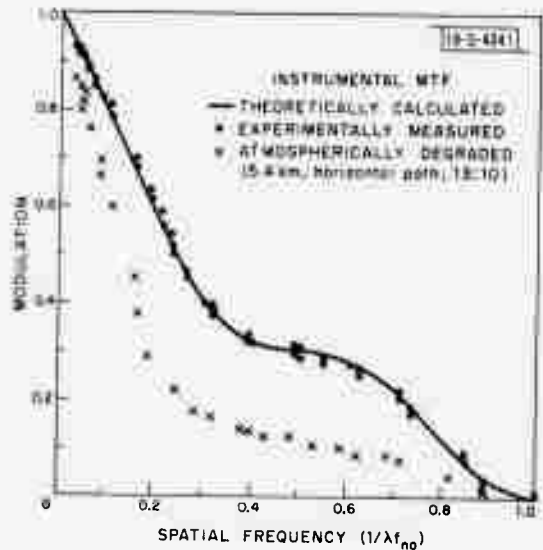


Fig. III-2. Instrumental modulation transfer function.

Figure III-2 shows the theoretically calculated MTF for the instrument along with a corresponding experimental measurement. The particular shape is due to the central obstruction in the Questar aperture ( $\eta = r_1/r_2 = 0.39$ ). Also shown in Fig. III-2, is an example of the instrumental MTF degraded by the atmosphere. The case shown is for a 5.4-km horizontal path and was taken at 13:10 EDT. The results of a more comprehensive set of measurements on the atmospheric MTF, made in conjunction with 10.6- $\mu\text{m}$  propagation measurements also described herein, will be presented in the next Optics Research Report.

J. Z. Holtz  
T. J. Gilmartin  
L. J. Prugnarola

## 2. MTF Electronics

The electronics used with the MTF instrument consists of a square-wave generator and a signal processor.

The square-wave generator consists of a light source and photodetector in an integral housing with a beam splitter and lens such that the light is focused on the rotating reticle and the return beam is focused on the photodetector. Following the photofet detector are an amplifier and an emitter follower which provides a low output impedance. The square-wave generator provides the reference signal when a lock-in amplifier is used to process the data.

The signal processor provides an output proportional to the percentage modulation impressed on the incoming beam by the rotating reticle. It includes:

- (a) Photomultiplier
- (b) Photomultiplier buffer
- (c) Low-pass active filter before the signal strength meter
- (d) AGC loop amplifier and filter, which control the voltage applied to the photomultiplier and thus its gain

### Section III

- (e) Active bandpass filter tuned to the frequency produced by the bar pattern of the rotating reticle
- (f) Full-wave rectifier and filter, which convert the output of the bandpass filter into a DC voltage proportional to the percentage modulation.

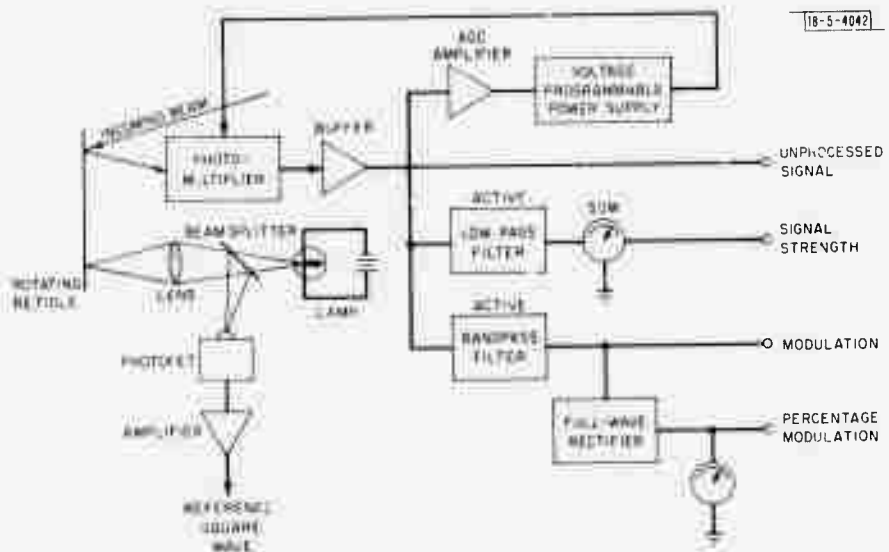


Fig. III-3. MTF control and signal processing electronics.

Outputs are available at various points for recording or for connecting other measuring instruments. Figure III-3 is a block diagram of the electronics. M. D. Zimmerman

#### B. AUTOMATIC RANGE TRACKER

Detailed plans for an automatic range tracker for the Firepond laser radar installation were devised. Implementation of the plans has been cancelled because of planned program and system changes at Firepond.

An automatic switch designed to interchange the tuning relationships of the local oscillator (LO) to the master oscillator (MO) as controlled by the delta f loop servo has been constructed and is ready to be installed and tested. It will switch the output frequency of the LO from 5 MHz below the MO frequency to 5 MHz above the MO frequency when the Doppler frequency goes to zero. In this manner, the signal frequency at the detector mixer output will be prevented from going to zero regardless of whether the moving target is on the incoming or outgoing leg of its pass. Figure III-4 is a block diagram of the switching scheme.

Design and construction of the remote control circuits to be used with the AIL monopulse tracking receiver have been completed. The circuits are ready to be installed and tested at Firepond when the receiver arrives. M. D. Zimmerman

### Section III

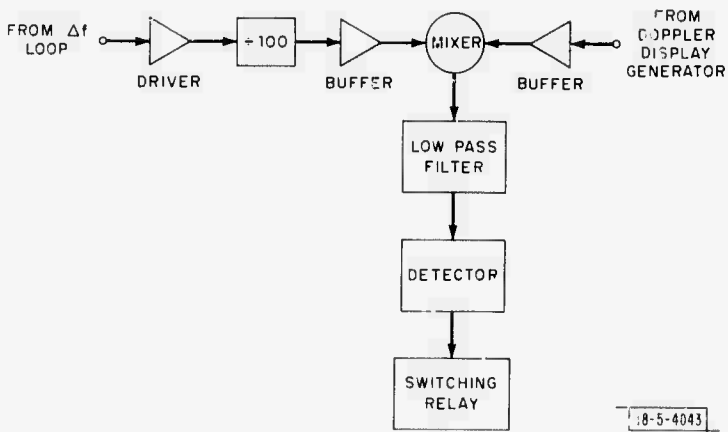


Fig. III-4. Automatic Doppler switchover.

#### C. ATMOSPHERIC OPTICAL COHERENCE MEASUREMENTS AT 10.6 AND 0.63 $\mu\text{m}$

The performance of large aperture optics ( $D > 1 \text{ m}$ ) at  $10.6 \mu\text{m}$  in projection and heterodyne reception has previously been estimated by extrapolating from measurements made at shorter wavelengths. Since large and complex systems are being contemplated at  $10.6 \mu\text{m}$ , it is of great practical interest to measure directly the effect which atmospheric refractive inhomogeneities will have on such systems. To this end, a 48-inch-diameter (1.2 m) Cassegrainian telescope was focused at a range of 5.4 km, where the  $10.6 \mu\text{m}$  spot fell on a diffuse metal surface, was scanned with an IR imaging camera and recorded for later computer analysis. Simultaneously, the optical quality of parallel paths 1 and 2 m distant from the primary path were monitored at  $0.63 \mu\text{m}$  with a MTF instrument and with a two-point, white light source resolution instrument. The optical paths were horizontal with an average altitude of 68 m.

Data have now been taken under a variety of meteorological conditions and over several diurnal cycles. However, while most of the data from the visible instruments have been analyzed, the computer analysis of the  $10.6 \mu\text{m}$  data will not be completed for several weeks. For this reason, a detailed description of the experiment or of the results will not be presented at this time, but some qualitative observations will be made.

Defining the atmospheric coherence diameter  $r_0$  to be the diameter which, when used in a vacuum, allows the same resolution as does the atmosphere when not aperture limited, the atmospheric  $r_0$  was measured by the MTF instrument to range from about 1 to 20 cm at  $0.63 \mu\text{m}$ . Since  $r_0$  is predicted to scale as  $\lambda^{6/5}$ ,  $r_0(10.6 \mu\text{m})$  is expected to equal  $29.4 r_0(0.63 \mu\text{m})$  and the  $r_0(10.6 \mu\text{m})$ , implied by the visible measurements, ranges from 30 cm to 6 m. Indeed, the image projected by the 1.2-m aperture at  $10.6 \mu\text{m}$  was observed to be almost perfectly diffraction limited occasionally, near diffraction limited most often, and badly degraded occasionally. A measurement-by-measurement correlation of coherence data taken at the two wavelengths is presently being made.

The  $10.6 \mu\text{m}$  spot wander was observed to range from a fraction of the diffraction-limited spot radius to several spot radii at extremes under typical wind and turbulence conditions. The correlation time for spot wander and image distortion was typically a fraction of a second.

### Section III

A more detailed and comprehensive description of the results of these propagation measurements will be given in the next Optics Research Report.

T. J. Gilmartin  
J. Z. Holtz  
R. N. Capes

#### D. InSb ISOLATOR

We have previously reported that when 10.6- $\mu\text{m}$  radiation is incident on an InSb sample that is rigidly attached to a heat sink, beam distortion occurs. The stress caused by local heating will not be uniform in this case and the resultant unsymmetrical change in the index of refraction will cause the distortion.

A new holder has been designed which allows the sample to expand uniformly. The holder is shown in Fig. III-5. Tests using a 12-W beam incident on a 4-mm piece of InSb held by the new holder show none of the distortion previously observed.

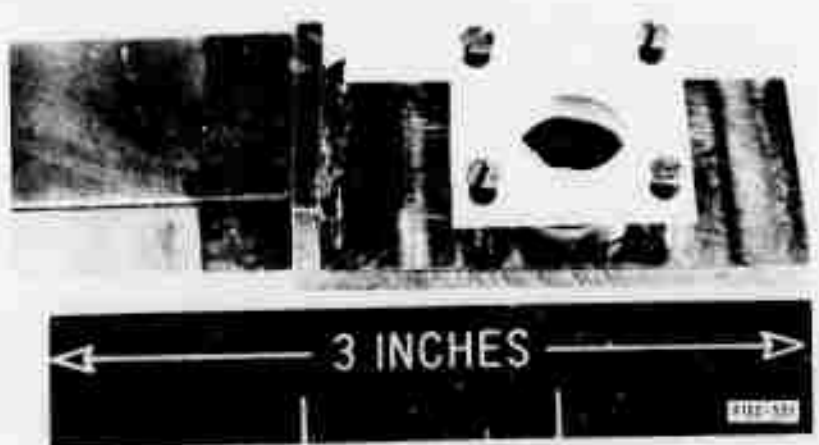


Fig. III-5. InSb holder.

A profilometer was constructed which scans the beam at  $1\frac{1}{2}$ -inch/min. (25 thousandths/sec) through a 20 to 30 thousandths aperture. The time constant of the detector is  $10^{-3}$  sec. Results from the profilometer show no gross differences between the beam directly from the laser and one that has passed through an InSb sample.

An isolator was constructed using Faraday free carrier rotation. Pictures of the system are shown in Figs. III-6 and -7. The Dewar and a polarizer are shown in Figs. III-8 and -9, respectively.

The isolator has been tested in the laboratory. Characteristics of the 10.6- $\mu\text{m}$  isolator are:

Material	$n = \text{InSb}$
Concentration	$1.0 \times 10^{16} \text{ cm}^{-3}$
Thickness	4 mm
Verdet constant	$1.1 \times 10^{-2} \text{ deg/cm-G}$
Field for 45° rotation	10.2 kG
Operating temperature	77°K

Section III

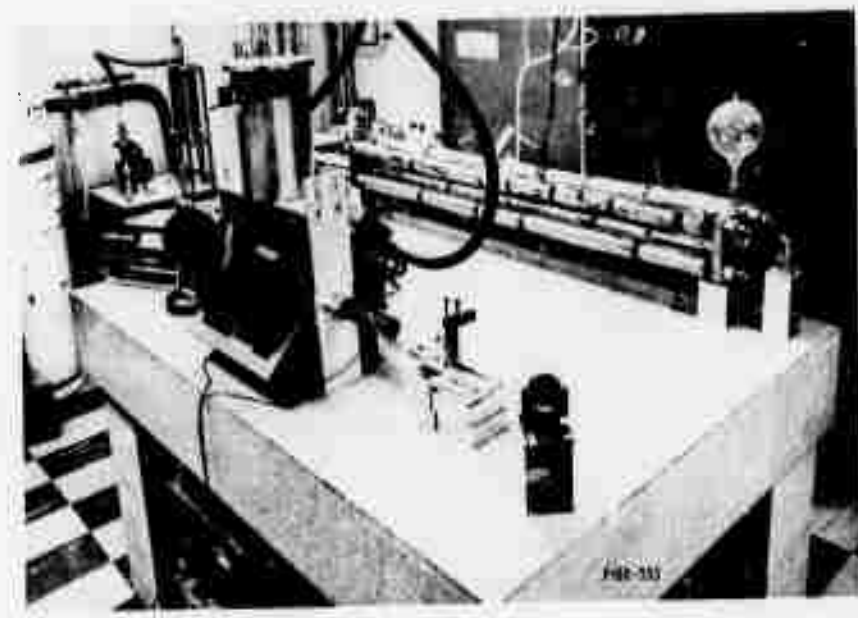


Fig. III-6. Complete isolator showing Dewar, magnet and polarizer.

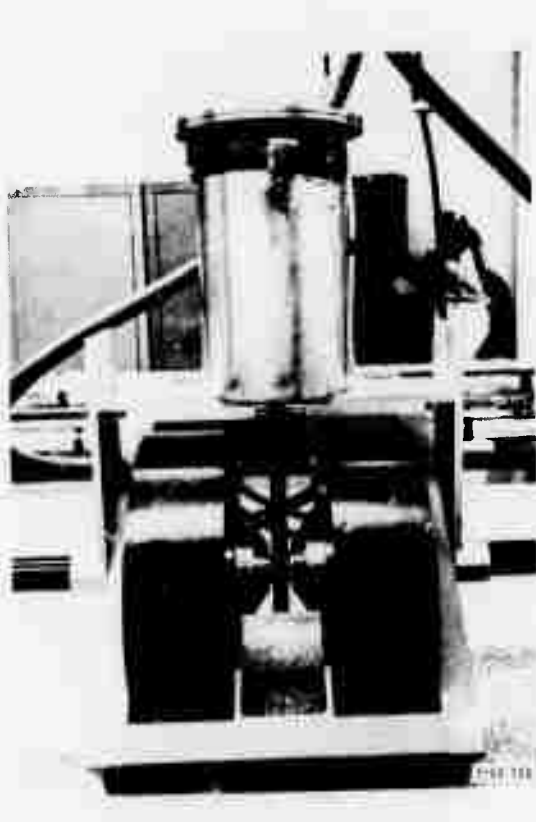


Fig. III-7. Closeup of Dewar and magnet showing flange containing InSb between pole faces.

Section III

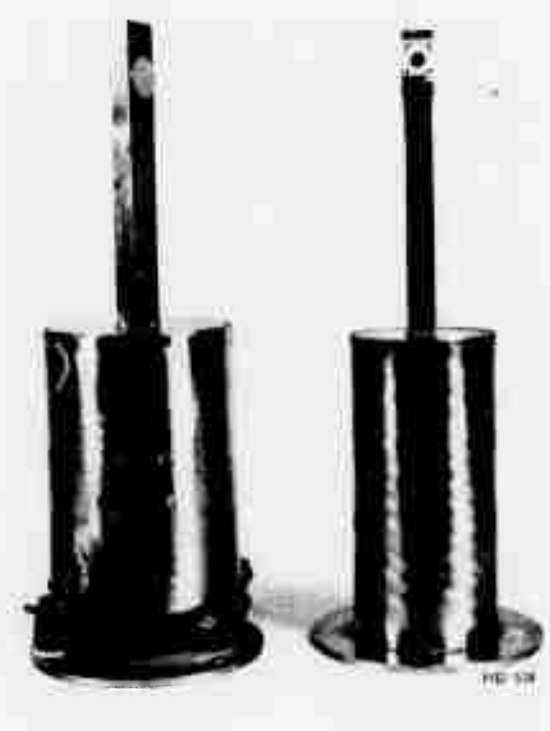


Fig. III-8. Exploded view of Dewar: on left, the outer Dewar with Ge A-R coated windows; on right, the inner liquid nitrogen reservoir with InSb ottoched. Liquid nitrogen flows to the copper plug visible just below the InSb holder.



Fig. III-9. Exploded view of Ge brewster and polarizer.

### Section III

Insertion loss	$2 \pm 0.5$ dB
Isolation	$20 \pm 0.5$ dB
Total reverse loss	$22 \pm 1$ dB
Maximum forward throughput power	30 W CW
Safety factor	2.9 (calculated)

The safety factor is the ratio of the radius of any aperture to the beam waist at the worst point in the optical path. In this case it occurs at the point where the pole faces and the magnet coils meet.

Isolation seems to be limited by non-uniformity in the magnetic field across the  $\frac{1}{4}$ -inch aperture in the pole piece. Maximum isolation based on the limitation of the Ge Brewster angle polarizers is 26 dB. [There is a 23 percent transmission of perpendicular polarization through each surface. There are 4 surfaces, thus the isolation is  $0.23^4$ .] Notice we are 6 dB below this level indicating that this is not the limiting factor.

Some improvement might be possible by using a magnet with larger pole faces. Larger pole faces generally reduce variation of field across a  $\frac{1}{4}$ -inch-diameter hole in the pole faces.

An investigation of the power handling capability of the isolator when 300-nsec pulses are incident will be undertaken. The effect of InSb on the waveform of the pulse will be examined.

L. R. Tomasetta  
W. E. Bicknell  
D. H. Bates